



# NAVAL POSTGRADUATE SCHOOL Monterey, California



DTIC  
ELECTE  
MAR 05 1992  
S D D

## THESIS

A STUDY OF THE MICROSTRUCTURAL BASIS FOR THE  
STRENGTH AND TOUGHNESS PROPERTIES OF  
OVERAGED HSLA-100 STEEL

by

Lawrence Whitley Comerford

JUNE 1991

Thesis Advisor:

Alan G. Fox

Approved for public release: Distribution is unlimited

92 3 02 042

92-05306



Unclassified

SECURITY CLASSIFICATION OF THIS PAGE

REPORT DOCUMENTATION PAGE				Form Approved OMB No 0704-0188	
1a. REPORT SECURITY CLASSIFICATION <b>Unclassified</b>			1b. RESTRICTIVE MARKINGS		
2a. SECURITY CLASSIFICATION AUTHORITY			3. DISTRIBUTION/AVAILABILITY OF REPORT <b>Approved for public release: Distribution is unlimited</b>		
2b. DECLASSIFICATION/DOWNGRADING SCHEDULE					
4. PERFORMING ORGANIZATION REPORT NUMBER(S)			5. MONITORING ORGANIZATION REPORT NUMBER(S)		
6a. NAME OF PERFORMING ORGANIZATION <b>Naval Postgraduate School</b>		6b. OFFICE SYMBOL (If applicable) <b>ME</b>	7a. NAME OF MONITORING ORGANIZATION <b>Naval Postgraduate School</b>		
6c. ADDRESS (City, State and ZIP Code)  <b>Monterey, CA 93943-5000</b>			7b. ADDRESS (City, State, and ZIP Code)  <b>Monterey, CA 93943-5000</b>		
8a. NAME OF FUNDING/SPONSORING ORGANIZATION <b>David Taylor Research Center</b>		8b. OFFICE SYMBOL (If applicable) <b>Code 2814</b>	9. PROCUREMENT INSTRUMENT IDENTIFICATION NUMBER		
8c. ADDRESS (City, State, and ZIP Code)  <b>Annapolis, MD 21402</b>			10. SOURCE OF FUNDING NUMBER		
			PROGRAM ELEMENT NO.	PROJECT NO.	TASK NO.
11. TITLE (Include Security Classification) <b>A STUDY OF THE MICROSTRUCTURAL BASIS FOR THE STRENGTH AND TOUGHNESS PROPERTIES OF OVERAGED HSLA-100 STEEL</b>					
12. PERSONAL AUTHORS <b>LAWRENCE WHITLEY COMERFORD</b>					
13a. TYPE OF REPORT <b>Master's Thesis</b>		13b. TIME COVERED FROM _____ TO _____		14. DATE OF REPORT (Year, Month, Day) <b>JUNE 1991</b>	
15. PAGE COUNT <b>115</b>					
16. SUPPLEMENTARY NOTATION <b>The views expressed are those of the author and do not reflect the official policy or position of the Department of Defense or the U.S. Government</b>					
17. COSATI CODES			18. SUBJECT TERMS (Continue on reverse if necessary and identify by block numbers) <b>HSLA, non-metallic inclusions</b>		
FIELD	GROUP	SUB-GROUP			
19. ABSTRACT (Continue on reverse if necessary and identify by block numbers) A certification program for the use of HSLA steel in ship construction is currently being funded by the U.S. Navy. Integral to this program is the characterization of the microstructure of the highly weldable HSLA-100 steel. In the present work, optical, scanning electron and transmission electron microscopy were employed to analyze the microstructural basis for the mechanical properties of as-quenched and tempered HSLA-100 steel in the form of 31.75 mm plate. The as-quenched microstructure contained bainite/martensite laths and a small amount of retained austenite. The strength and toughness in this specimen was based on the small transformation product packets with their fine laths and highly dislocated substructures. The best combination of strength and toughness occurred for the sample tempered at 621°C; the recovery of the dislocation substructures, the precipitation of overaged copper and carbides, and the small transformation product packet size accounted for the high toughness at this tempering temperature. The size, distribution, and composition of non-metallic inclusions were also determined; the inclusion population generally consisted of small, globular, homogeneously dispersed particles. However, exogenous oxides on the order of 50 µm were occasionally found as well as slightly brittle oxides which had broken up in the rolling direction. As a result of this investigation, it is suggested that the optimum aging temperature for 31.75 mm as-quenched HSLA-100 plate is around 600°C and that improved secondary steelmaking procedures are adopted to eliminate the large, deleterious non-metallic inclusions.					
20. DISTRIBUTION AVAILABILITY OF ABSTRACT <b>XX UNCLASSIFIED/UNLIMITED</b> SAME AS RPT DTIC USERS			21. ABSTRACT SECURITY CLASSIFICATION <b>unclassified</b>		
22a. NAME OF RESPONSIBLE INDIVIDUAL <b>Alan G. Fox</b>			22b. TELEPHONE (Include Area Code) <b>(408) 646-2142</b>		22c. OFFICE SYMBOL <b>ME</b>

DD Form 1473, JUN 86

Previous editions are obsolete.  
S/N 0102-LF-014-6603SECURITY CLASSIFICATION OF THIS PAGE  
**Unclassified**

Approved for public release: Distribution is unlimited

A Study of the Microstructural Basis  
for the Strength and Toughness Properties  
of Overaged HSLA-100 Steel

by

Lawrence Whitley Comerford  
Lieutenant, United States Navy  
B.S.M.E., United States Naval Academy, 1983

Submitted in partial fulfillment of the  
requirements for the degree of

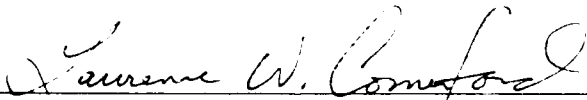
MASTER OF SCIENCE  
IN MECHANICAL ENGINEERING

from the


NAVAL POSTGRADUATE SCHOOL


JUNE 1991

Author:

  
Lawrence Whitley Comerford

Approved by:

  
Alan G. Fox, Thesis Advisor

  
A.J. Healey, Chairman  
Department of Mechanical Engineering

## ABSTRACT

A certification program for the use of HSLA steel in ship construction is currently being funded by the U.S. Navy. Integral to this program is the characterization of the microstructure of the highly weldable HSLA-100 steel. In the present work, optical, scanning electron and transmission electron microscopy were employed to analyze the microstructural basis for the mechanical properties of as-quenched and tempered HSLA-100 steel in the form of 31.75 mm plate. The as-quenched microstructure contained bainite/martensite laths and a small amount of retained austenite. The strength and toughness in this specimen was based on the small transformation product packets with their fine laths and highly dislocated substructures. The best combination of strength and toughness occurred for the sample tempered at 621°C; the recovery of the dislocation substructures, the precipitation of overaged copper and carbides, and the small transformation product packet size accounted for the high toughness at this tempering temperature. The size, distribution, and composition of non-metallic inclusions were also determined; the inclusion population generally consisted of small, globular, homogeneously dispersed particles. However, exogenous oxides on the order of 50  $\mu\text{m}$  were occasionally found as well as slightly brittle oxides which had broken up in the rolling direction. As a result of this investigation, it is suggested that the optimum aging temperature for 31.75 mm as-quenched HSLA-100 plate is around 600°C and that improved secondary steelmaking procedures are adopted to eliminate the large, deleterious non-metallic inclusions.

Accession For	
NTIS CRASH	✓
DRG TAB	11
Unrecorded	12
J. Publication	
By	
Date to	
Author	
Date	
A-1	

## TABLE OF CONTENTS

I.	INTRODUCTION .....	1
II.	BACKGROUND .....	4
	A. CHARACTERISTICS OF HSLA STEEL .....	4
	B. THE EFFECTS OF MICROALLOYING .....	7
	C. STRUCTURE-PROPERTY RELATIONSHIPS IN BAINITIC STEELS .....	12
	D. PROCESSING OF HSLA-100 STEELS TO ACHIEVE HIGH STRENGTH AND TOUGHNESS .....	17
	E. THE AGING BEHAVIOR OF COPPER .....	19
	F. INCLUSIONS IN STEEL .....	22
	1. Sources of Inclusions .....	23
	2. Composition of Inclusions in Steel .....	24
	3. Effects of Inclusions on Steel Properties .....	25
	4. The Role of Calcium on Inclusion Control .....	28
	G. SCOPE OF PRESENT WORK .....	32
III.	EXPERIMENTAL PROCEDURE .....	34
	A. MATERIAL .....	34
	B. MECHANICAL PROPERTIES .....	34
	C. MICROSCOPY .....	35
	1. Optical Microscopy .....	35
	2. Scanning Electron Microscopy .....	37
	3. Transmission Electron Microscopy .....	37
IV.	RESULTS AND DISCUSSION .....	39
	A. INCLUSION STUDY .....	39
	1. Optical Microscopy .....	39
	2. Scanning Electron Microscopy .....	42

B.	MECHANICAL BEHAVIOR .....	50
C.	MICROSTRUCTURE .....	54
1.	As-quenched HSLA-100 Steel .....	54
2.	454°C Aged HSLA-100 Steel .....	55
3.	621°C Aged HSLA-100 Steel .....	62
4.	677°C Aged HSLA-100 Steel .....	70
5.	Transformation Product Packet Dimensions .....	74
V.	SUMMARY .....	76
A.	CONCLUSIONS .....	76
1.	Inclusion Study .....	76
2.	Mechanical Properties .....	75
3.	Microstructure .....	77
B.	RECOMMENDATIONS .....	78
	APPENDIX A EQUILIBRIUM PHASE DIAGRAMS .....	80
	APPENDIX B DTRC TENSILE TEST DATA .....	94
	APPENDIX C DTRC CHARPY V-NOTCH IMPACT TEST DATA .....	95
	LIST OF REFERENCES .....	99
	INITIAL DISTRIBUTION LIST .....	103

## LIST OF TABLES

TABLE I.	HSLA-100 STEEL MIL-S-24654A COMPOSITION (WEIGHT PERCENT) .....	5
TABLE II.	HSLA-100 STEEL LOT GQH CHEMICAL COMPOSITION .....	35
TABLE III.	HSLA-100 STEEL STRENGTH AND TOUGHNESS REQUIREMENTS .....	51

## LIST OF FIGURES

Figure 1. HSLA-100 Steel Continuous Cooling Transformation Diagram [Ref. 16:p. 262] .....	8
Figure 2. Graville Diagram [Ref. 1:p. 16] .....	10
Figure 3. Hydrogen-induced Cracking in a Transverse Section [Ref. 16:p. 119] .....	11
Figure 4. Effect of Copper on Average Hydrogen-Induced Crack Length [Ref. 16:p. 120] .....	12
Figure 5. Effect of Ferrite Grain Size on 0.2% Proof Stress [Ref. 7:p. 112] ....	15
Figure 6. Cleavage Crack Deflection at Bainite Packet Boundary [Ref. 20:p. 1533] .....	16
Figure 7. Fe-Cu Phase Diagram [Ref. 11:p. 8]] .....	21
Figure 8. Effect of Sulfide Volume Fraction on Total Ductility at Fracture [Ref. 7:p. 82] .....	26
Figure 9. Lamellar Tearing in Welded Structure [Ref. 18:p. 364] .....	27
Figure 10. (a) Elongated Manganese Sulfide Inclusions in Quenched and Tempered Steel Without Inclusion Shape Control; (b) Globular Inclusions Found in Hot-Rolled Low Alloy Steel With Inclusion Shape Control [Ref. 18:p. 369] .....	29
Figure 11. Effect of Calcium Treatment on the Susceptibility to Lamellar Tearing [Ref. 35:p. 159] .....	30
Figure 12. Effect of Sulfur Content on Charpy Impact Energy [Ref. 18:p. 368] .....	31
Figure 13. Relation Between Calcium Oxygen Content of Steels Treated with Ca Si [Ref. 34:p. 12] .....	32
Figure 14. Inclusions Elongated in Rolling Direction. ....	39
Figure 15. Large Non-Deformed Inclusion with Fish Tails. ....	40
Figure 16. Inclusion Distribution From Optical Study. ....	41



Figure 17. Inclusion Distribution From SEM-EDX Study. ....	43
Figure 18. Distribution of Oxide Inclusions. ....	44
Figure 19. A Large Spinel Oxide Inclusion. ....	45
Figure 20. EDX Analysis of Spinel Oxide Inclusion. ....	45
Figure 21. Elongated Corundum Oxide Inclusion. ....	46
Figure 22. Distribution of Oxysulfide Inclusions. ....	47
Figure 23. Oxysulfide Inclusions. ....	48
Figure 24. EDX Analysis of Oxysulfide Inclusion. ....	48
Figure 25. HSLA-100 Steel Lot GQH 0.2% Yield Strength and Impact Energy at -84° C as a Function of Aging Temperature. ....	52
Figure 26. HSLA-100 Steel Lot GQH Tensile Strength. ....	53
Figure 27. HSLA-100 Steel Lot GQH DBTT Behavior for Various Aging Temperatures. ....	53
Figure 28. HSLA-100 Steel Lot GQH Ductility: Variation of Elongation and Reduction of Area With Aging Temperature. ....	54
Figure 29. SEM Micrograph of As-quenched Transformation Product Packets. ...	56
Figure 30. TEM Image Showing Acicular Ferrite (Bainite), Lath Martensite, and Retained Austenite in As-quenched Sample. ....	56
Figure 31. TEM Image of Twin Martensite in As-Quenched Sample. ....	57
Figure 32. TEM Dark Field Image of Retained Austenite at Lath Boundaries of Martensite in As-quenched Sample. Imaged Using $\bar{g}=111$ of Austenite. ....	57
Figure 33. SEM Micrograph of 454°C Aged Transformation Product Packets. ...	58
Figure 34. TEM Image Showing 454°C Aged HSLA-100 Steel Lath Structure. ...	60
Figure 35. TEM Image of 454°C Aged HSLA-100 Steel Copper Coherent Strain Fields in Bainite Lath. ....	60
Figure 36. TEM Image of 454°C Aged HSLA-100 Steel Intralath Carbide ....	61
Figure 37. EDX Spectra of 454°C Aged HSLA-100 Steel Carbide. ....	61
Figure 38. Micrographs of 621°C Aged HSLA-100 Steel Transformation Product Packages: (Top) Light Micrograph, (Bottom) SEM Micrograph ....	64

Figure 39. TEM Image of 621°C Aged HSLA-100 Steel Lath Structure . . . . .	65
Figure 40. TEM Image Showing Copper Precipitates Decorating Dislocations and Lath Boundaries in 621°C Aged HSLA-100 Steel. . . . .	65
Figure 41. TEM Image of Copper Precipitates in 621°C Aged HSLA-100 Steel: (Top) Bright Field, $\vec{B}$ Close to $\langle \bar{1}13 \rangle$ , $\vec{g}=110$ ; (Bottom) Dark Field . . . . .	66
Figure 42. Intralath Nb-Mo Carbide (500 Å) in 621°C Aged HSLA-100 Steel: (Top) TEM Image; (Bottom) EDX Spectra. . . . .	67
Figure 43. TEM Image of Nb-Mo Carbide (350 Å) at Triple Junction in 621°C Aged HSLA-100 Steel. . . . .	68
Figure 44. TEM Image of Interlath 621°C Aged HSLA-100 Steel Molybdenum Carbide (1000 Å) . . . . .	68
Figure 45. Interlath Molybdenum Carbide (1000 Å) in 621°C Aged HSLA- 100 Steel: (Top) TEM Micrograph; (Bottom) EDX Spectra. . . . .	69
Figure 46. Light Micrograph of 677°C Aged HSLA-100 Transformation Product Packets . . . . .	72
Figure 47. TEM Image of 677°C Aged HSLA-100 Steel Lath Structure. . . . .	72
Figure 48. TEM Image of Intralath Copper Precipitates and Interlath Carbides in 677°C Aged HSLA-100 Steel Lath Structure . . . . .	73
Figure 49. TEM Image of Intralath Carbides and Copper Precipitates. . . . .	73
Figure 50. TEM Image of Interlath Molybdenum Carbide in 677°C Aged HSLA-100 Steel. . . . .	74
Figure 51. Variation of Transformation Product Packet Size with Aging Temperature . . . . .	75
Figure 52. Variation of Bainite/Martensite Lath Widths with Aging Temperature. . . . .	75

## **ACKNOWLEDGMENTS**

I would like to thank Dr. Alan G. Fox for his technical guidance and supervision while working on this thesis, as well as Ms. Elisabeth Grayson for her technical support. Dr. Roy Crooks' assistance in printing the micrographs is also appreciated.

## I. INTRODUCTION

The structures of modern warships are subjected to a complex array of dynamic loadings and stresses during the life cycle of the ship. These stresses result from many sources, including fabrication, waveloading, machinery vibrations, aircraft/helo landings and possible explosive shock waves from weapons detonations. The hull also experiences thermal excursions due to operations in both arctic and tropical seas. [Ref. 1:pp. 1-2]

The material used for naval construction must therefore meet stringent strength and fracture toughness requirements imposed by the above conditions. The HY series of steels have traditionally met these requirements, but their higher concentration of carbon (added for increased strength) has had an adverse effect on the steel's weldability [Ref 2:p. 26]. Post-weld cracking in these martensitic steels is a major concern and is prevented by expensive fabrication procedures including preheat requirements, interpass temperature limits, heat input limits, welder training and qualification and intensive inspection procedures [Ref 1:p. 2].

In an effort to reduce shipbuilding and repair costs, the U.S. Navy has maintained a continuous research, development, and certification program in high strength low alloy (HSLA) steels [Ref 2:p. 3]. These steels use microalloying and thermomechanical processing to obtain the required mechanical properties for ship structures [Ref 2:p. 3]. Unlike the HY series, though, HSLA steels possess excellent weld characteristics. These low carbon martensite/bainite alloys have lower carbon levels resulting in a softer

microstructure which is more resistant to hydrogen cracking [Ref 3:p. 68.] [Ref 4:p. 4]. The need for preheat is eliminated resulting in cost reductions and increased productivity in shipyards [Ref 5:p. 2.] [Ref 6:pp. 21-26].

In 1985, a program was initiated to develop HSLA-100 steel as an alternative to the HY-100 steels which had been used extensively in submarine non pressure hull designs and surface combatant's topside structures [Ref 1:p. 3] [Ref 3:p. 64]. HSLA-100 is a solution treated, quenched and aged, low carbon, copper precipitation strengthened steel designed to meet the strength (690 MPa) and toughness of HY-100 steel, but with improved weldability [Ref 5:p. 1]. The high fracture toughness inherent in this steel is due to the tempered bainitic microstructure and the dispersion of secondary transformation products throughout the homogeneous microstructure [Ref 3:p. 67]. Ductility and transverse toughness are improved due to calcium treatment which controls inclusion morphology [Ref 7:pp. 81-83]. Developed and commercially produced within a four year period, HSLA-100 has been recently certified and is now being used in the construction of CVN-74, CVN-75, SSN-785, and SSBN-726 class ships [Ref 2:p. 3].

The Navy hopes to eventually design 130 and possibly 150 ksi yield strength steels amenable to high technology welding processes [Ref 1:p. 11]. Before this goal can be realized, the basis for the excellent strength and toughness properties in HSLA-100 steel must be understood. Explanations for the mechanical behavior of the material can be found from an in-depth analysis of the microstructure using principles of physical metallurgy. Optical, scanning electron, and transmission electron microscopy were used in the present work to determine the size, distribution, and composition of non-metallic

inclusions and to characterize the bainitic/martensitic matrix found in the overaged steel.

This research is conducted in conjunction with David Taylor Research Center's effort in certifying the HSLA series of steels.

## **II. BACKGROUND**

### **A. CHARACTERISTICS OF HSLA STEEL**

Technological advances in steel processing and a better understanding of microalloying and structure-property relationships have all contributed to the development and increased utilization of HSLA steels. Approximately 7% of all steels made in the United States is of the high strength low alloy variety; this percentage is expected to grow in the future [Ref. 8:p. 41]. Economic considerations have also factored in their use; close matching of strength with other property requirements have realized cost savings of 30% over plain carbon steels [Ref. 9:p. 17]. Generally defined as having a yield strength above 275 MPa, these steels combine alloy additions such as vanadium, titanium, and niobium, and thermomechanical processing to achieve a desired microstructure that will guarantee high strength, toughness, and formability. [Ref. 9:p. 14]

The amount of research that has been invested in these steels is staggering; it has not been haphazard either, but has been based on planned, systematic research [Ref. 8:p. 41] [Ref. 7:p. 61]. The latest innovation in processing is the use of Ladle Metallurgy to improve the through-thickness ductility and toughness in steels by influencing the morphology of non-metallic inclusions [Ref. 10]. Also, by applying new metallurgical principles, the amount of carbon continues to be reduced in the steel while maintaining the required strength. The evolution of HSLA steels continues with new chemistries produced and better mechanical properties attained every day.

The Navy is interested in this family of steels and has appropriated resources for the research and development of HSLA-100 steel to be used in ship construction. A derivation of the successful ASTM-A710 commercial product, this steel is a solution treated, quenched and aged, highly weldable, low carbon, copper precipitation strengthened steel designed to achieve a yield strength of 690 MPa. The chemical composition according to MILSPEC MIL-S-24645A for HSLA-100 steel is listed in Table I. [Ref. 5:p. 3]

**TABLE I. HSLA-100 STEEL MIL-S-24654A COMPOSITION  
(WEIGHT PERCENT)**

C	0.04-0.06
Mn	0.75-1.05
P	0.020
S	0.006
Si	0.40
Ni	3.35-3.65
Cr	0.45-0.75
Mo	0.55-0.65
Cu	1.45-1.75
Nb	0.02-0.06

Strength is an important parameter in HSLA steels and is defined as a measure of a material's resistance to plastic flow [Ref. 11:p. 18]. Unlike HY steels which attain their



strength from quench and temper heat treatments, HSLA steels achieve their strength through alternate mechanisms including grain refinement, precipitation strengthening, and solid solution strengthening [Ref. 12:pp. 5-22]. Dislocation substructures, produced either by mechanical processing or by a bainitic/martensitic type of phase transformation, also contribute to the material's strength [Ref. 5:p. 3]. The above strengthening mechanisms all reduce dislocation mobility and increase the stress required to move these dislocations through the steel [Ref.11:p. 21].

Carbon is an excellent solid solution strengthener increasing the yield stress 4600 MPa for each 1% added [Ref. 7:p. 70]. However, the Navy's stipulation that the new steel be low in carbon (for improved weldability) virtually eliminates the contribution of this strengthening mechanism to HSLA-100 steel; the remaining alloying elements do not offer significant solid solution strengthening. Deformation processing, such as rolling and forging, was also not mentioned in the Navy's requirements. Therefore, the yield strength of HSLA-100 would be based primarily on grain refinement, precipitation strengthening, and transformation induced substructures. [Ref. 5:pp. 3-4]

It has been well documented in the literature that improved yield stresses are achieved by grain refinement of the ferrite resulting from the allotropic transformation of the parent austenite. The primary source of strength in HSLA-100 steel is the fine grained bainitic microstructure which evolves from the refined prior austenite structure [Ref. 13:p. 6]. Smaller grains also have a beneficial effect on the ductile to brittle

transition temperature. The dependence of both properties follows a Hall-Petch relationship. [Ref. 14:p. 1657]

Transformation substructures and precipitation strengthening together account for approximately 138 MPa in yield strength. Alloy additions lower the Bainite transformation temperature and consequently increase the density of dislocation substructures produced by the transformation of austenite to bainite. The strength is raised by this increase in density dislocation. Precipitation of  $\epsilon$ -copper particles and carbides also increases strength during aging. [Ref. 5:pp. 3-8]

Toughness is also an important material parameter and is improved in HSLA-100 steel by: refining the prior austenite grain size; reducing the carbon content and thereby the volume fraction of both pearlite and grain-boundary carbides; ensuring that particles present to increase strength are equiaxed and homogeneously distributed; and by controlling the size, shape and distribution of inclusions [Ref. 15:p. 2055].

## **B. THE EFFECTS OF MICROALLOYING**

Successful microalloying in HSLA-100 steel development is the key to this steel's excellent mechanical properties. Alloy additions affect every strengthening mechanism in steel with the exception of mechanical processing. Alloying changes the positions of each transformation region in the continuous cooling transformation (CCT) curves, causing different austenite transformation characteristics (Figure 1). Increased alloying also promotes structural refinement by lowering the Bainite start (BS) and Martensite start

(MS) temperatures. The shift in the CCT "nose" to longer transformation times increases the size of the austenite field and allows the formation of Bainite with its high dislocation density and martensite. [Ref. 16:pp. 260-263] [Ref. 13:pp. 7-8]

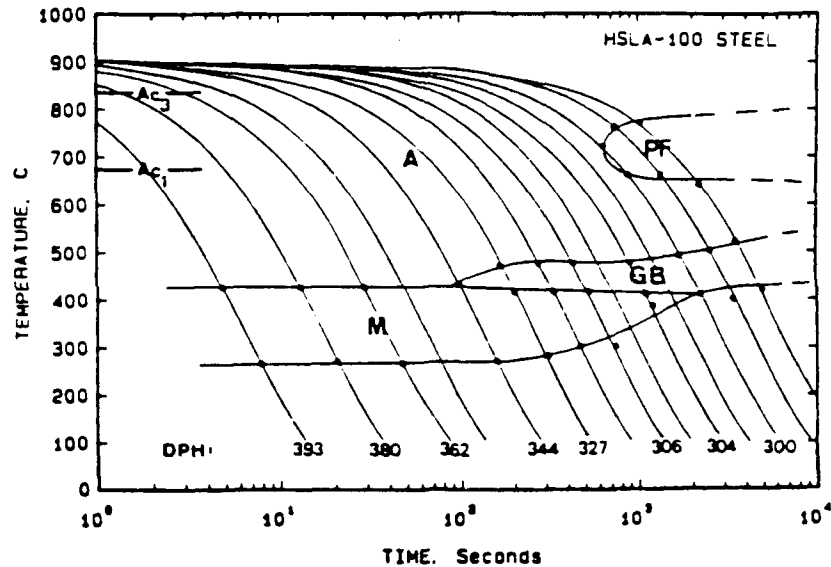


Figure 1. HSLA-100 Steel Continuous Cooling Transformation Diagram [Ref. 16:p. 262]

Listed below are the metallurgical significance of each of the important alloying elements:

- **Carbon** - Increases in carbon content improves the steel's ability to form martensite which increases strength. Carbon also is an excellent solid solution strengthener. Lower carbon content leads to improved toughness and a lower ductile-brittle transition temperature (DBTT) since fewer crack-initiating carbides exist. Low carbon concentrations also provide a highly weldable steel insensitive to hydrogen-induced cracking (HIC); the need for pre-heat can also be eliminated. [Ref. 3:pp. 64-65]

- **Manganese** - Reacts with sulfur to form MnS, preventing the formation of harmful FeS at grain boundaries which causes 'hot cracking'. Mn is also a good deoxidizer when combined with silicon [Ref. 17:p. 19] and lowers the DBTT and elevates strength when in solid solution. [Ref. 18:p. 376]
- **Copper** - Increases strength by precipitation of copper-rich particles during aging [Ref. 16:p. 260]. Improves corrosion resistance to seawater and reduces susceptibility to hydrogen induced cracking [Ref. 16:p. 67].
- **Nickel** - Increases strength by enhancing grain refinement and solid solution strengthening; Ni reduces the DBTT but does not affect Charpy upper shelf energy [Ref. 18:p. 391]. Prevents the hot shortness phenomenon associated with welding of steels containing copper. Dramatically increases hardenability and promotes higher toughness [Ref. 16:p. 260].
- **Niobium** - Combines with nitrogen and carbon to form niobium carbonitrides Nb(C,N) which provide grain refinement during hot rolling and later austenitizing treatment by pinning the austenite grain boundaries. Increases strength through carbide and nitride formation. [Ref. 16:p. 260]
- **Molybdenum** - Increases strength without loss in toughness. Strong carbide former; influences transformation kinetics by delaying the onset of proeutectoid ferrite formation; suppresses temper embrittlement. [Ref. 16:p. 260]
- **Vanadium** - Strong carbide and nitride former [Ref. 18:p. 376].
- **Silicon** - Excellent deoxidizer; prevents porosity during steelmaking. [Ref. 19:p. 8]
- **Chromium** - Increases hardenability of bainite by delaying onset of proeutectoid ferrite formation; retards tempering during aging; provides corrosion resistance; strong carbide former. [Ref. 16:p. 260] [Ref. 18:p. 376]
- **Aluminum** - Lowers DBTT by removing nitrogen from solid solution which lowers the lattice resistance to dislocation motion; strong deoxidizer. Forms AlN which pins grain boundaries and keeps ferrite grain size small. [Ref. 8:p. 47] [Ref 13:p. 9]

The main purpose of microalloying in HSLA-100 steel is to increase strength through refinement of grain size and precipitation strengthening. Carbon is then not

necessary for strength and can be reduced, improving the weldability and toughness of the steel. The Graville diagram, Figure 2, illustrates the impact of low carbon content on weldability. Three regions are depicted on the diagram which predict the ease with which a steel can be welded. The traditional steels, HY-80 and HY-100, lie in zone III which is difficult to weld and requires costly welding procedures. HSLA-100 steel, with its low carbon content, is found in the easily weldable zone.

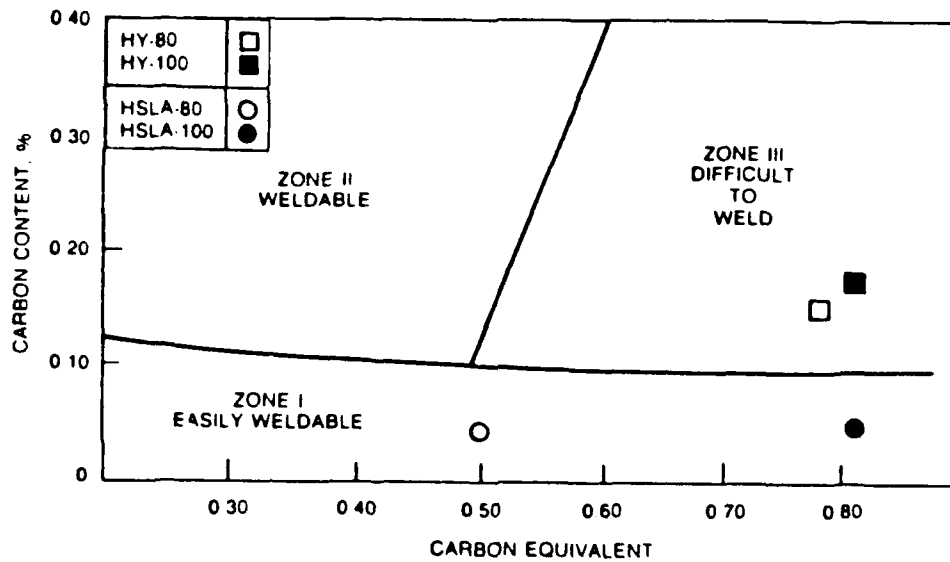
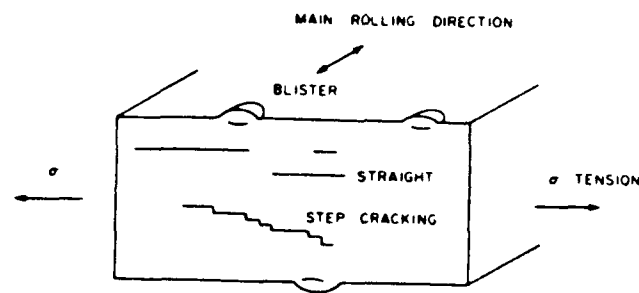


Figure 2. Graville Diagram [Ref. 1:p. 16]

As stated earlier, microalloying additions, especially copper, help eliminate the deleterious effects of hydrogen-induced cracking; this phenomenon can begin with hydrogen entering the steel as a result of a corrosion reaction in a wet  $H_2S$ -containing environment. The hydrogen then diffuses to the inner surfaces of voids or existing cracks

where its pressure can be raised dramatically to as much as a few thousand atmospheres. Larger cracks then initiate and propagate, principally at MnS inclusions, to relieve this pressure. Basically, there exists two cracking modes: (1) straight cracking parallel to the rolling plane, and (2) stepwise cracking, which occurs when adjacent parallel cracks interconnect and propagate through the thickness of the material (Figure 3). Copper addition suppresses the hydrogen entry into the steel by the formation of a protective surface film. Copper treated steels containing low amounts of sulfur show a decrease in average crack length as the amount of copper content increases (Figure 4). [Ref. 16:pp. 118-119]



**Figure 3. Hydrogen-induced Cracking in a Transverse Section**  
[Ref. 16:p. 119]

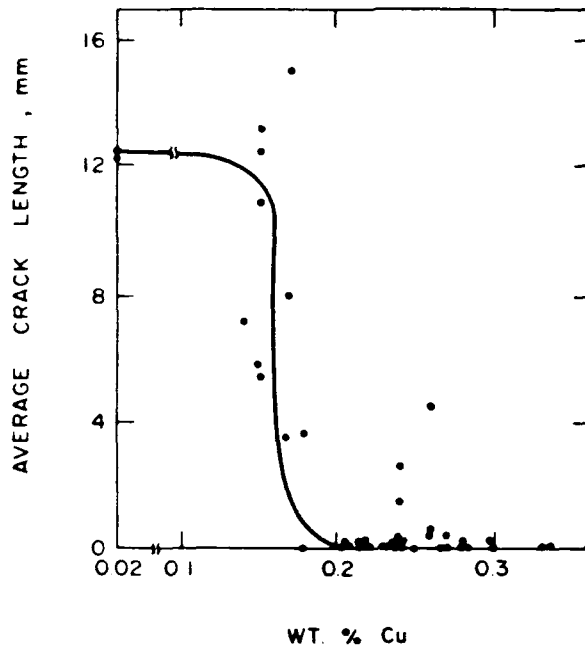


**Figure 4. Effect of Copper on Average Hydrogen-Induced Crack Length [Ref. 16:p. 120]**

### **C. STRUCTURE-PROPERTY RELATIONSHIPS IN BAINITIC STEELS**

The bainite structure found in HSLA-100 steel has been the subject of much recent research and is believed to represent the current frontier of the science of phase transformations [Ref. 20:p. 1527]. Although its exact mechanism of formation is not clearly understood, most metallurgists now agree that bainite has a positive influence on the mechanical properties of steels. Consequently, a larger percentage of high strength

steels have been designed to possess the low carbon bainitic microstructure in order to achieve the best combination of strength and toughness.

Bainite is generally defined as a two phase microstructure consisting of carbide particles dispersed in a ferrite matrix which has an elongated, lathlike appearance [Ref. 21]. Bainite forms in low carbon steels by a shear transformation from austenite; this diffusion controlled process actually nucleates the ferrite first [Ref. 7:p. 110].

There are two general classes of bainite which are differentiated by their basic morphology, their transformation temperature, and their orientation relationship between the ferrite and the carbides [Ref. 7:p. 110]. "Upper" bainite forms with carbides between ferrite laths at relatively higher transformation temperatures, while "lower" bainite forms at lower temperatures with the carbides contained entirely within the ferrite [Ref. 20:p. 1528].

Pickering provides the following characterization of upper bainite [Ref. 7:pp. 110-111]:

The ferrite forms by shear as plates or laths, which co-operatively nucleate side by side in packets. It occurs at temperatures above 350°C in steels containing > 0.6% C, but at somewhat higher temperatures in lower carbon steels. At the temperatures at which upper bainite forms, carbon is sufficiently mobile to diffuse in the austenite in front of the growing bainitic ferrite. Thus carbon-enriched austenite is entrapped between the bainitic ferrite laths. This carbon-enriched austenite can be retained, can form high-carbon martensite, or can form  $\text{Fe}_3\text{C}$  between the ferrite laths, depending upon the composition, degree of carbon enrichment, rate of cooling or transformation temperature. If the structure contains retained austenite or martensite it may be termed granular bainite. The general structure comprises carbide films or elongated particles lying between the bainitic ferrite laths, i.e. at the lath boundaries. The lower the transformation temperature, the finer are the



bainitic ferrite laths and the smaller and more numerous are the carbides at lath boundaries. The higher the carbon content, the finer are the bainitic ferrite laths and the more numerous and continuous are the carbide films between the ferrite laths, so that the structure may take on a pearlitic aspect.

In lower bainite, carbon cannot diffuse as rapidly from the growing ferrite at the lower transformation temperatures. Consequently, the ferrite plates contain supersaturated carbon. To maintain the driving force for the reaction, the carbide precipitates as small plates within the ferrite laths. Thus, lower bainite often has a platelike morphology. Lower transformation temperatures also produce finer bainitic ferrite laths and smaller, more numerous carbides. [Ref. 7:p. 111]

The excellent strength exhibited by bainitic steels is due to four separate factors [Ref. 20:pp. 1531-1532]:

- **Lath strengthening** - numerous studies have shown that lath width and bainite packet size affect strength; the flow stress usually varies with the reciprocal of some characteristic lath dimension. Pickering showed that the ferrite grain size (bainitic lath size) gives the usual Petch relationship with 0.2% proof stress (Figure 5). The lath dimensions decrease with decreasing transformation temperature.
- **Dislocation strengthening** - transformation strains induce a higher density of dislocations which increase strength. As transformation temperature decreases, the density of dislocations increases.
- **Interstitial and substitutional strengthening** - the carbon dissolved in the bainitic ferrite causes solid solution strengthening. Experimental evidence also shows a residual super-saturation of carbon atoms can interact with dislocations to increase the strength significantly.
- **Carbide strengthening** - In upper bainite the coarser particles at the lath boundaries impede dislocation motion but do not appear to affect the strength of the microstructure via dispersion strengthening. In lower bainite, the increased number

of fine intralath carbides per unit planar section increases the proof stress [Ref. 7:p. 112].

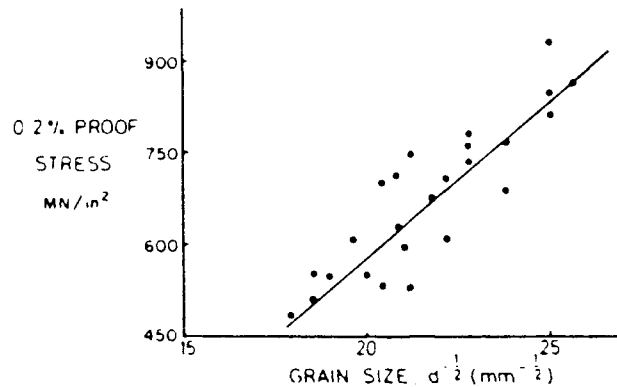


**Figure 5. Effect of Ferrite Grain Size on 0.2% Proof Stress [Ref. 7:p. 112]**

All of the above strengthening mechanisms increase in intensity as the transformation temperature decreases.

Bainite also possesses good toughness properties. Studies of the cleavage facet size have shown that this structural dimension is larger than the packet size, which suggests that the cleavage crack is deflected at the high angle bainite packet boundary as illustrated in Figure 6. This deflection impedes crack propagation and raises the fracture toughness of the steel. [Ref. 20:p. 1533].

Upper bainite exhibits different toughness properties than lower bainite. Large carbides crack to form a supercritical defect in upper bainite. Once started, the crack is

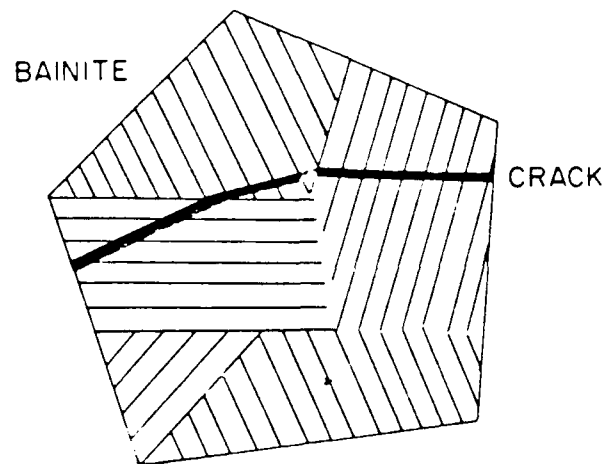


**Figure 6. Cleavage Crack Deflection at Bainite Packet Boundary [Ref. 20:p. 1533]**

not obstructed by the low angle bainitic ferrite boundaries. In lower bainite, crack initiation is more difficult due to the presence of smaller carbides. If a cleavage crack is initiated, however, its propagation is blunted by the numerous carbides and increased dislocation density. Thus, for equal strength, upper bainite has lower impact toughness than lower bainite. [Ref. 7:p. 116]

Bainitic steels can be designed for improved toughness. The impact transition temperature can be lowered in upper bainite by refining the prior austenite grain size through thermomechanical treatment and alloy additions. In lower bainite, a slight reduction of the strength by tempering will result in a lower impact transition temperature.

The tempering temperature is limited, though, since ferrite grain growth occurs at higher tempering temperatures and increases the impact transition temperature. [Ref. 7:p. 117]

#### **D. PROCESSING OF HSLA-100 STEELS TO ACHIEVE HIGH STRENGTH AND TOUGHNESS**

Thermomechanical treatment (TMT) is an important event in the development of HSLA-100 steels. In addition to attaining proper plate thicknesses, the process also plastically deforms the austenite microstructure before transformation; the result is a uniform fine grained bainitic microstructure with improvements in yield strength and toughness. [Ref. 22:p. 170]

The treatment begins with the reheating of the slab; certain complex carbonitrides formed from alloy additions will dissolve during this phase [Ref. 23:p. 62]. These microalloying elements will actually "condition" the austenite during TMT by performing one or more of the following functions [Ref. 22:p. 170]:

- Maintain the fine austenite grain size during reheating by increasing the grain coarsening temperature.
- Slow down the growth of recrystallized grains by pinning the grain boundaries.
- Retard or suppress recrystallization

Niobium carbonitride is one key ingredient that influences the austenite. It actually assists in flattening the austenite grain during later rolling operations. The resulting high ratio

of austenite grain boundary surface area to grain volume enhances the nucleation kinetics and a fine grain size is obtained during cooling. [Ref. 24:p. 25]

The rolling process is the next step in TMT. Conducted at high temperatures, each rolling pass is usually followed by rapid recrystallization and grain growth. But this does not occur since the carbonitrides now precipitate at substructural features in the deformed austenite. These fine second phase particles pin the substructure and inhibit recrystallization. These interactions make it possible to roll below a temperature where recrystallization does not occur between rolling passes. The plastically deformed grains then keep their flattened, pancake morphology which is desirable since it is the thickness of grains that controls the final grain size after phase transformation. [Ref. 23:p. 64]

The next evolution is the transformation of the refined austenite into a bainitic microstructure. For HSLA-100 steel, the transformation consists of austenization of the material, which serves the same function as slab reheating, followed by a quench [Ref. 1:p. 16]. The quench is critical since control of the bainite transformation temperature will affect grain size. Microalloying again assists in this process since the alloying elements actually lower the Bainite start temperature ( $B_s$ ). As the  $B_s$  is lowered, the number of bainite nucleation sites increases at the expense of bainitic grain growth, resulting in a smaller size. A fine grained microstructure supersaturated with copper and carbonitrides is the goal of the quench in HSLA-100 steel. The precipitation of

carbonitrides may occur during the quench due to their greater solubility in austenite than in bainite. [Ref. 13:p.11]

The strength and toughness of HSLA steels is dependent on the small grains produced during the thermomechanical processing. To achieve the higher strengths required in ship structures, though, precipitation strengthening from aging is also required. This is accomplished in HSLA-100 steels through the classic precipitation of copper. Additional strengthening also results from niobium and molybdenum carbides.

#### **E. THE AGING BEHAVIOR OF COPPER**

Although grain refinement is the main mechanism of strengthening in materials, it alone cannot provide the 690 MPa of yield strength required of HSLA-100 steel [Ref. 23:p. 66]. The Navy has stipulated that the additional strengthening be supplied by precipitation hardening. Dispersed precipitates generally increase strengthening by impeding dislocation motion; dislocations may be forced to bow around the hard particle (Orowan looping) or, in the case of weaker particles, may actually cut through the precipitate [Ref. 11:pp. 21-22]. Coherent precipitates cause the most hardening due to the large elastic-strain fields associated with their interface with the matrix. Dislocations are blocked by these strain fields. As aging time progresses, the coherent particles coalesce; the driving force for this coalescence is the reduction in the strain energy of the matrix. The resulting larger particles cause less strain in the adjacent matrix because of their larger radii. Incoherent precipitates are now formed from this coalescing; these particles

involve smaller elastic strains because the misfit of the matrix-precipitate interface is accommodated by dislocations. Dislocation motion is now easier and the strength of the material begins to decrease. [Ref. 25:pp. 319-324]

Copper is a precipitation strengthener that operates similar to the above classic aging mechanism; its presence in HSLA-100 steel is required to meet the yield strength requirement. As shown by the iron-carbon phase diagram, the maximum solubility of copper in iron is 2.1% and its decreasing solubility with decreasing temperature provides this opportunity for age hardening to be used (Figure 7). Copper can contribute up to 248 MPa during aging for each 1% of the element added to the alloy [Ref. 11:p.23]. Additional strengthening is also provided by precipitates of niobium carbonitrides. [Ref. 26:p. 791]

Goodman, Brenner, and Low have studied the precipitation of copper in iron using field ion microscopy. They discovered that aging of the supersaturated Fe-Cu alloy resulted in precipitation of copper-rich body centered cubic (BCC) clusters that formed in ferrite and grew by bulk diffusion. Maximum strength was attained during the precipitation of this coherent non-equilibrium phase while the precipitates were still BCC with an average diameter of 24 Å and an average copper content of 50%. During overaging, these clusters transform into larger face-centered cubic (FCC) equilibrium epsilon phase precipitates containing a larger amount of copper; their loss of coherency makes them visible in the transmission electron microscope [Ref. 27:p. 121]. The

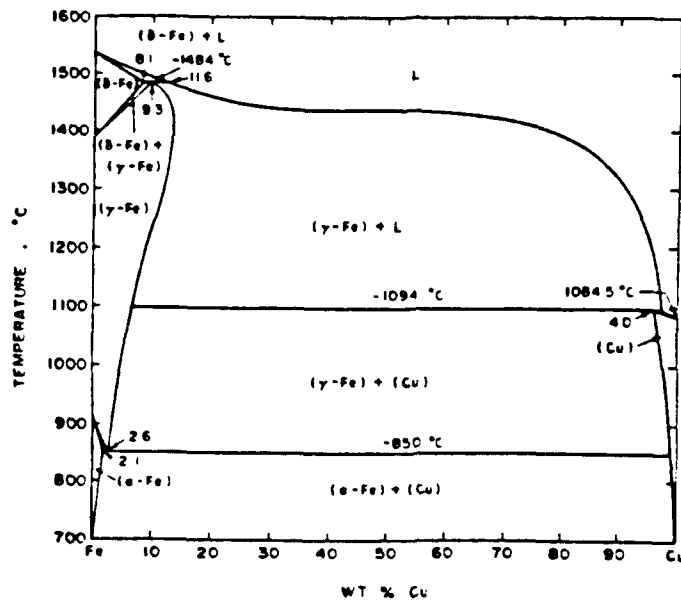


Figure 7. Fe-Cu Phase Diagram [Ref. 11:p. 8]

transformation from BCC to FCC relieves crystallographic strain and occurs when the precipitates reach a size of approximately 40 Å [Ref. 28:p. 803]. The incoherent particles were found to be spherical and randomly distributed throughout the matrix: as aging continued, the precipitates became rod-shaped [Ref. 29:p. 624]. The number density of precipitates remained nearly constant until peak strength was reached and then decreased during overaging. [Ref. 30, 31]

The mechanism of copper precipitation strengthening, however, is not clearly understood but numerous theories have been presented. Hornbogen suggested that



vacancies, causing jogs in screw dislocations, limited dislocation motion resulting in increased strength in copper alloys [Ref. 27:p.127]. Krishnadev and Le May believe the Orowan relationship is pertinent for correlating the strengthening effects observed in the overaged condition [Ref. 11; p. 26]. Strengthening due to differences in elastic moduli of particle and matrix was proposed by Russell and Brown [Ref. 32:p. 969]. Thus, detailed mechanisms contributing to the strengthening effect are still far from certain.

Although continued aging after peak hardness reduces the material's strength, it usually increases its toughness. The enhanced toughness of HSLA-100 is due in large part to the overaged condition of the copper precipitates [Ref. 33:pp. 244-248]. The larger, incoherent copper particles inhibit localized slip and formation of dislocation pileups at grain boundaries thereby increasing the upper shelf fracture toughness [Ref. 26:p.798].

## **F. INCLUSIONS IN STEEL**

HSLA-100, like all steels, is a composite material consisting of a metallic matrix with various second phase particles, including carbides and non-metallic inclusions. Usually originating during the molten steel refining operations, these second phase particles come in a variety of sizes, shapes, and compositions. Inclusions are present in every ton of steel produced and are a natural and inseparable component of the steel. A "clean steel" with only 1 ppm each of oxygen and sulfur will contain  $10^9$ - $10^{12}$  non-metallic inclusions per tonne; it is neither possible nor in some cases desirable to produce a steel completely free from these particles. Their uncontrolled presence, though, can have

serious deleterious effects on the mechanical properties of the steel. One of the goals of steel processing is to eliminate undesirable inclusions and control the nature and distribution of the remainder to optimize the properties of the final product. [Ref. 10]

### **1. Sources of Inclusions**

Understanding the origin of these particles is a first step in being able to control their effects. Non-metallic inclusions fall into two groups, those of exogenous and those of indigenous origin. The former are usually characterized by their unusually large size, irregular shape, sporadic occurrence, and complex structure. They form as a result of the molten steel coming in contact with refractories, trapped ladle slags, etc., and are generally composed of oxides. These foreign macroinclusions should be avoided since their large size is detrimental to the steel's properties [Ref. 17:part 3, p. i]. Indigenous inclusions, however, occur as a result of homogeneous reactions taking place in the molten or solidifying steel bath. The reactions that form them may be induced either by additions to the steel or simply by changes in solubility during the cooling and freezing of the steel [Ref. 17:part 3, p. 1]. Composed principally of oxides and sulfides, these inclusions are inherent structural components of the steel. Their quantity, size, shape, distribution, and composition can be modified but the presence of these inclusions can never be avoided. [Ref. 17:part 3, p. 74]

Most inclusions are hybrids of the two sources; they form by indigenous precipitation of manganese, silicon, and aluminum on exogenous nuclei during all the

different stages of the steelmaking process. Their composition in the steel bath and even in the solid steel continuously changes. [Ref. 17:part 3, pp. 1-2]

Although it is possible to trace the origin of different types of non-metallic inclusions, their growth, coalescence, rise in the steel bath, detachment from the molten steel, and general behavior is not fully understood. [Ref. 17:part 3, pp. 3]

## **2. Composition of Inclusions in Steel**

Two main families of inclusions exist in steels, oxides and sulfides. Dominating the oxide group is the system  $\text{MnO-SiO}_2\text{-Al}_2\text{O}_3$ . These indigenous inclusions are of fundamental importance to the formation of all oxide inclusions in modern steels [Ref. 17:part 2, p. i].  $\text{MgO-SiO}_2\text{-Al}_2\text{O}_3$  and  $\text{CaO-SiO}_2\text{-Al}_2\text{O}_3$  are two other common oxide systems, but they are formed from exogenous sources. In aluminum killed and calcium treated steels, calcium aluminate inclusions ( $\text{CaO-Al}_2\text{O}_3$ ,  $\text{CaO-2Al}_2\text{O}_3$ ) are abundant. These inclusions are free of  $\text{SiO}_2$ ; they are hard and keep their spherical shape even after deformation of the steel matrix [Ref. 17:part 2, p. 45].

Sulfides are also a very influential class of non-metallic inclusions. In the molten phase, sulfur is extremely soluble. As the steel solidifies, sulfur's solubility decreases and it precipitates in the form of metal sulfides. Manganese sulfide is the predominate type of these inclusions. In calcium treated steels, though, these are hopefully transformed into the complex  $\text{CaMnS}$  inclusions which are less deformable. [Ref. 17:part 2, p. 97, Ref. 34:p. 8]

### **3. Effects of Inclusions on Steel Properties**

The study of inclusions is mandatory since they have a major impact on the mechanical behavior of steels. Properties such as fracture toughness, ductility, machinability, and fatigue resistance are largely affected by volume fraction, size, shape, as well as distribution of these second phase particles. [Ref. 17:part 3, pp. 74-107]

The major detrimental effect is produced when MnS inclusions are formed in the solute-enriched interdendritic liquid at the last stages of solidification. During hot rolling, these sulfides are elongated into "stringers" which cause undesirable mechanical anisotropies in the steel. [Ref. 34:p. 8]

Poor ductility in the through-thickness direction is a major result of these planar arrays of plastic inclusions. The ductility in HSLA steels has been found to decrease exponentially as the volume fraction of non-metallic inclusions, especially sulfides, increases (Figure 8). The mechanics of ductile fracture is well understood; the phenomenon is caused by the growth and coalescence of voids which are nucleated at hard particles such as inclusions. Inclusions at room temperature are harder than the surrounding matrix. This leads to stress and strain concentrations during matrix deformation which can produce voids by matrix-particle decohesion or by fracture of the particles. Voids nucleate more easily if the particle is rigid, has a low cohesion to the matrix, or has a low internal fracture strength. Voids first form at the larger MnS inclusions, then at the smaller oxide inclusions. The voids grow until their softening effect

on the matrix is so large that sudden strain localization occurs leading to failure.

[Ref. 10:pp. 145-147]

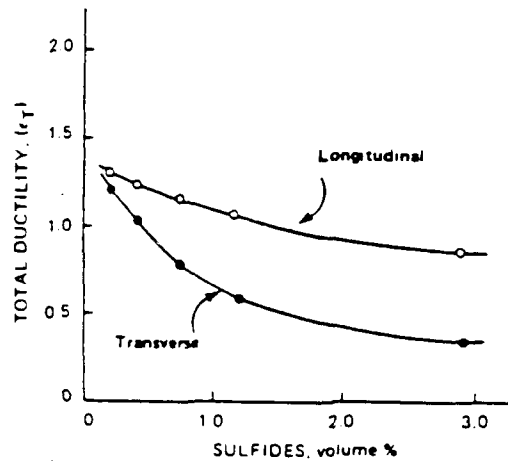


**Figure 8.** Effect of Sulfide Volume Fraction on Total Ductility at Fracture  
[Ref. 7:p. 92]

Lamellar tearing in large, restrained welded structures can also result from the presence of elongated sulfide inclusions [Ref. 34:p. 8]. Large through-thickness welding stresses initiate cracks which usually occur just outside the transformed heat affected zone (Figure 9). Having a characteristic stepped appearance, the cracks eventually lead to failure of the joint. [Ref. 10:pp. 109-110]

Toughness and fatigue resistance are also seriously degraded by inclusions. Acting as stress raisers, they cause shear deformation and crack nucleation in the steel. In the high cycle range ( $> 10^5$  cycles), nearly all cracks initiate from inclusions

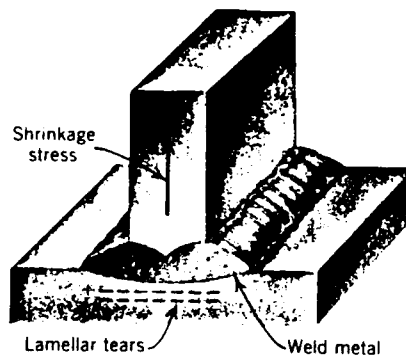


**Figure 9. Lamellar Tearing in Welded Structure [Ref. 18:p. 554]**

[Ref. 10:p. 135]. The Charpy impact shelf energy above the transition temperature is lowered due to the presence of inclusions [Ref. 7:p. 83]. Spherical oxide inclusions larger than 20  $\mu\text{m}$  are prime candidates for nucleating cracks. The critical size required for crack initiation decreases if the oxide particles ( $\text{Al}_2\text{O}_3$ ) are angular or if the stringer type is aligned perpendicular to the stress axis. Failure can result from fracture at the inclusion itself by separation of an internal phase boundary or by separation of the matrix/inclusion interface. Smaller inclusions were found to be unimportant for crack nucleation but may contribute to fatigue crack propagation. The propagation rate decreases with increasing cleanliness of the steel. [Ref. 17:part 3, pp. 43-44]

#### **4. The Role of Calcium on Inclusion Control**

The above deleterious effects of certain inclusions on mechanical properties can be significantly reduced by employing ladle metallurgy technology. This revolutionary processing technique involves bath stirring, slag-metal interaction, and the addition of alloying elements, such as calcium, to reduce the oxygen and sulfur contents of the steel. As a result, the number, size, composition, and morphology of the inclusions can be controlled and mechanical anisotropies eliminated. [Ref. 10:p. 44]

The injection of calcium is probably the greatest contributor to this optimization process of the inclusion population. It has been known for the past 20 years that calcium treatment can modify the morphology of inclusions [Ref. 10:p. 44]. The free energy of formation of CaO is the lowest among the common oxides (Appendix A); calcium therefore has a high affinity for oxygen [Ref. 17:part 3. p. 29]. These CaO products then react with the hard, angular  $\text{Al}_2\text{O}_3$  inclusions, forming complex CaO- $\text{Al}_2\text{O}_3$  or CaO- $\text{Al}_2\text{O}_3$ - $\text{SiO}_2$  inclusions that are molten at steelmaking temperatures and frequently float out of the melt. The result is a deoxidized steel containing fewer harmful aluminum oxide inclusions and more globular, less deformable calcium aluminates. [Ref. 10:p. 58]

Calcium addition has also proven successful in providing sulfide shape control and in generally reducing the amount of sulfur in the ladle. Molten calcium aluminate inclusions retained in the liquid steel react with sulfur during cooling and solidification such that there is little or no MnS accumulation in the interdendritic regions

[Ref. 34:p. 8]. The harmful manganese sulfide inclusions are reduced in number and size, and they are transformed to complex Ca-Mn sulfides which do not deform during hot rolling [Ref. 10:p. 58] (Figure 10). By calcium-assisted shape control of the sulfides and with the sulfur content limited to 0.005%, the sensitivity to lamellar tearing can practically be eliminated [Ref. 10:p. 110] (Figure 11).

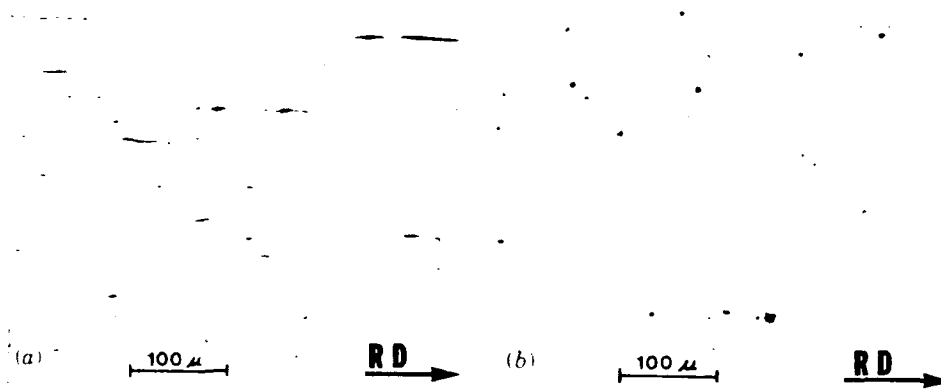


**Figure 10.** (a) Elongated Manganese Sulfide Inclusions in Quenched and Tempered Steel Without Inclusion Shape Control; (b) Globular Inclusions Found in Hot-Rolled Low Alloy Steel With Inclusion Shape Control [Ref. 18:p. 369]



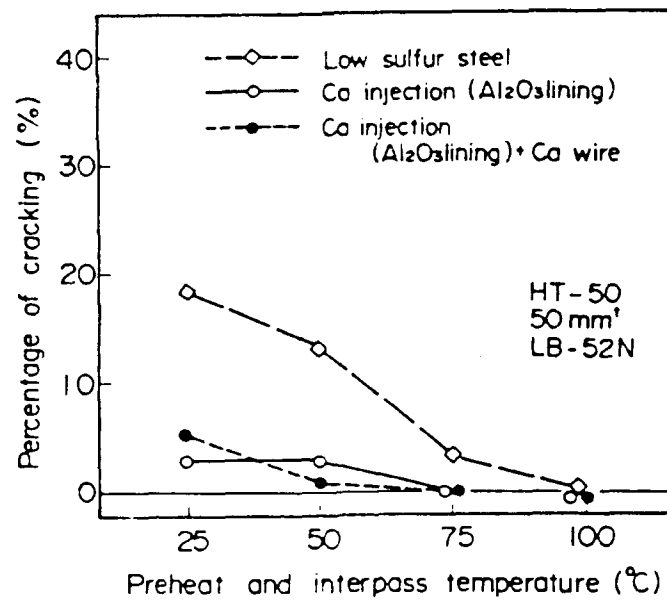


**Figure 11. Effect of Calcium Treatment on the Susceptibility to Lamellar Tearing [Ref. 35:p. 159]**

Calcium treatment thus lowers the oxygen and sulfur content in steels and modifies the oxide and sulfide inclusions that remain so that they are less deformable. These steels do not suffer the loss of toughness and ductility in the transverse direction. The upper shelf of the Charpy impact energy curve is greatly improved as the sulfur content is reduced (Figure 12). A high resistance to hydrogen-induced cracking (HIC) in HSLA steels can also be assured by lowering the sulfur and oxygen contents of the steel and by treating liquid steel with calcium to prevent the formation of MnS during solidification [Ref. 34:p. 9]. As stated earlier, copper additions also significantly reduce HIC problems.

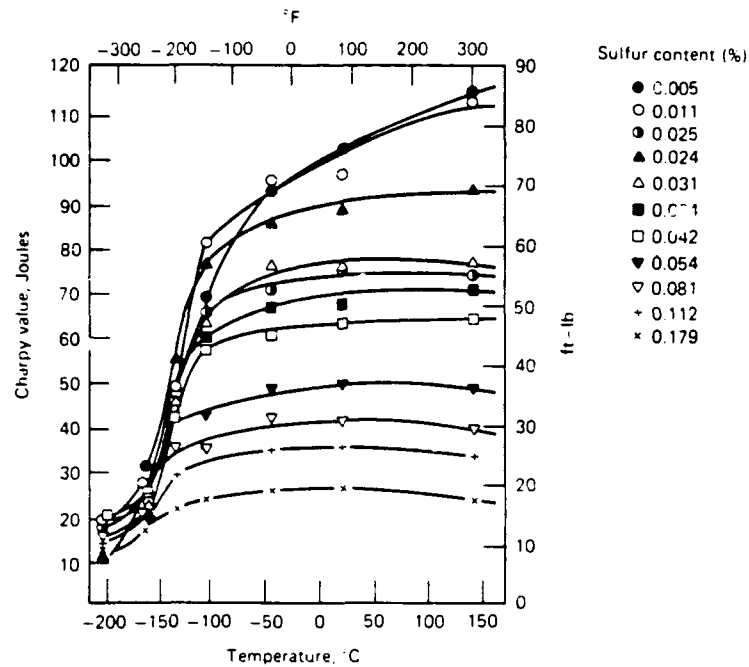


**Figure 12. Effect of Sulfur Content on Charpy Impact Energy [Ref. 18:p. 368]**

Machinability is also improved in calcium treated steels. The abrasive silica and alumina inclusions are converted to calcium silicate or aluminosilicate inclusions. These inclusions coat the carbide cutting tool by softening during machining. A protective barrier is provided that reduces tool wear and improves machinability. [Ref. 34:p. 8]

Calcium has also proven beneficial in eliminating nozzle blockage problems during casting which are characteristic in aluminum killed steels; it accomplishes this by modifying the indigenous inclusions responsible for the blockage [Ref. 36:p. 219]. Figure

13 shows the relation between calcium and oxygen content of low and high sulfur steels treated with CaSi. For a given total oxygen content of the steel, initially as alumina inclusions, a greater amount of calcium is returned in the low sulfur steels. Turkdogan found that for steels containing sulfur less than 50 ppm, there is almost complete conversion of alumina inclusions to molten calcium aluminate inclusions. These liquid steels are then easily cast without nozzle blockage. [Ref. 34:p. 5]

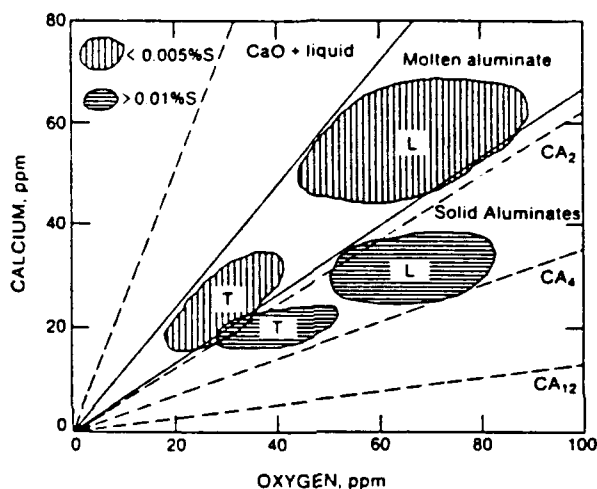


**Figure 13. Relation Between Calcium Oxygen Content of Steels Treated with Ca Si [Ref. 34:p. 12]**

## G. SCOPE OF PRESENT WORK

A certification program for the use of HSLA-100 steel in ship construction is currently being sponsored by David Taylor Research Center. Research on HSLA-100 to

date has been concerned with examination of the microstructure at various aging temperatures and verification of its excellent mechanical and welding properties. General consensus is that the strength is due to a fine-grained bainitic microstructure resulting from the refined prior austenite while the toughness is mainly attributed to the overaged copper precipitates.

In the present work, information regarding the size and distribution of non-metallic inclusions will be collected using optical and scanning electron microscopy while the composition of inclusions will be determined using energy dispersive x-ray analysis (EDX). Transmission electron microscopy will be used to study the bainitic matrix and to investigate the presence of carbides and copper precipitates. The purpose of this thesis is to examine the microstructural basis for the strength and toughness properties of overaged HSLA-100 steel.

### **III. EXPERIMENTAL PROCEDURE**

#### **A. MATERIAL**

David Taylor Research Center (DTRC), Annapolis, Maryland, provided one as-quenched and six heat treated HSLA-100 plate steel Charpy halves for this study. The samples (DTRC code GQH) were processed from the same cast manufactured by Lukens Steel Company. Produced in a 160 tonne electric arc furnace, the melt was aluminum killed, argon-injected with CaSi for inclusion shape control, and vacuum degassed. The heats were ingot cast with bottom pour molds to ensure good surfaces and sent to soaking pits for hot charging. After reheating to approximately 1177°C, the ingots were then cut into smaller slabs and rolled to a finishing temperature of 954°C and a thickness of 31.75mm [Ref. 8]. Charpy samples were cut from the plate along the T-L orientation. DTRC then re-austenized the samples for one hour before quenching. Six samples were then aged at temperatures of 399, 454, 510, 566, 621, and 677°C for 75 minutes. Table II shows the chemical composition of the samples as determined by DTRC. [Ref. 9:p. 26]

#### **B. MECHANICAL PROPERTIES**

DTRC performed Charpy V-notch impact energy, yield strength, tensile strength, and ductility testing for which all data was made available to the author. The tensile test

**TABLE II. HSLA-100 STEEL LOT GQH CHEMICAL COMPOSITION**

C	Mn	Mo	Cr	Cu	Ni
0.048	0.69	0.54	0.52	1.47	3.42
Nb	Si	N	S	O	P
0.020	0.27	0.0091	0.004	0 .0035	0.010

data is listed in Appendix B, and the Charpy V-notch impact energy data is found in Appendix C.

## **C. MICROSCOPY**

### **1. Optical Microscopy**

Optical microscopy was conducted for two reasons; first, to provide a statistical analysis of the size and distribution of inclusions within the specimen, and second, to analyze the etched microstructure.

For the inclusion study, the as-quenched sample was mounted and ground on successive emery paper to 600 grit and polished on 6  $\mu\text{m}$  and 1  $\mu\text{m}$  diamond wheels. The specimen was washed with soap, ultrasonically cleaned in ethanol, rinsed, and blown dry between polishing media and at the conclusion of final polishing. Extreme care was taken to maintain cleanliness since retained polishing media can contaminate the diamond wheels resulting in erroneous EDX analysis and poor surface finishes. Samples prepared

for inclusion studies must not be overpolished as small inclusions can be stripped from the matrix leaving holes.

The unetched specimen was then placed in a Zeiss ICM 405 photomicroscope and examined. In order to obtain a statistically significant number of inclusions, a total of 300 random fields were examined. Overlapping fields were avoided by locating a discernable landmark in the surrounding bakelite mount and then advancing along a vertical axis. After observing 25 fields, the sample was moved horizontally a significant distance to a new landmark before proceeding in the vertical direction to count 25 more fields. This process was repeated until a total of 300 fields were observed. When a field contained one or more inclusions, a picture was taken with the attached 35 mm camera. Care was taken to avoid "photographing inclusions" versus "photographing the sample" in order to analyze the inclusion distribution. The developed negatives were then placed on an overhead projector so the diameter of the enlarged 'spots' could be measured off the screen. After several trial exposures using different magnifications, the best results were found using the 80 objective which gave a negative magnification of 256X. Smaller objectives did not provide adequate resolution to measure inclusions smaller than three microns. The projector increased the magnification 10X, allowing a total magnification of approximately 2500X. By measuring the diameter of the 'spots' and knowing the total magnification of the image, the true sizes of the inclusions were found. Inclusion mean size, median size, and total surface fraction could then be calculated.

For optical microstructure analysis, a metallographic specimen was prepared from each of the Charpy samples and mounted, polished, and etched for approximately 30 seconds using a two percent nital etching solution. These samples were then examined and photographed at various magnifications.

## **2. Scanning Electron Microscopy**

A Cambridge Stereo Scan S200 Scanning Electron Microscope and Kevex 8000 Energy Dispersive X-Ray Analysis (EDX) Spectrometer were used to perform a second inclusion study consisting of 300 random fields at 1000X magnification. When an inclusion was observed, a chemical analysis was performed using the EDX which provided information on the inclusion's chemical composition. Spectra for each inclusion were collected and stored on memory tape. Micrographs of several inclusions using Back Scatter (BS) and Secondary Electron (SE) detectors were taken.

Microstructural features such as bainite/martensite packet size were examined and photographed from etched specimens of the Charpy samples. Dimensions of the bainite/martensite packets for the as-quenched, 454, 566, and 677°C were determined earlier by Mattes [Ref.13]. The packet size was determined from the SEM micrographs by employing a mean intercept method.

## **3. Transmission Electron Microscopy**

Thin wafers from the as-quenched, 454, 621, and 677°C aging temperature Charpy samples were cut from the low speed diamond wafer saw. Discs three mm in



diameter were then punched out and hand sanded on wet 600 grit silicon carbide paper to a thickness less than 0.025 mm. Discs were electrochemically thinned to perforation in a Struers Tenupol electropolishing device, operating at 70 volts, 0.5 amperes, and a medium flow rate using a 3 percent perchloric acid, 62 percent ethanol, and 35 percent n-butoxy ethanol solution, cooled to  $< -35^{\circ}\text{C}$  with liquid nitrogen. To remove copper that redeposited on the discs during the electropolishing process, the discs were ion milled in a Gatan Dual Ion Mill (Model 600) at room temperature using two guns at currents of 0.5 to 1 milliamperes for five minutes at an angle of 15 degrees. To characterize the microstructure and determine the bainite lath width, the discs were placed in a JEOL model JEM 100 CX transmission electron microscope operated at 120 KV. Composition of second phase particles such as carbides were analyzed using the Kevex energy dispersive X-ray analyzer. Spectra were collected and stored on memory tape. The bainite/martensite lath widths were measured from TEM micrographs using a mean intercept method.

## IV. RESULTS AND DISCUSSION

### A. INCLUSION STUDY

#### 1. Optical Microscopy

Examination of several HSLA-100 steel samples revealed numerous inclusions of a roughly uniform small size and coloration. Although the majority of inclusions observed were globular and homogeneously dispersed, some were elongated in the rolling direction with an apparent aspect ratio of 4 (Figure 14). A few very large non-deformed inclusions with the characteristic fish tails were also observed (Figure 15).

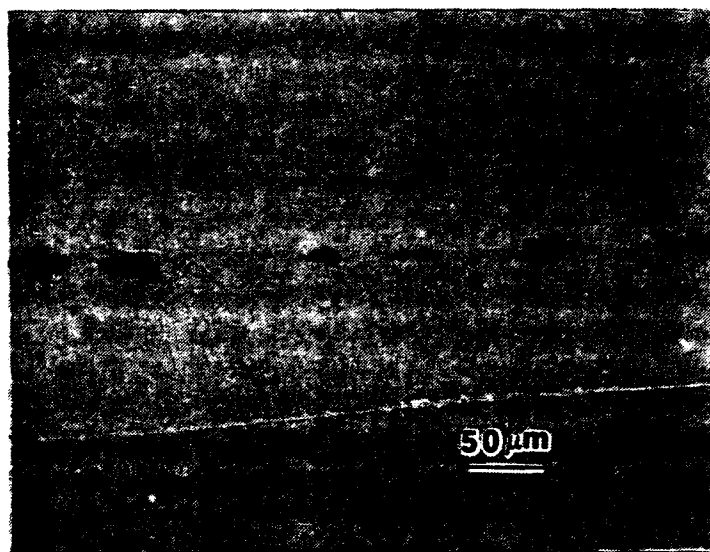


**Figure 14. Inclusions Elongated in Rolling Direction.**

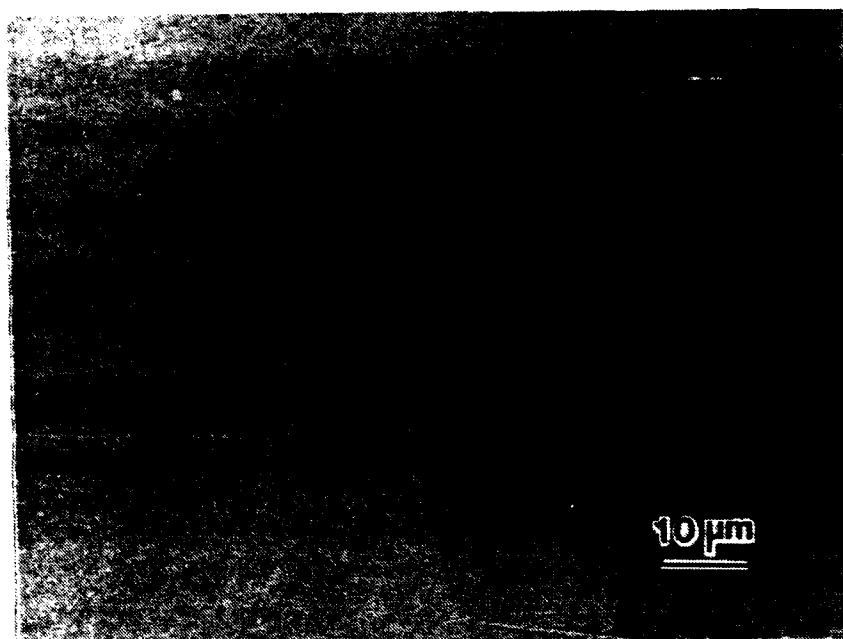


**Figure 15. Large Non-Deformed Inclusion with Fish Tails.**

In order to provide a statistical analysis, 300 random fields were observed using the optical microscope at a magnification of 256x. A total of 130 inclusions were counted; a histogram presenting their size distribution is provided in Figure 16. The mean and median sizes of inclusions were found to be 3.78  $\mu\text{m}$  and 2.84  $\mu\text{m}$  respectively; six inclusions larger than 10  $\mu\text{m}$  were observed, the largest approaching 34 $\mu\text{m}$ . The surface fraction of inclusions was determined to be 0.0365%.

The results of the optical study may be suspect since small "holes" and "dirt" (< 3  $\mu\text{m}$ ) may have been erroneously counted as inclusions. This consequence would result in a biasing of the histogram (Figure 16) to the left. The error may be compensated,

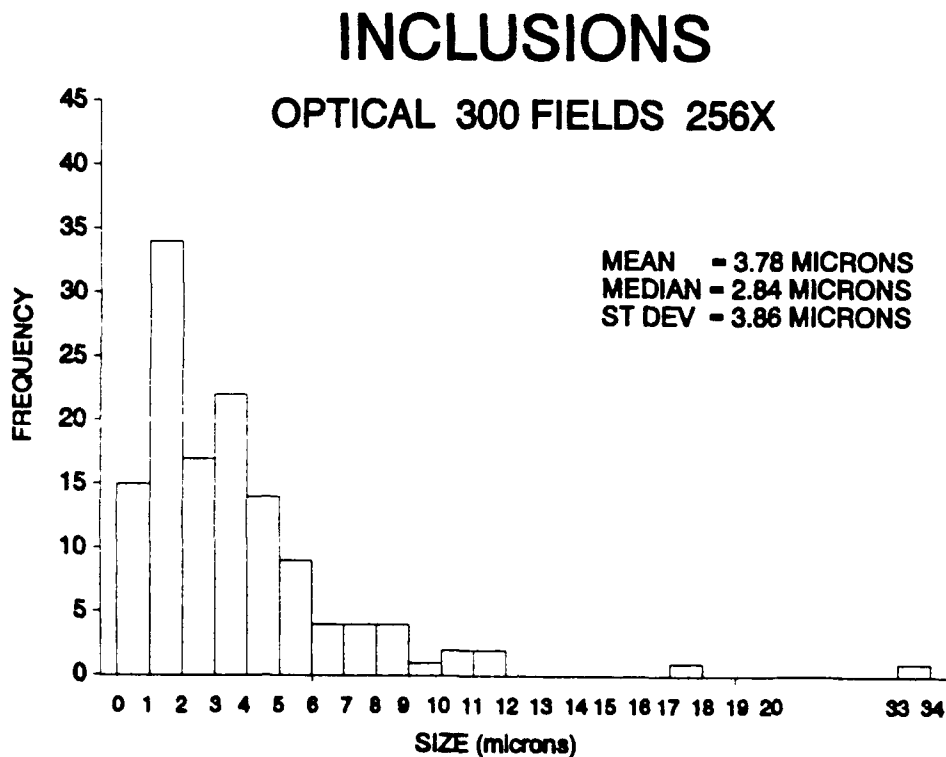


**Figure 16. Inclusion Distribution From Optical Study.**

though, due to the fact that inclusions smaller than  $0.375\ \mu\text{m}$  were not counted since they exceeded the limit of resolution of the microscope. Quantitative chemical analyses of the inclusions were also not provided by the optical study since it was difficult to visually distinguish between different inclusion types such as oxides or sulfides.

## 2. Scanning Electron Microscopy

HSLA-100 steels were also examined in the SEM/EDX in order to provide more statistical data on the inclusions and their respective compositions. 300 random fields were observed at a magnification of 1000x. A total of 56 inclusions were counted; the histogram showing their size distribution is presented in Figure 17. As expected, fewer inclusions were found in the SEM study since less surface area was observed at the 1000x magnification compared to the 256x magnification used in the optical microscope. The mean and median size of the second phase particles was determined to be 6.35  $\mu\text{m}$  and 4.23  $\mu\text{m}$  respectively. Significant in the statistical study were 10 inclusions found with a diameter larger than 10  $\mu\text{m}$ , the largest measuring 28  $\mu\text{m}$ . The surface fraction of inclusions, using their mean diameter, was calculated to be 0.0798%. This area was twice as large as the area covered by the inclusions in the optical study. Close inspection of the SEM histogram (Figure 17) shows several larger "outlying" inclusions and a larger standard deviation of sizes (5.54  $\mu\text{m}$ ). The median value of 4.23  $\mu\text{m}$  is probably a more accurate size for the "average" inclusion. The surface fraction using this median diameter is 0.0354% which is consistent with the optical value. EDX spectra were collected on each of the 56 inclusions "seen" in the SEM study; this allowed accurate identification and differentiation between inclusion types, such as oxides, oxysulfides, or pure sulfides.

A total of 26 inclusions were classified as pure oxides. With a mean size of 8.74  $\mu\text{m}$ , these particles were generally rather large and spherical in shape. Their size

# INCLUSIONS

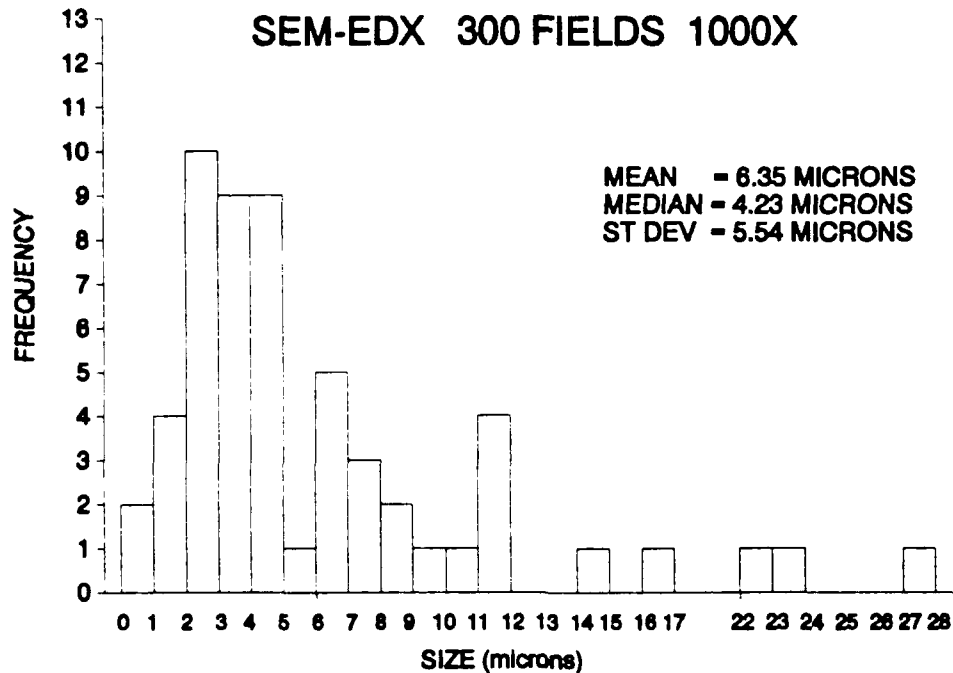


Figure 17. Inclusion Distribution From SEM-EDX Study.

distribution is shown in Figure 18. An extremely large oxide measuring 51  $\mu\text{m}$  in diameter was found outside of the random field study. This inclusion is shown in Figure 19 with the accompanying EDX spectra provided in Figure 20. Analysis indicated the particle possessed the following atomic percent composition: Mg (44.67%), Al (40.45%), Si (9.34%), and Ca (5.54%). From the known stoichiometries of  $\text{MgO}$ ,  $\text{Al}_2\text{O}_3$ , and  $\text{SiO}_2$ , the weight percent of each component in the inclusion was calculated. Reference to the

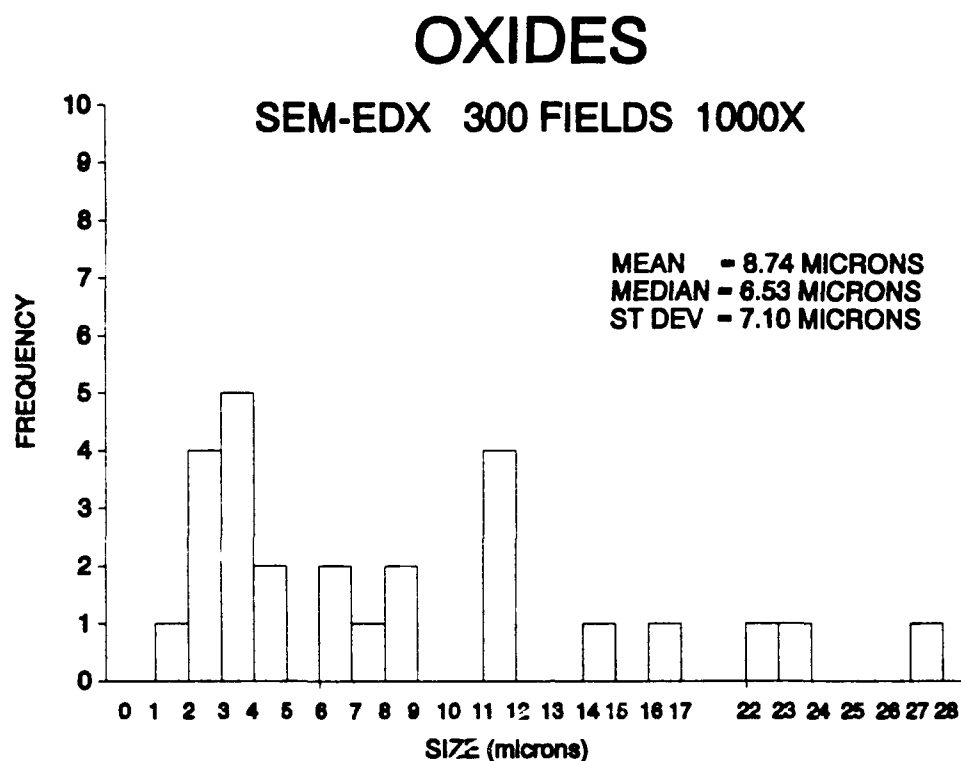


Figure 18. Distribution of Oxide Inclusions.

appropriate ternary phase diagram in Appendix A indicated a molecular composition of  $4\text{MgO} \cdot 5\text{Al}_2\text{O}_3 \cdot 2\text{SiO}_2$ . Commonly called spinel, this inclusion originated from an exogenous source and possessed a high melting point temperature of 2050 C.

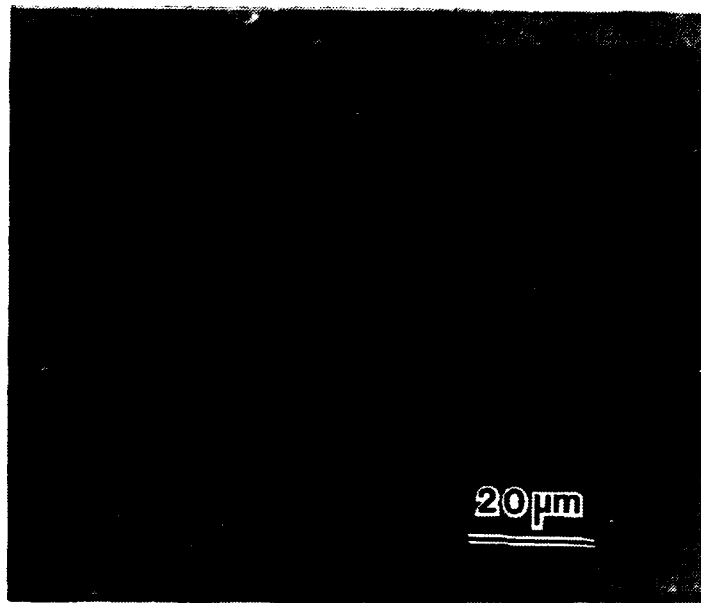


Figure 19. A Large Spinel Oxide Inclusion.

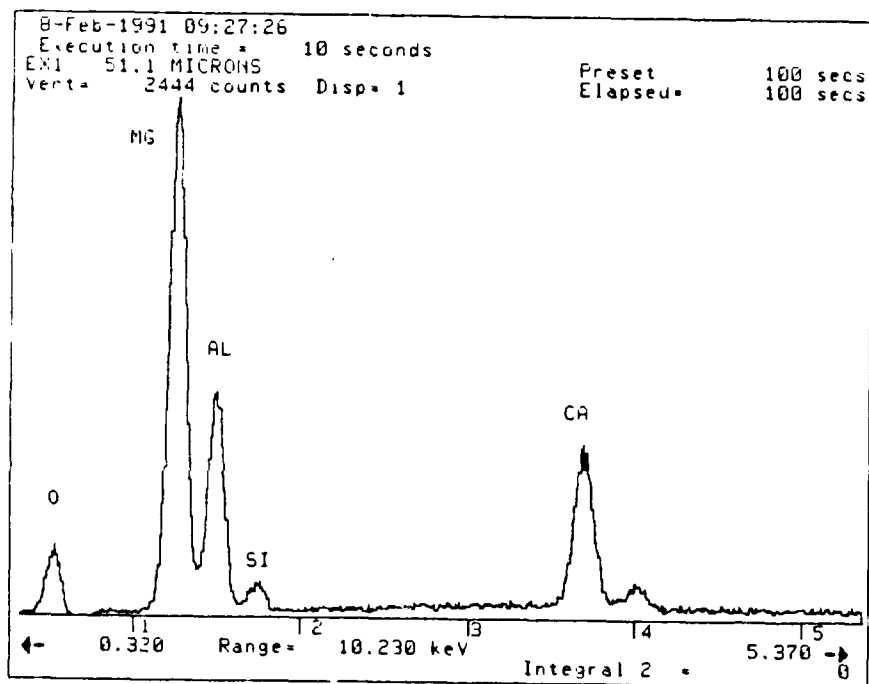
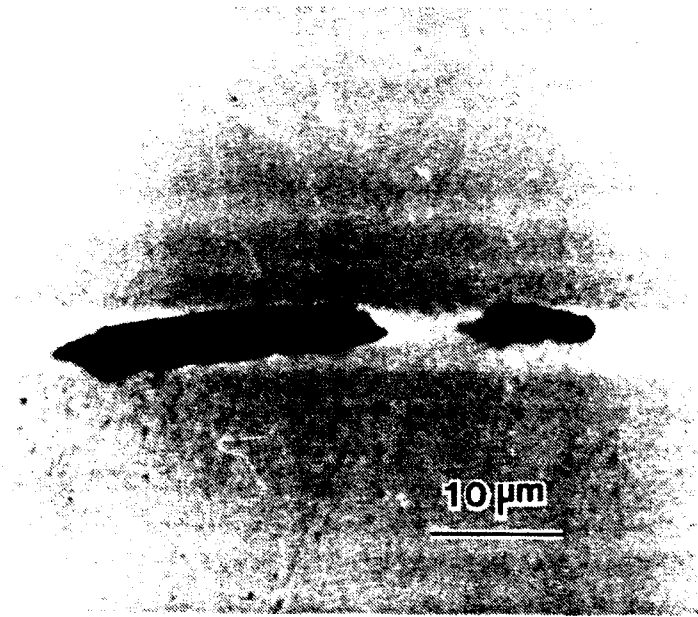


Figure 20. EDX Analysis of Spinel Oxide Inclusion.



Slightly elongated oxides were also discovered as shown in Figure 21. EDX analysis proved this 23  $\mu\text{m}$  inclusion to be a corundum ( $\text{CaO-SiO}_2\text{-Al}_2\text{O}_3$ ), also from an exogenous source. Corundums are brittle due to their higher aluminum content and tend to break up during deformation. As expected of aluminum-killed and calcium treated steels, numerous  $\text{CaO-Al}_2\text{O}_3$  and  $\text{CaO-2Al}_2\text{O}_3$  inclusions were observed. No harmful  $\text{Al}_2\text{O}_3$  clod inclusions were found.



**Figure 21. Elongated Corundum Oxide Inclusion.**

A total of 30 oxysulfide inclusions, with a mean diameter of 4.28  $\mu\text{m}$ , were found in the statistical study. Figure 22 displays their size distribution. A group of 3 oxysulfides are shown in Figure 23, with the accompanying EDX spectra featured in Figure 24. The following atomic percent compositions were recorded: Mg (24.51%), Al

(43.72%), Si (19.04%), S (4.18%), and Ca (8.55%). The free energy of formation of the sulfides (Appendix A) shows that the Ca will readily react with the S. The Mg, Al, and Si all occur as oxides making it necessary to use the  $\text{MgO-Al}_2\text{O}_3\text{-SiO}_2$  ternary phase diagram to determine the phase present. The material was found to be spinel ( $4\text{MgO}\cdot 5\text{Al}_2\text{O}_3\cdot 2\text{SiO}_2$ ).

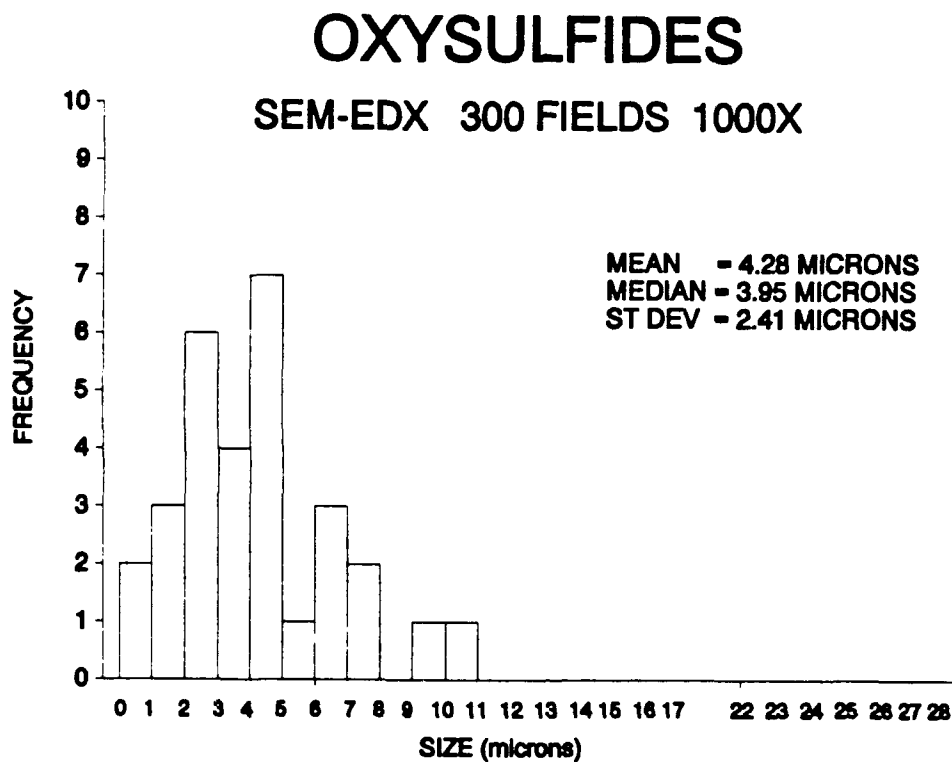
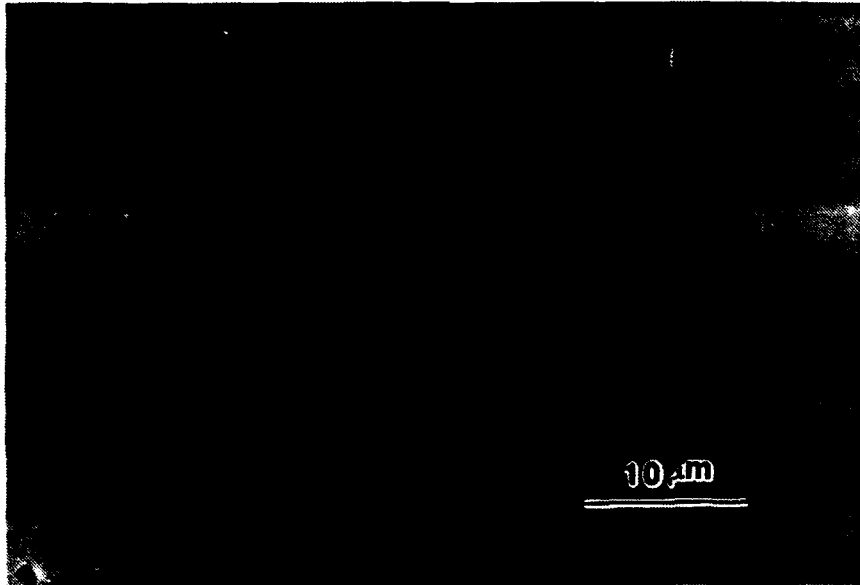
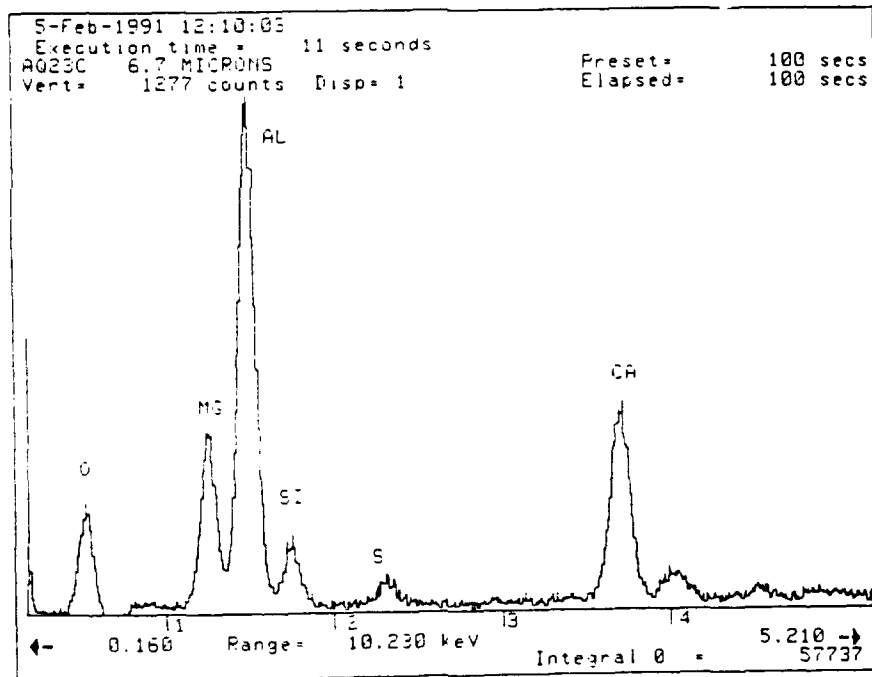


Figure 22. Distribution of Oxysulfide Inclusions.



**Figure 23. Oxysulfide Inclusions.**



**Figure 24. EDX Analysis of Oxysulfide Inclusion.**

The data indicates that the oxides were on average twice as large as the oxysulfides. Pure oxides with their high aluminum content tend to have higher melting points. They grow in the molten steel and form extensive 3-dimensional arrays. The oxysulfides, on the other hand, generally have a higher weight percent of CaO resulting in a higher capacity for sulfur. As shown in the CaO-Al<sub>2</sub>O<sub>3</sub> binary phase diagram in Appendix A, the more calcium present, the lower the melting point temperature of the CaO-nAl<sub>2</sub>O<sub>3</sub> inclusions that form. They coalesce and float out of the molten steel more easily than the aluminum oxides. The result is a smaller diameter for the higher CaO oxysulfides as compared to the higher Al<sub>2</sub>O<sub>3</sub> oxides. [Ref. 37:p. 420]

There were no pure sulfides found in the SEM study which is attributed to the desulfurizing action of the calcium treatment. It was also remarkable that no CaMnS inclusions were found; in fact, there was very little, if any, manganese detected in any of the inclusions which indicates the success of this aspect of the calcium treatment.

Both the optical and SEM/EDX inclusion studies showed that most of the second phase particles present were globular and small enough in diameter to prevent anisotropic properties in the steel. A few large inclusions and slightly deformed oxides were discovered, however, which could theoretically cause problems. The elongated oxides were not plastically deformed but were simply broken up in the rolling direction due to their brittleness. Unfortunately, the calcium treatment was not sufficient to transform every second phase particle to the strong and hard CA, CA<sub>2</sub>, or C<sub>12</sub>A<sub>7</sub>.

composition which are resistant to deformation. High amounts of sulfur may have been present during the treatment resulting in a partial conversion of alumina inclusions to molten calcium aluminate inclusions. The brittle  $\text{CaO-6Al}_2\text{O}_3$  solid aluminates may have been coated with a thin layer of CaS-saturated molten aluminate which prevented their conversion to molten oxides. [Ref. 34:p. 5]

Lukens Steel Company has been notified of the presence of these larger oxides by DTRC and is currently working on reducing their size through improved calcium treatment.

## **B. MECHANICAL BEHAVIOR**

The variation of HSLA-100's yield strength and toughness with aging temperature is shown in Figure 25, while the relationship between ultimate tensile strength and aging temperature is shown in Figure 26. The strength peaks at 454°C and then decreases at higher aging temperatures. At 677°C, the strength has actually fallen below the as-quenched condition. This rise and fall in strength is characteristic of aging behavior associated with copper precipitation. The toughness values shown in Figure 25 were measured by conducting Charpy V-notch (CVN) impact tests on specimens cooled to -84°C. The plot shows the toughness decreasing until a minimum is reached at the peak age temperature of 454°C. As the steel is overaged, though, the toughness dramatically rises. At an aging temperature of 621°C, the impact energy exceeds the as-quenched steel by a factor of two. Figure 27 shows the DBTT behavior of HSLA-100 steel at various

aging temperatures. Again the impact energy decreases to a minimum at the 454°C aging temperature and then returns to approximately the same impact behavior at 566°C as it had in the as-quenched condition. Above 566°C, the DBTT is shown to decrease while the impact energy increases at all testing temperatures. The DBTT curves of 621°C and 677°C are almost identical.

Percent reduction of area and percent elongation are two parameters used to measure the ductility of a steel. These characteristics as a function of aging temperature are plotted in Figure 28. The reduction of area measurement remains fairly constant during aging; the 677°C aged specimen recorded a 73% reduction which was only 5% larger than the as-quenched condition. The elongation was shown to increase gradually from 23% to 42%.

The above mechanical testing results on lot GQH exceed the strength, toughness, and ductility requirements for HSLA-100 steel listed in Table III, with the exception of the 677°C aged steel which does not meet the minimum yield strength and the 399, 454, and 521°C aged steels which do not meet the minimum toughness requirements.

**TABLE III. HSLA-100 STEEL STRENGTH  
AND TOUGHNESS REQUIREMENTS**

0.2% Yield Strength	690 MPa minimum
Elongation	18% minimum in 50.8 mm
Reduction of Area	45% minimum
Transverse Charpy V-notch Impact Toughness	81.3 J at -19° 54.2 J at -84°C

The mechanical property data provided by DTRC shows that the best combination of strength and toughness occurs at the overaged temperature of 621°C; the microstructure of this optimum specimen will therefore be examined in the current work. The as-quenched, peak aged, and 677°C overaged microstructures, initially examined by Mattes, will also be reviewed in this thesis.

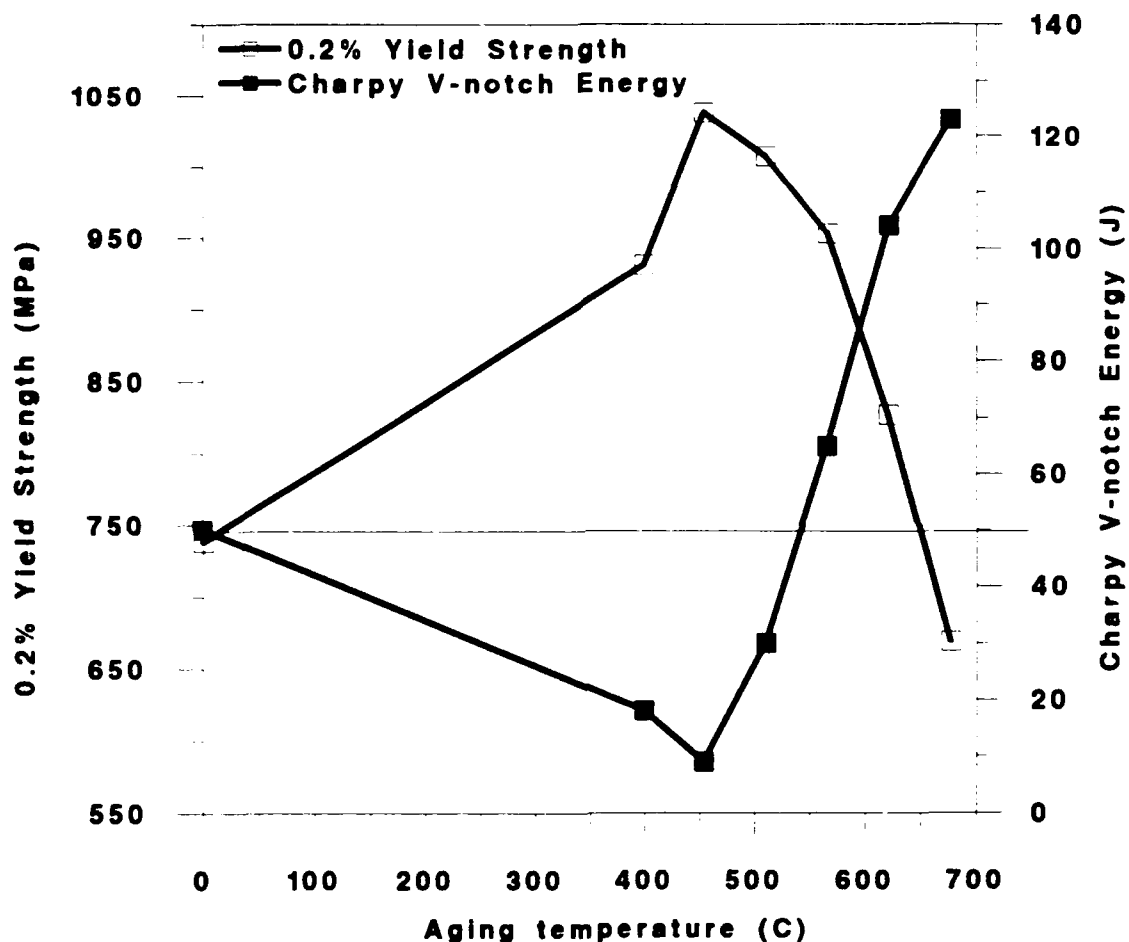


Figure 25. HSLA-100 Steel Lot GQH 0.2% Yield Strength and Impact Energy at -84° C as a Function of Aging Temperature.

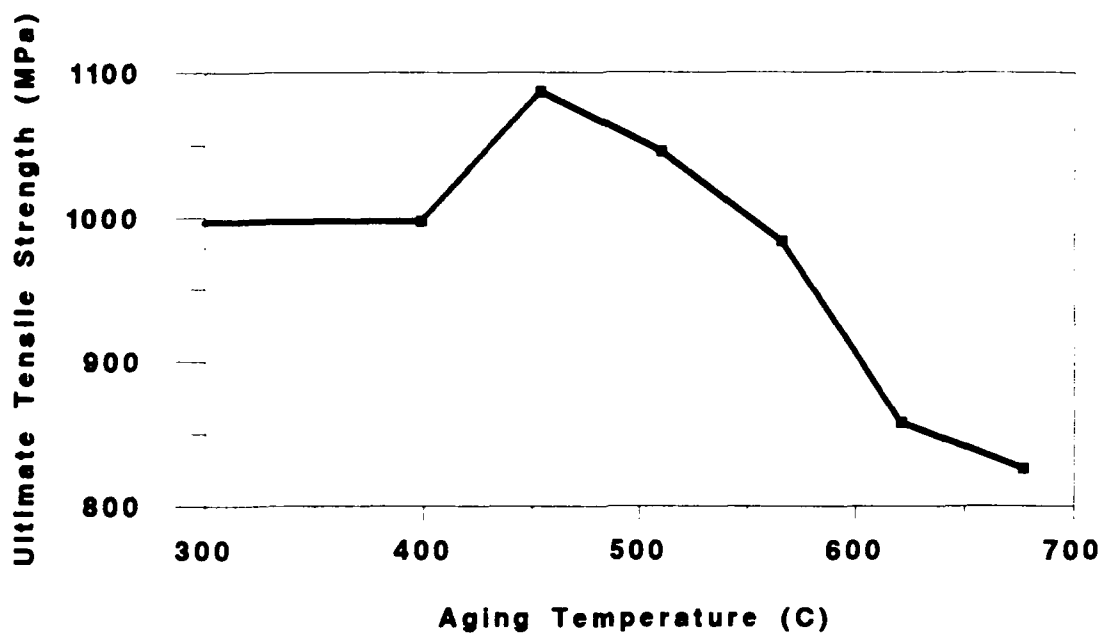


Figure 26. HSLA-100 Steel Lot GQH Tensile Strength

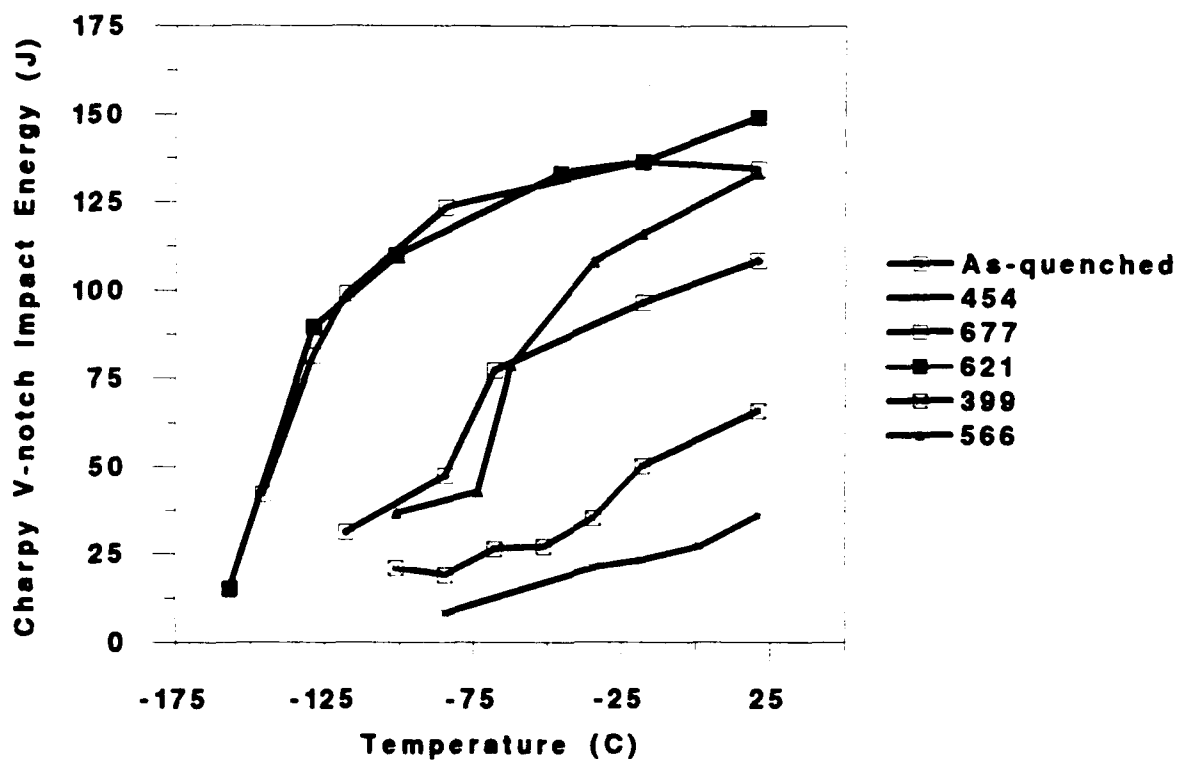


Figure 27. HSLA-100 Steel Lot GQH DBTT Behavior for Various Aging Temperatures.



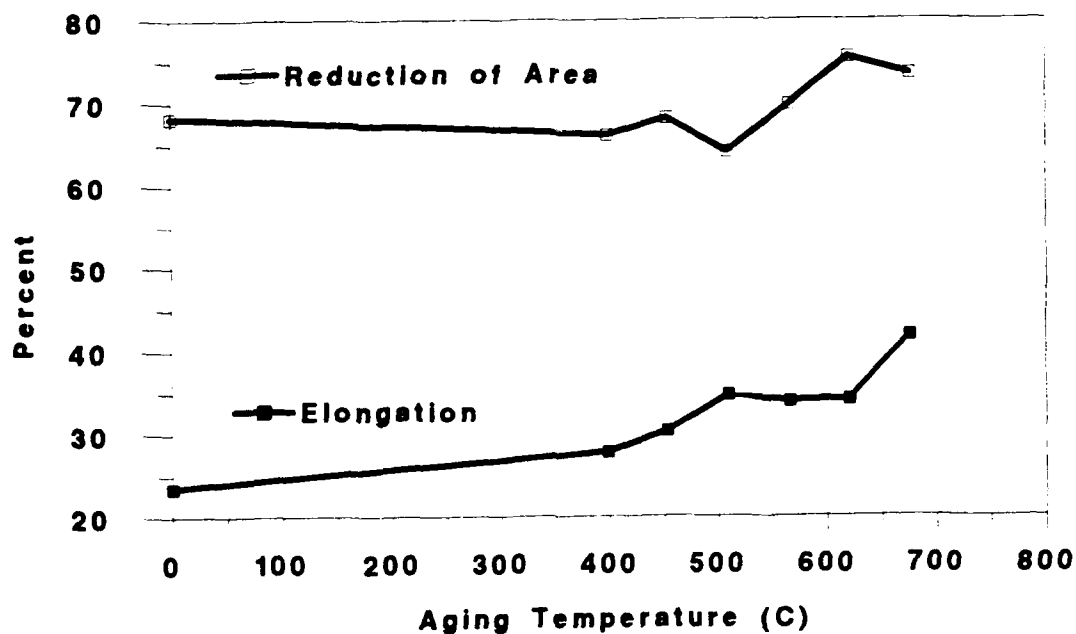


Figure 28. HSLA-100 Steel Lot GQH Ductility: Variation of Elongation and Reduction of Area With Aging Temperature.

## C. MICROSTRUCTURE

### 1. As-quenched HSLA-100 Steel

An SEM micrograph of the as-quenched HSLA-100 steel is shown in Figure 29 where the transformation product packet boundaries are visible. The transformation product is lath martensite/retained austenite + acicular ferrite (bainite). This microstructure is expected from an examination of the HSLA-100 steel CCT diagram (Figure 1), although for a 31.75 mm plate we would expect the martensite/acicular ferrite ratio to decrease going from the surface to the center of the plate. Figure 30 is a TEM micrograph

illustrating thin lath martensite (0.1  $\mu\text{m}$ ) interspersed between larger bainite laths (0.3  $\mu\text{m}$ ). The high dislocation density is clearly visible. Twin martensite was also observed in the as-quenched specimen, as shown in Figure 31. Retained austenite is observed in the dark field micrograph (Figure 32). Copper precipitates were not evident since the selected area diffraction patterns were clear of streaking. Howell found copper precipitates in his research, but his as-quenched specimens were oil quenched, allowing a slower cooling rate [Ref. 38:p. 902]. Precipitated carbides or carbonitrides also were apparently not present. The transformation product packet size, consisting of bainite and martensite, was found to be about 7  $\mu\text{m}$ .

The main strengthening mechanisms for the as-quenched condition appear to be the fine prior austenite grain size leading to a small transformation product packet size and the highly dislocated bainite/martensite substructures, both of which impede dislocation motion. Interstitial carbon, molybdenum, copper, chromium, and nickel provide some solid solution strengthening. The toughness is due to the small transformation product packet size and the fine bainite/martensite laths which tend to deflect dislocations and cracks.

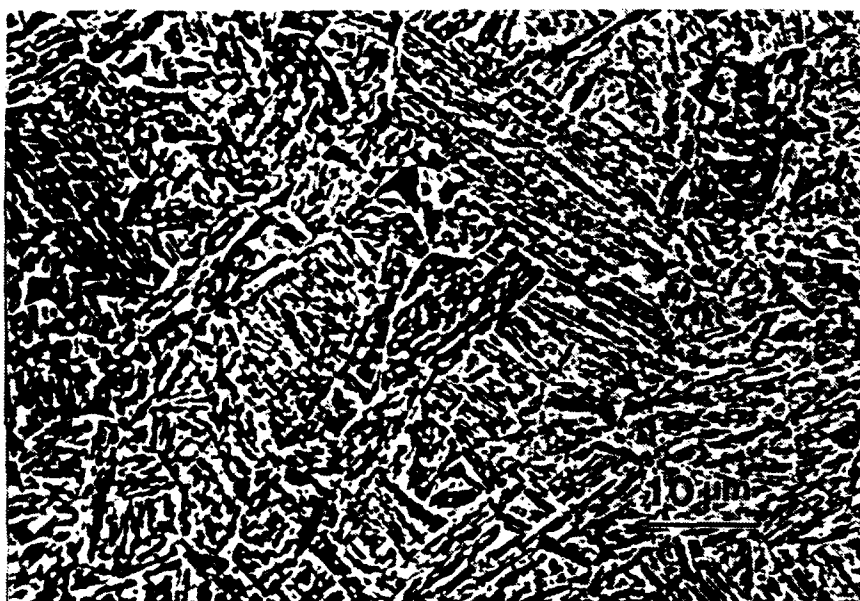


**Figure 29. SEM Micrograph of As-quenched Transformation Product Packets.**



**Figure 30. TEM Image Showing Acicular Ferrite (Bainite), Lath Martensite, and Retained Austenite in As-quenched Sample.**

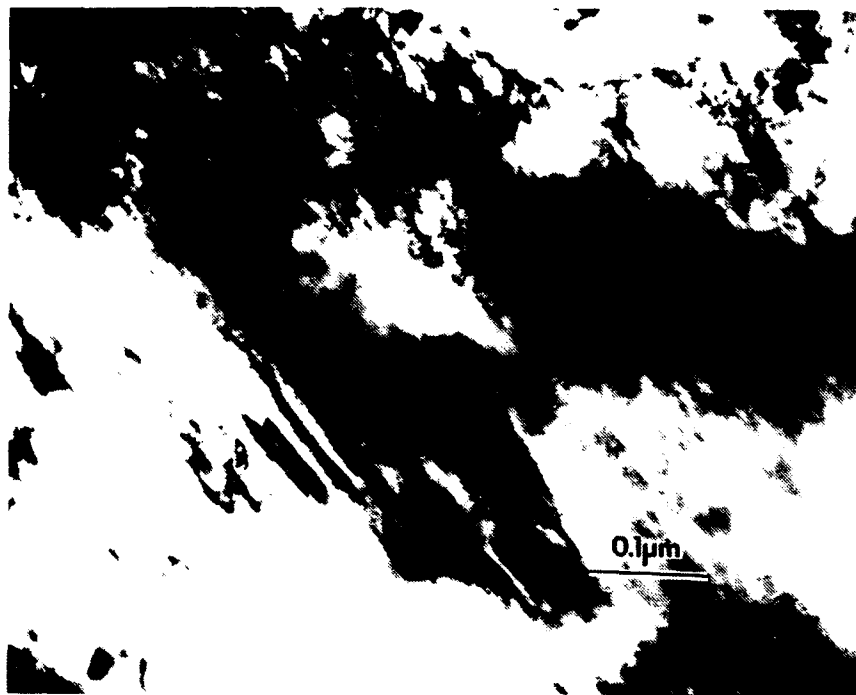


**Figure 31. TEM Image of Twin Martensite in As-Quenched Sample.**



**Figure 32. TEM Dark Field Image of Retained Austenite at Lath Boundaries of Martensite in As-quenched Sample. Imaged Using  $\bar{g}=111$  of Austenite.**

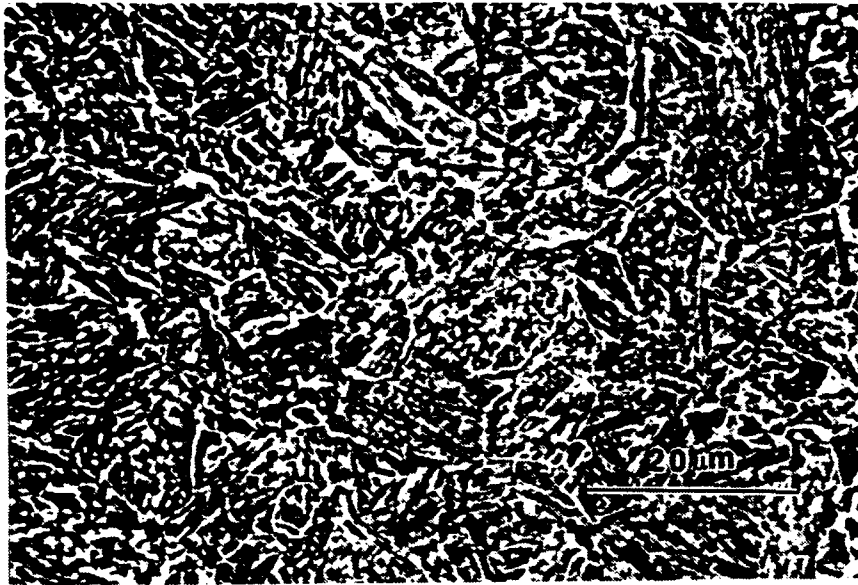


**Figure 33. SEM Micrograph of 454°C Aged Transformation Product Packets.**

## **2. 454°C Aged HSLA-100 Steel**

A back-scattered SEM image of the peak aged HSLA-100 steel microstructure is shown in Figure 33. The transformation product packets are approximately 8.1  $\mu\text{m}$  in diameter, slightly larger than the as-quenched condition. These packets are composed of tempered lath martensite/acicular ferrite (bainite) (Figure 34). Although the coherent copper precipitates are not visible due to their small size ( $\sim 20$  Å), their presence is evident as there is streaking in the SADPs [Ref. 13:p. 40]. Coherent strain fields are also visible in bainite laths; an example is shown in Figure 35. Intralath carbides and carbonitrides on the order of 600 Å have precipitated as shown in Figure 36. EDX

analysis provided in Figure 37 identified niobium and sometimes molybdenum in their composition.

Peak strength is attained in the 454°C aged specimen. Although the transformation product packet size is an important contributor to strength, significant additional strengthening is provided by classic copper age hardening. Small coherent BCC copper particles have precipitated. Previous work suggests that their size is about 24 Å [Ref. 30]. Their coherency causes large elastic strain fields to be produced; dislocations are blocked by these strain fields causing an increase in the stress required for dislocation motion. Dislocation substructures and carbide precipitates are also contributing to the increased strength.

Toughness reaches a minimum at this aging temperature since the dislocations are impeded by the mechanisms listed above. Again, this mechanical behavior is characteristic of peak aged coherent precipitate hardened copper bearing steels.

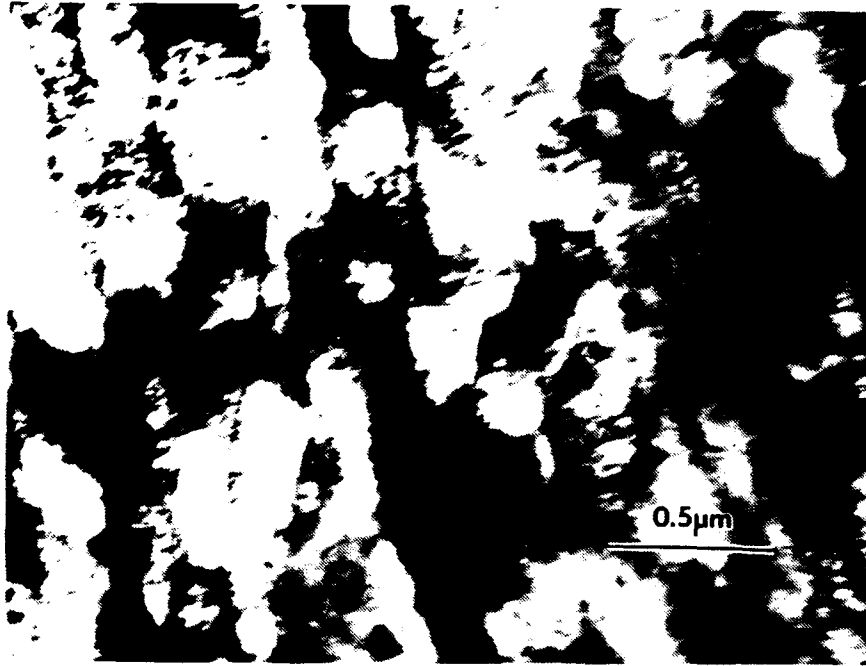


**Figure 34. TEM Image Showing 454°C Aged HSLA-100 Steel Lath Structure.**

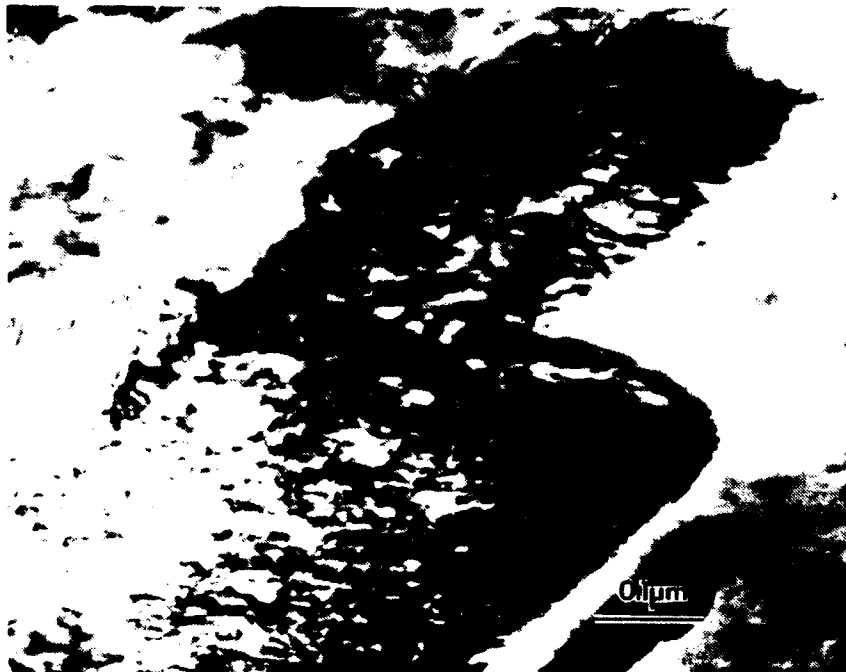


**Figure 35. TEM Image of 454°C Aged HSLA-100 Steel Copper Coherent Strain Fields in Bainite Lath.**

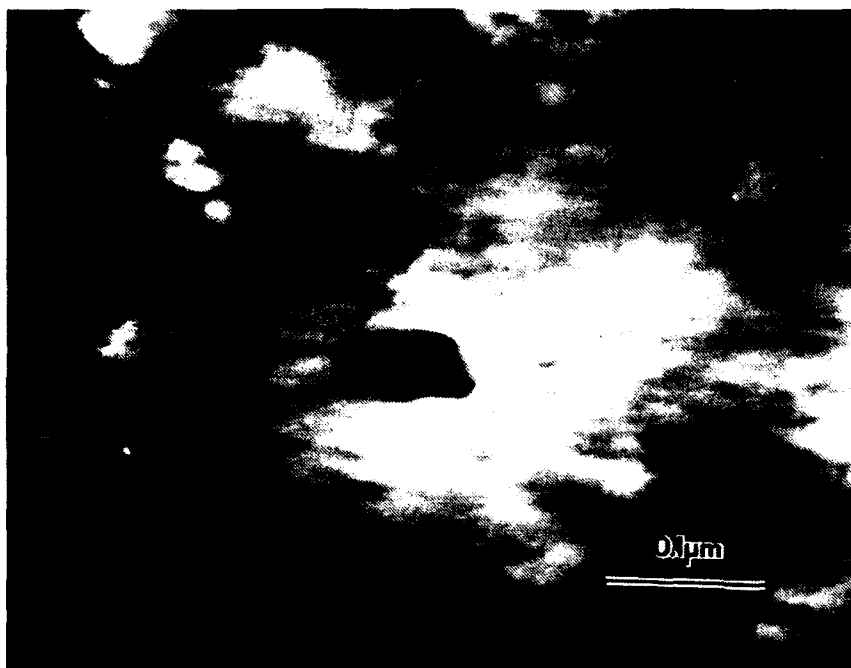


Figure 36. TEM Image of 454°C Aged HSLA-100 Steel Intralath Carbide

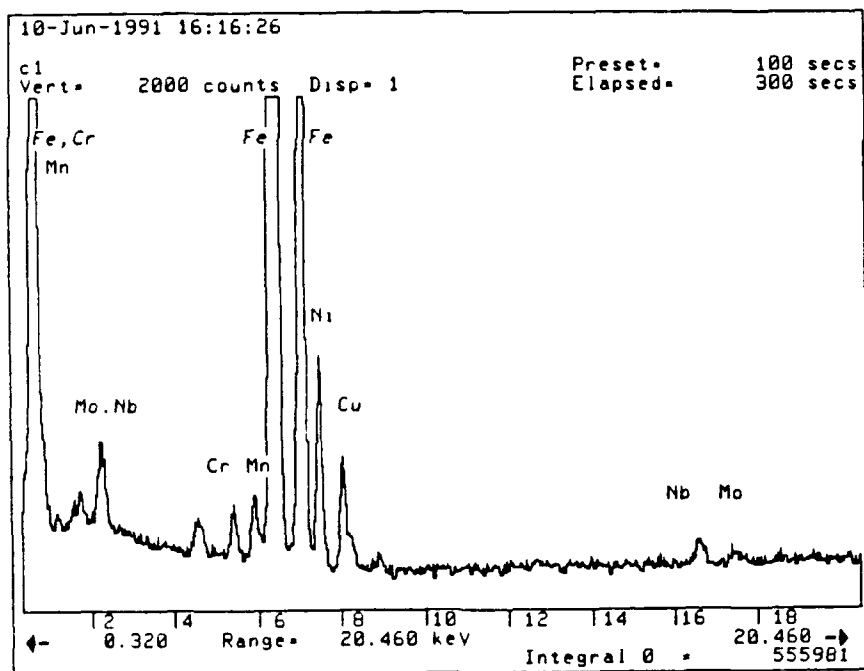


Figure 37. EDX Spectra of 454°C Aged HSLA-100 Steel Carbide.



### 3. 621°C Aged HSLA-100 Steel

Light and SEM micrographs showing the microstructure of this overaged specimen are featured in Figure 38. The transformation product packet size has increased to a diameter of  $\sim 9.7 \mu\text{m}$  and the tempered bainite/martensite laths have widened to  $\sim 0.26 \mu\text{m}$  (Figure 39). Copper precipitates are now clearly visible and are seen in Figure 40 decorating dislocations and lath boundaries. Bright and dark field micrographs (Figure 41) show that the majority of the copper precipitates are spherical, measuring 50-100 Å in diameter. It would seem that most of the copper precipitates have transformed from coherent BCC to incoherent FCC structures; in support of this, the SADPs showed a much reduced level of streaking. Niobium and molybdenum containing tempered carbides are visible in the lath field and at lath boundaries (Figures 42-45).

The strength at this aging temperature is lower than that of the peak aged condition. This is typical of age hardened materials and is due to the growth of the copper precipitates and their resulting incoherence with the steel matrix. Dislocations are now less likely to be impeded due to the larger effective interparticle spacing; the strength is reduced. Secondly, the dislocation substructures are recovered and their effect on strength is less pronounced. Finally, the increase in the transformation product packet size probably has a negative effect on strength. The tempered niobium and molybdenum carbides, however, have a positive influence on strength since they force the dislocations

to expend energy by bowing around them. The strength level achieved in this 621°C aged microstructure is still an improvement over the original as-quenched value.

The toughness dramatically increases at this aging treatment, practically doubling in value from the as-quenched condition. The ductile overaged copper precipitates almost certainly play the largest role in this phenomenon; they can plastically deform and blunt propagating crack tips. The hard intralath carbides may also contribute by deflecting cracks. The dislocation substructures also continue to recover making dislocation motion more possible. In addition, the retained austenite present in the as-quenched sample could contribute to poor toughness since this could transform to martensite during deformation.



**Figure 38. Micrographs of 621°C Aged HSLA-100 Steel Transformation Product Packages: (Top) Light Micrograph, (Bottom) SEM Micrograph**

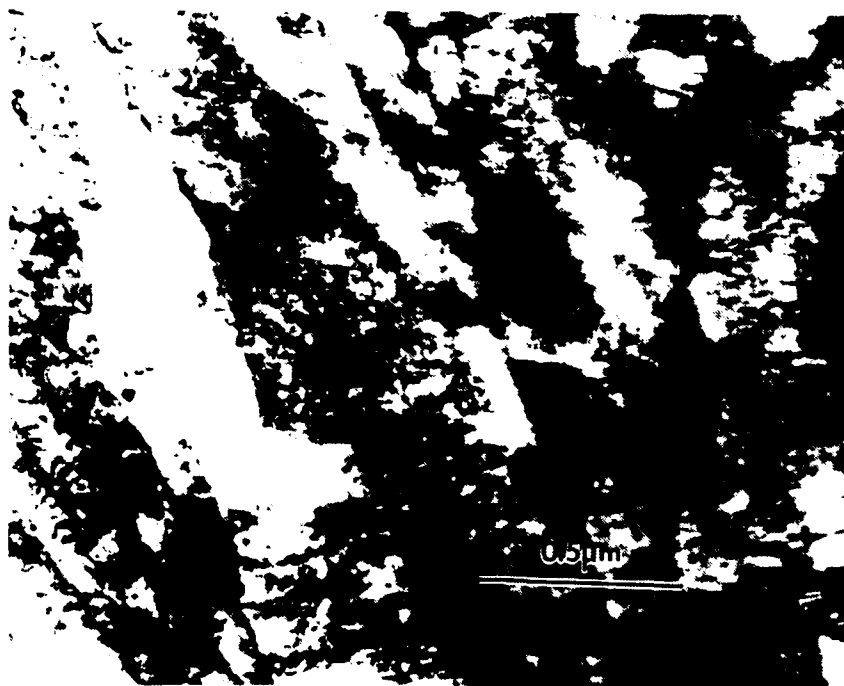


**Figure 39.** TEM Image of 621°C Aged HSLA-100 Steel Lath Structure

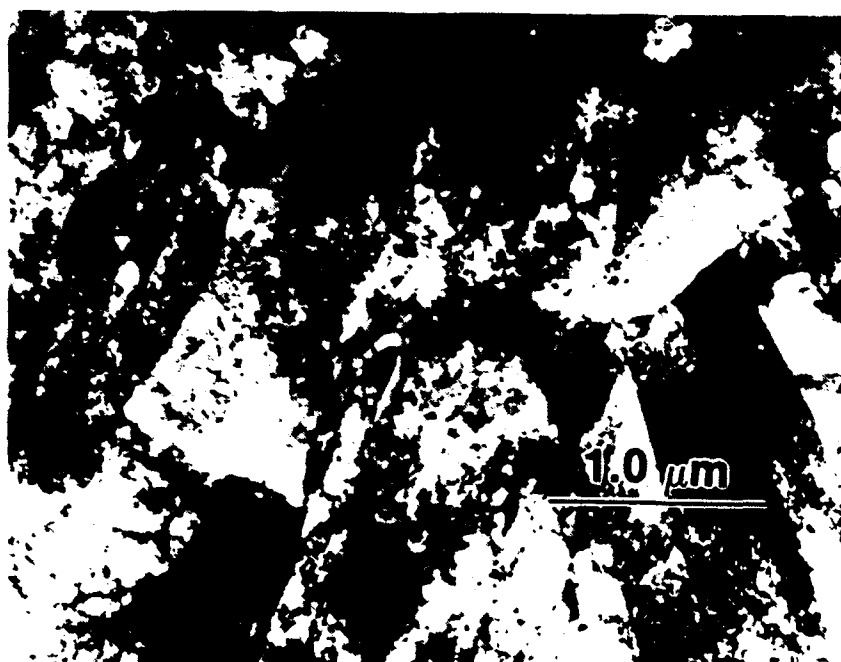


**Figure 40.** TEM Image Showing Copper Precipitates Decorating Dislocations and Lath Boundaries in 621°C Aged HSLA-100 Steel.

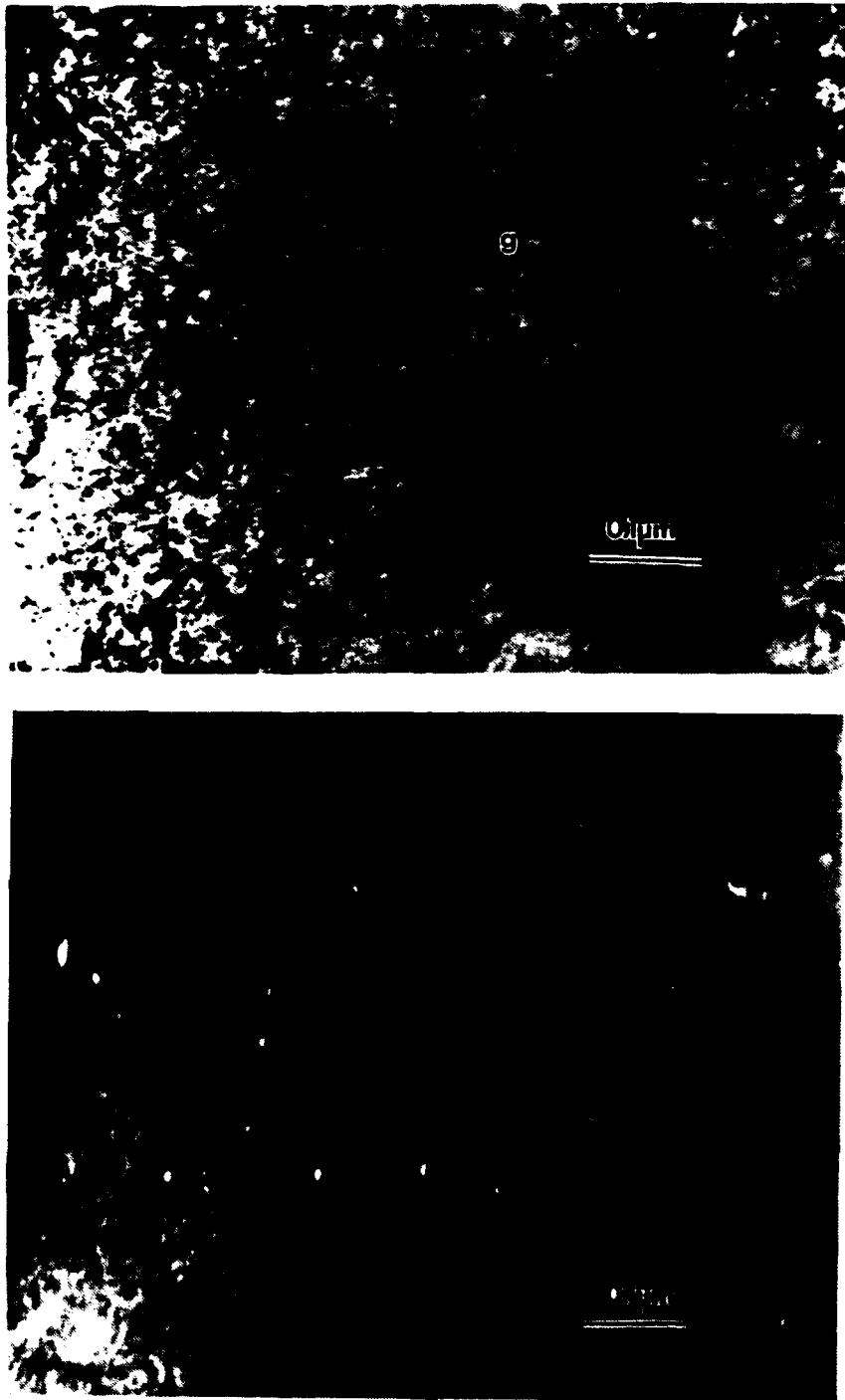


**Figure 41.** TEM Image of Copper Precipitates in 621°C Aged HSLA-100 Steel: (Top) Bright Field,  $\bar{B}$  Close to  $\langle \bar{1}13 \rangle$   $\bar{g}=\bar{1}10$ ; (Bottom) Dark Field.

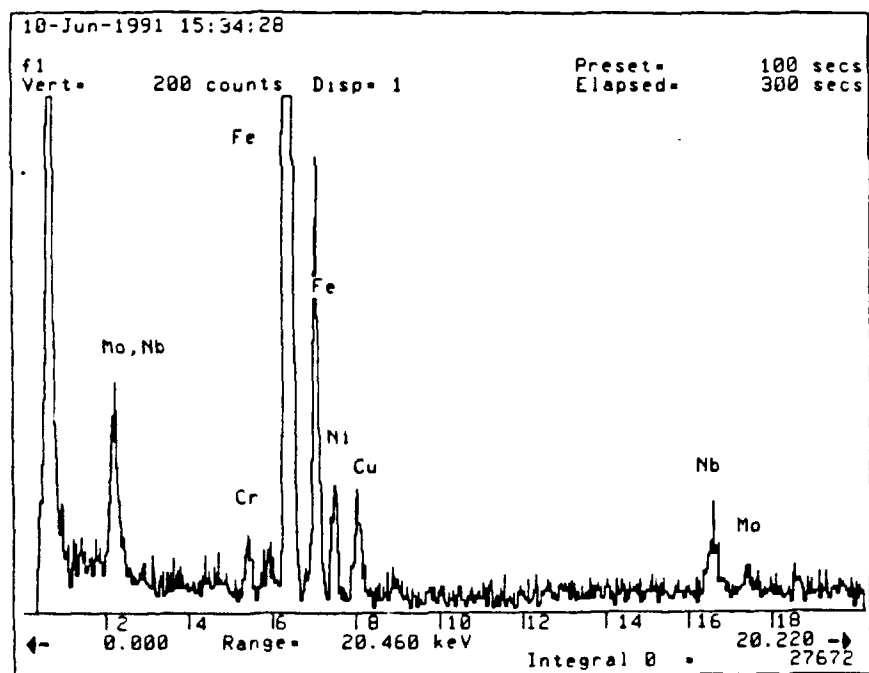


**Figure 42.** Intralath Nb-Mo Carbide (500 Å) in 621°C Aged HSLA-100 Steel:  
(Top) TEM Image; (Bottom) EDX Spectra.



**Figure 43.** TEM Image of Nb-Mo Carbide (350 Å) at Triple Junction in 621°C Aged HSLA-100 Steel.

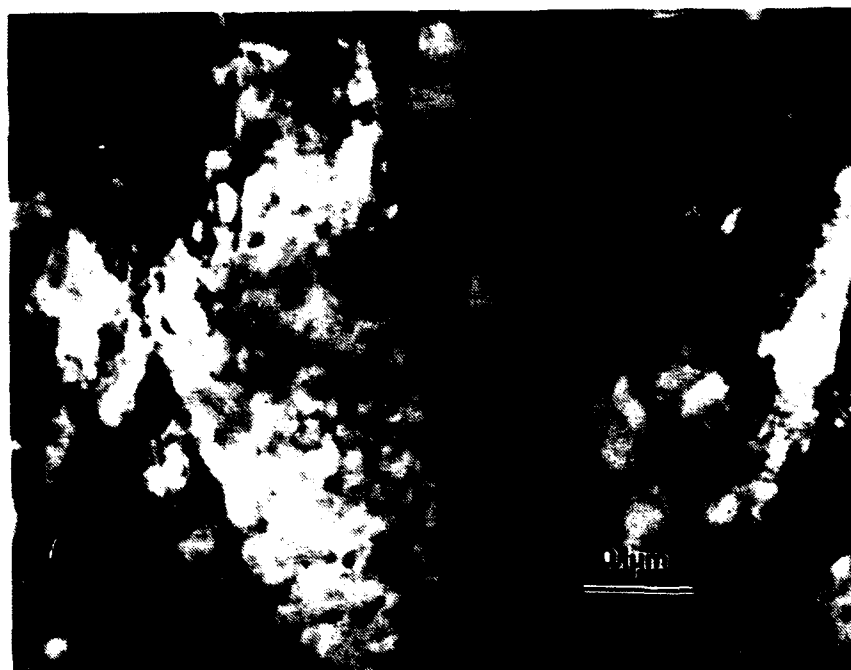


**Figure 44.** TEM Image of Interlath 621°C Aged HSLA-100 Steel Molybdenum Carbide (1000 Å)

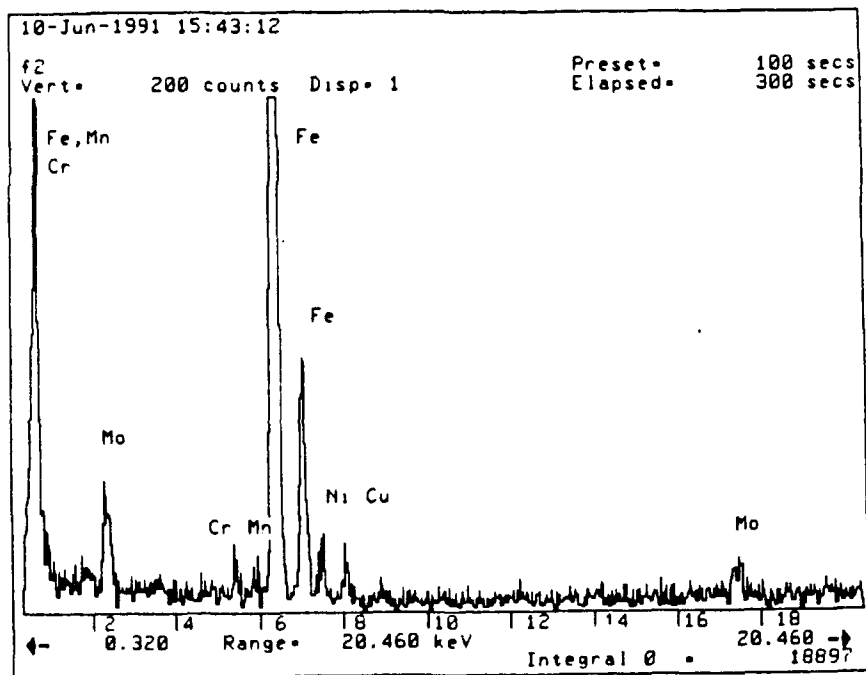
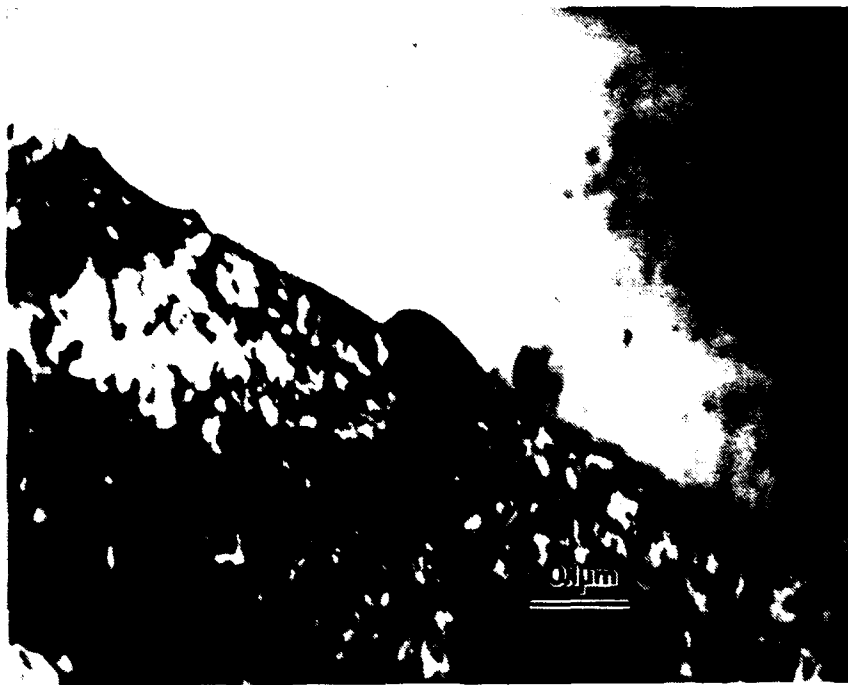


**Figure 45.** Interlath Molybdenum Carbide ( $1000 \text{ \AA}$ ) in  $621^\circ\text{C}$  Aged HSLA-100 Steel: (Top) TEM Micrograph; (Bottom) EDX Spectra.



#### 4. 677°C Aged HSLA-100 Steel

A light micrograph of the 677°C aged steel is shown in Figure 46. The transformation product packets have grown to a size of  $\sim 10.2\text{ }\mu\text{m}$ . Figure 47 is a TEM image of the tempered bainite/martensite laths which have widened to an average width of  $\sim 0.27\text{ }\mu\text{m}$ . The incoherent copper precipitates have continued to grow, now ranging in size between 200-500 Å, with some appearing rod-like in shape (Figures 48 and 49). Nb-Mo carbides ( $\sim 400\text{ Å}$ ) were observed in the laths (Figure 49) while molybdenum carbides ( $\sim 500\text{ Å}$ ) were found at the lath boundaries (Figure 50). Polygonal ferrite has also apparently formed which is expected since 675°C is approximately the lower critical temperature for this steel.

The strength decreases to a value of 669 MPa at this aging temperature which is below the required 690 MPa 0.2% yield strength. The formation of polygonal ferrite has resulted in the recrystallization of regions of high dislocation density. Recovery of the dislocations that do not recrystallize results in dislocation free bainitic ferrite laths, thus lowering the strength [Ref. 13:p. 63]. The much larger overaged copper precipitates also degrade the strength. These particles are now 200-500 Å in diameter with large distances between them; their interface with the matrix has little or no effect on the motion of dislocations. The tempered carbides are, however, a positive influence on strength since they force the dislocations to bow around them.

The toughness reaches its highest value at this aging temperature. The large ductile copper precipitates can apparently plastically deform to blunt the crack tip of propagating cracks. The hard intralath carbides improve fracture toughness by acting as crack arresters; the high angle boundaries of the polygonal ferrite also impede cracks. Finally, the markedly lower dislocation density throughout the microstructure will obviously lead to low strength and high toughness.

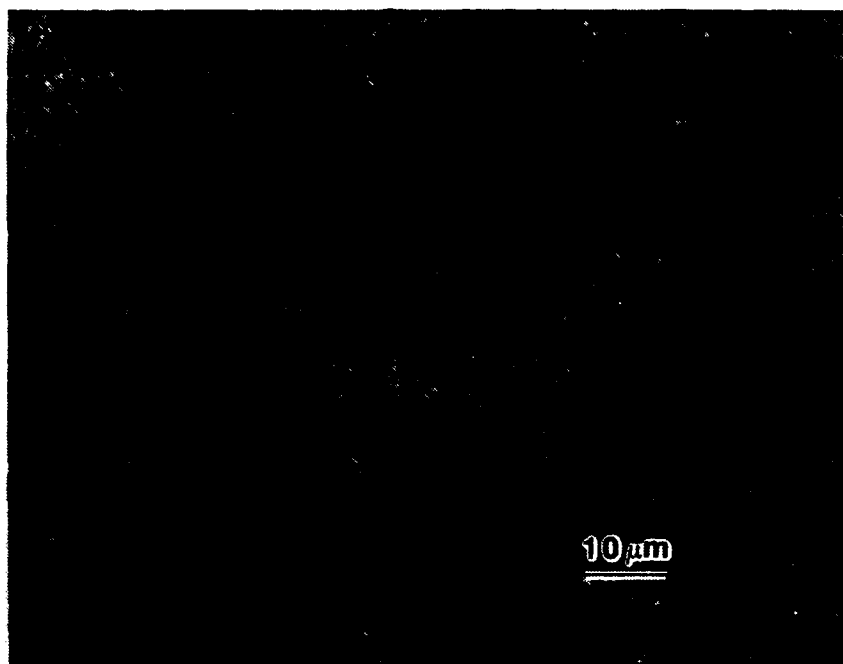


Figure 46. Light Micrograph of 677°C Aged HSLA-100 Steel Transformation Product Packets.

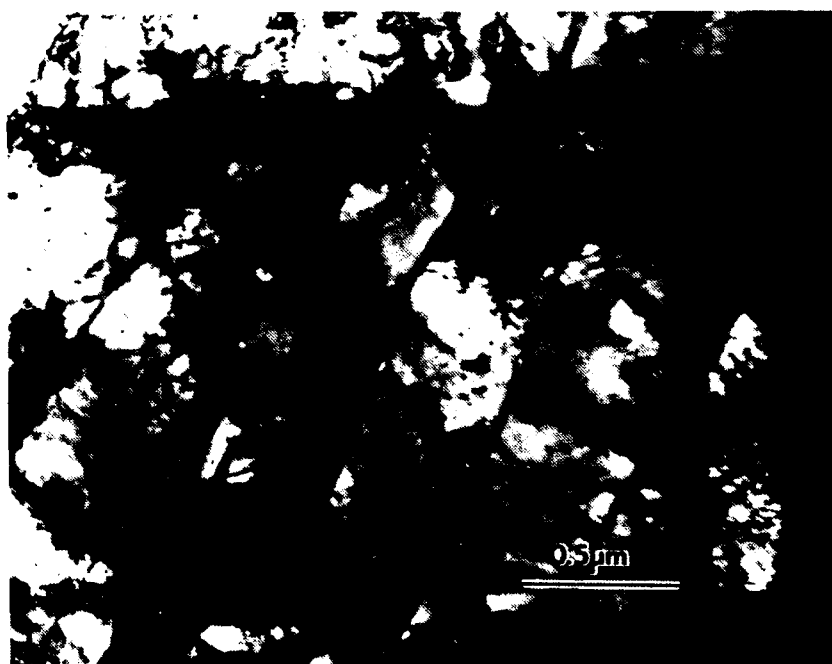


Figure 47. TEM Image of 677°C Aged HSLA-100 Steel Lath Structure.



Figure 48. TEM Image of Intralath Copper Precipitates and Interlath Carbides in 677°C Aged HSLA-100 Steel Lath Structure.

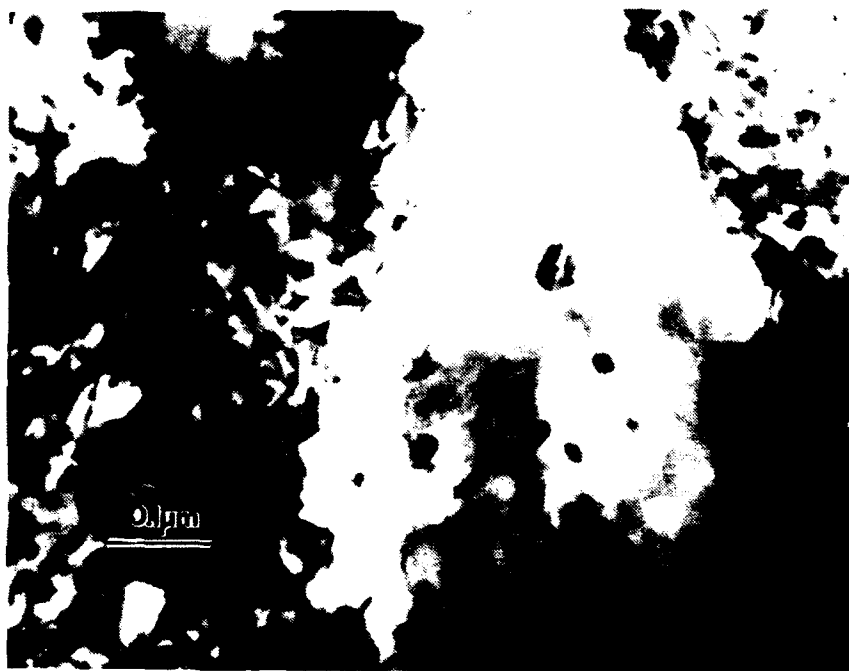
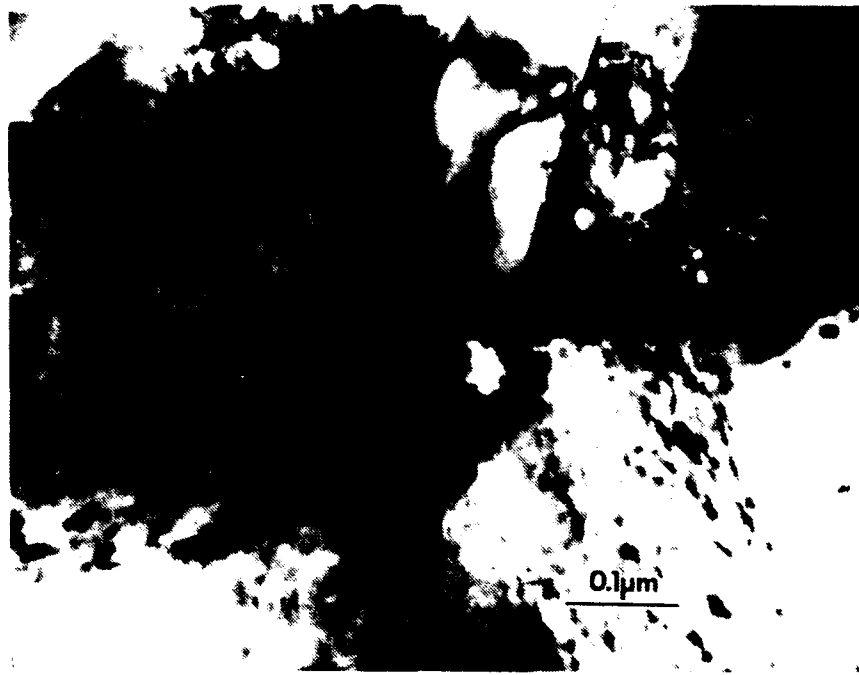


Figure 49. TEM Image of Intralath Carbides and Copper Precipitates.



**Figure 50.** TEM Image of Interlath Molybdenum Carbide in 677°C Aged HSLA-100 Steel.

### **5. Transformation Product Packet Dimensions**

Figure 51 shows the growth of the transformation product packet size as a function of aging temperature, while Figure 52 illustrates the growth of the bainite/martensite lath widths as a function of aging temperature. Both parameters experience slow growth up to the peak age temperature, 454°C, and then grow rapidly, reaching their largest size at the overaged temperature of 677°C. These results are consistent with Mattes' previous findings.

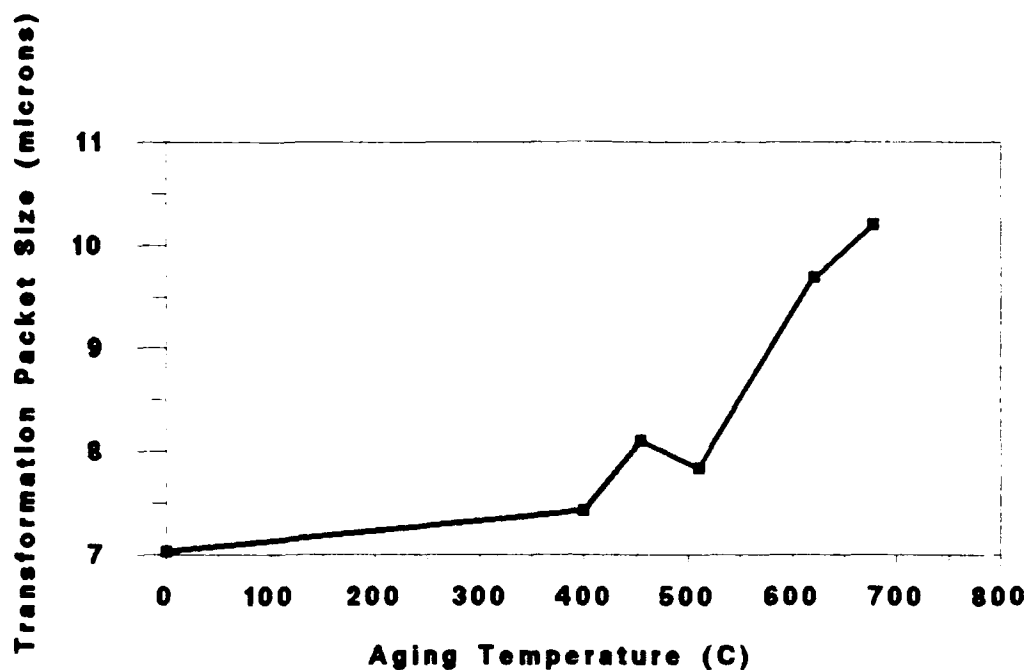


Figure 51. Variation of Transformation Product Packet Size With Aging Temperature.

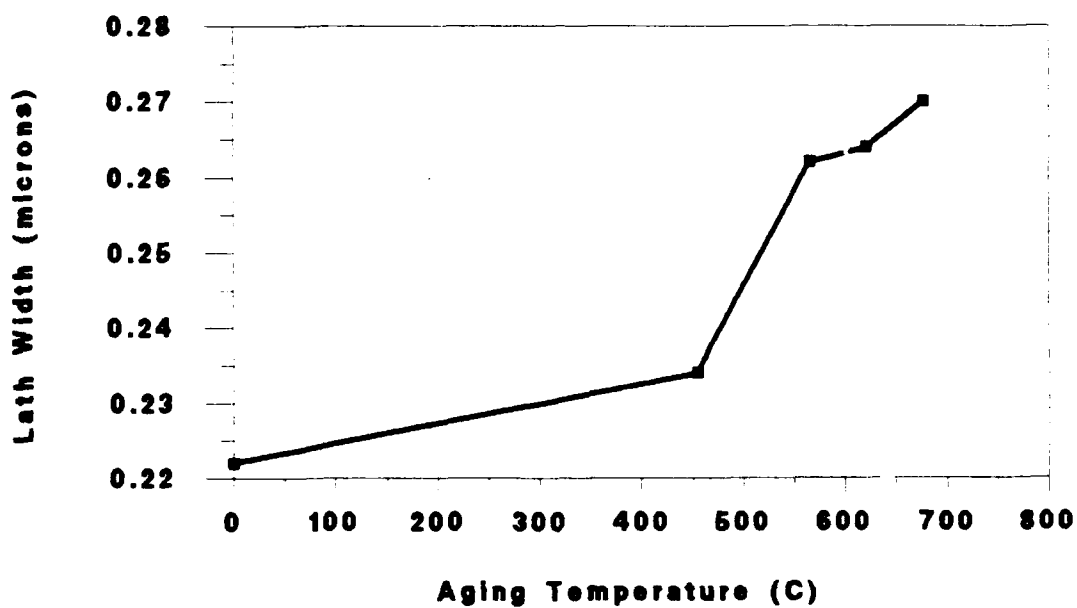


Figure 52. Variation of Bainite/Martensite Lath Widths with Aging Temperature.

## **V. SUMMARY**

### **A. CONCLUSIONS**

#### **1. Inclusion Study**

The results of the optical and SEM/EDX study showed the inclusion population in this lot of HSLA-100 steel generally consisted of small, globular, homogeneously dispersed particles. However, exogenous oxides of the order of 50  $\mu\text{m}$  were occasionally found as well as slightly elongated brittle oxides which had broken up in the rolling direction. The presence of these particular second phase particles could have deleterious effects on the mechanical properties of this steel. Improved calcium treatment could probably remove these undesirable inclusions. Fortunately, no harmful manganese sulfides were observed.

#### **2. Mechanical Properties**

Lot GQH meets the minimum requirements for strength, ductility, and toughness with the exception of the steel aged at 677°C which does not meet the minimum 690 MPa 0.2% yield strength, and the 399, 454, and 521°C aged specimens which failed to meet the minimum toughness requirement.

Of the seven specimens provided by DTRC, the aging treatment of 621°C offered the best combination of strength and toughness.

### 3. Microstructure

HSLA-100 steel's excellent strength and toughness are the result of several complex microstructural mechanisms. The microstructure of the as-quenched, peak aged (454°C), and overaged (621 and 677°C) specimens were studied in an effort to correlate these mechanisms with the observed mechanical properties of the steel.

The main strengthening mechanisms present in the base line as-quenched condition appear to be the small transformation product packet size and the highly dislocated bainite/martensite substructures. Solid solution strengthening also contributes to the impediment of dislocation motion. Toughness is influenced by the small transformation product packet size and the fine bainite/martensite laths which serve as crack and dislocation deflectors.

Peak strength is attained in the 454°C aged microstructure; the additional strengthening is primarily due to the precipitation of small coherent BCC copper particles which impede dislocation motion. Carbide precipitates also factor into the high strength by forcing dislocations to bow around them. The coherent copper has the opposite effect on toughness which is at a minimum at this aging temperature. The elastic strain fields do not allow adequate dislocation motion.

The best combination of strength and toughness occurs at the 621°C aged microstructure. Although the strength has decreased from the peak aged level due to the growth of incoherent copper precipitates and recovery of dislocation substructures, it is



still well above the required minimum 690 MPa. The toughness dramatically improves as a result of the ductile overaged copper precipitates and the intralath carbides which deter cracks. Recovery of the dislocation substructures also aid in making dislocation motion easier.

The 677°C aged microstructure possesses an unsatisfactory yield strength but extremely favorable fracture toughness. The overall low dislocation density and continued growth of large ductile copper precipitates account for the low strength and high toughness. The high angle polygonal ferrite boundaries and the intralath carbides both also contribute to the toughness by impeding crack propagation.

## **B. RECOMMENDATIONS**

The U.S. Navy's research and development program of HSLA-100 steels is continuing. It is the opinion of the author that future research in this area should include the following:

- An inclusion study on future lots of HSLA-100 steel manufactured by Lukens Steel Co. to determine if their calcium treatment has been improved to remove the large deleterious solid calcium aluminates found in the current work.
- Examination of a 590°C aged microstructure using optical and electron microscopy. Analysis of the data plotted in Figure 25 indicates that optimum strength and toughness may be achieved at an aging temperature different than the six temperatures evaluated by DTRC.
- The role precipitated carbides play in the strength and toughness mechanisms of HSLA-100 steel. A statistical analysis of the size, distribution, and chemical

composition of these particles may provide a better understanding of their effect on mechanical properties. [Ref. 13:p. 65]

- The development of an improved method for the thinning of TEM samples. A small size (25  $\mu\text{m}$ ) is required to avoid the magnetic distortion problems with these steel samples in the transmission electron microscope. The laborious mechanical and electrochemical thinning method currently used to attain this dimension continues to be a difficult if not impossible task. An improved method would save time and allow better crystallographic analysis to be conducted. [Ref. 13:p. 65]

# **APPENDIX A**

## **EQUILIBRIUM PHASE DIAGRAMS**

Free energy and equilibrium phase diagrams used in this study are included in this Appendix.

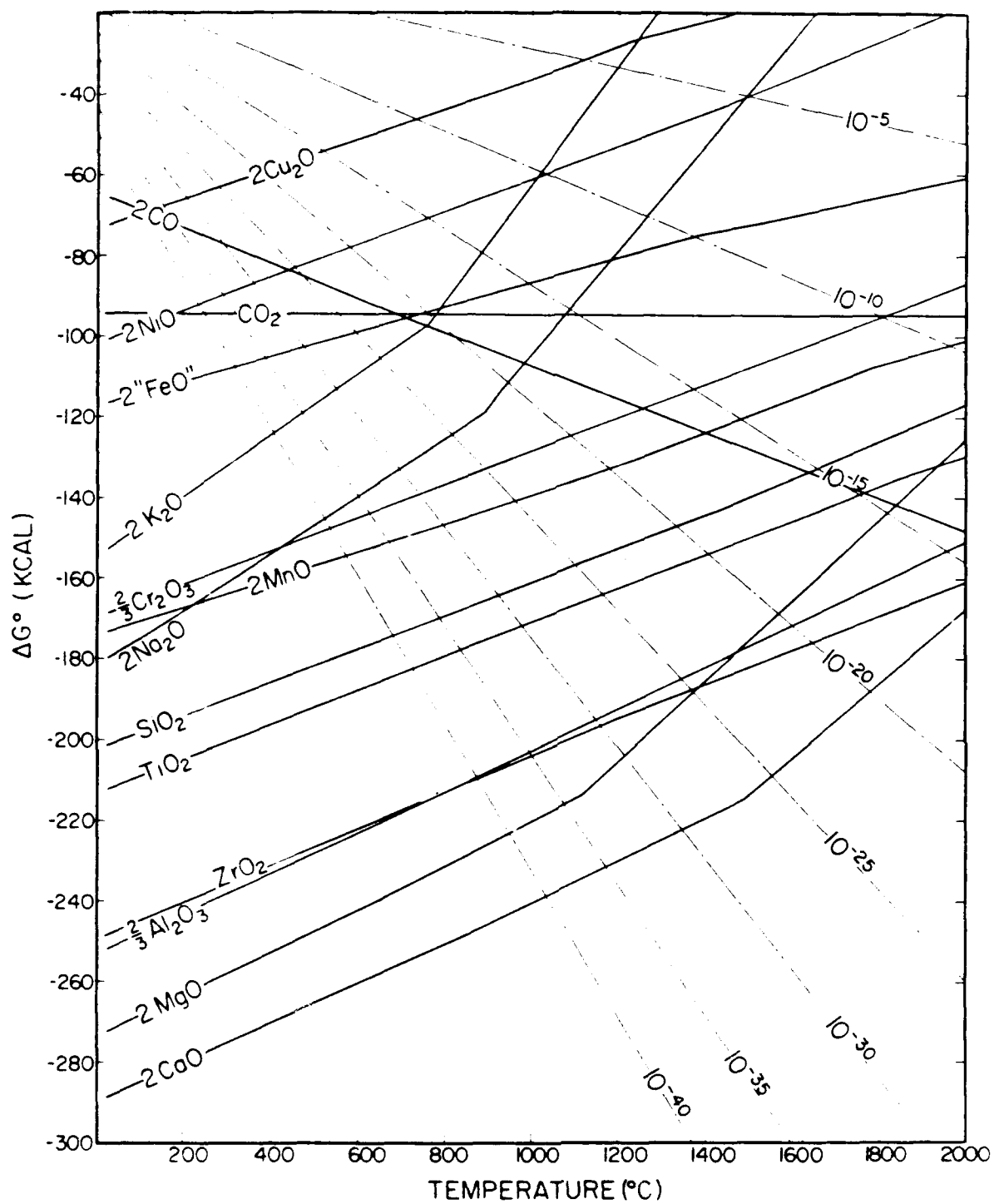


Figure A.1. Free Energy of Formation of Oxides [Ref. 39:p. 4].

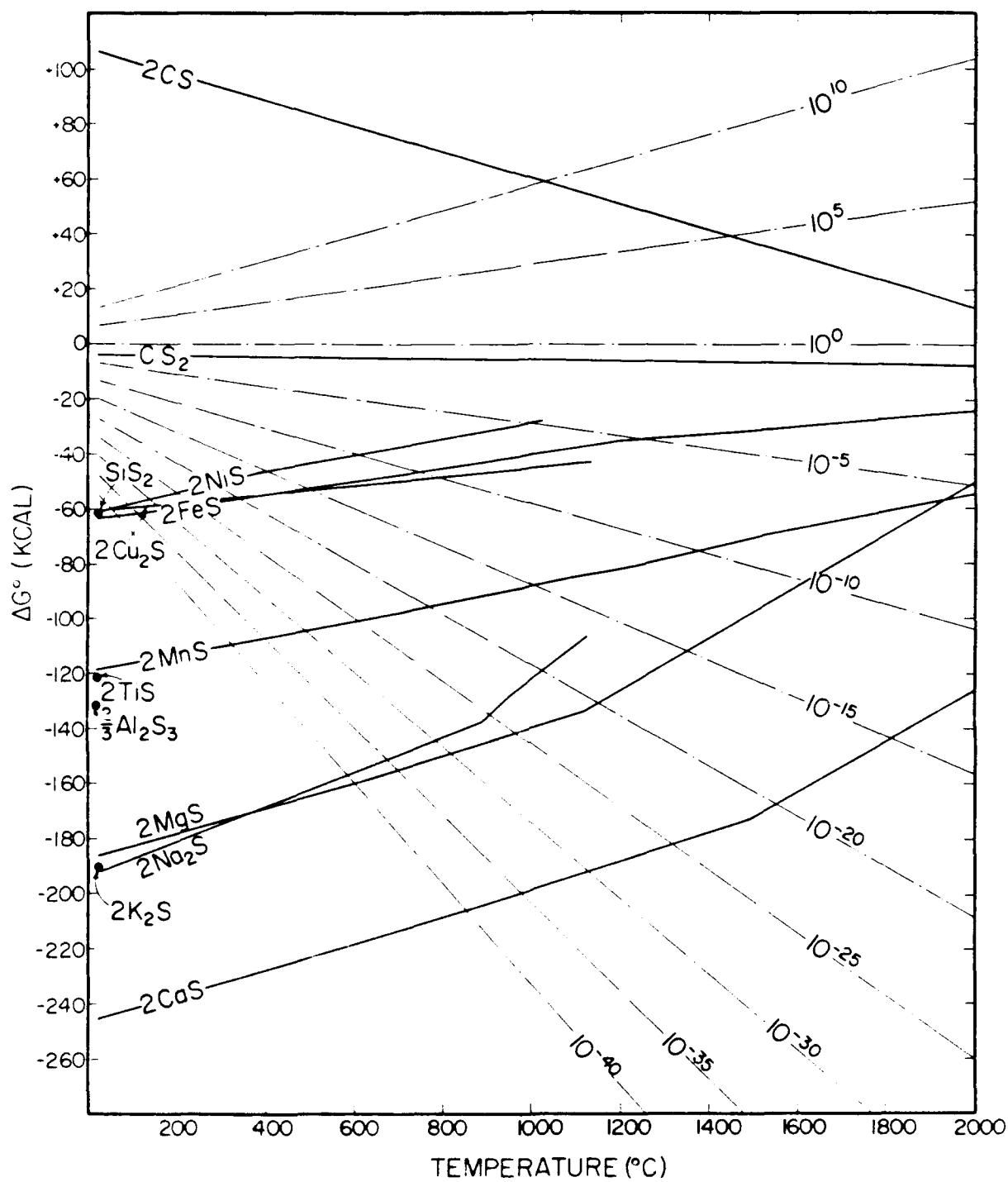


Figure A.2. Free Energy of Formation of Sulfides [Ref. 39:p. 8].

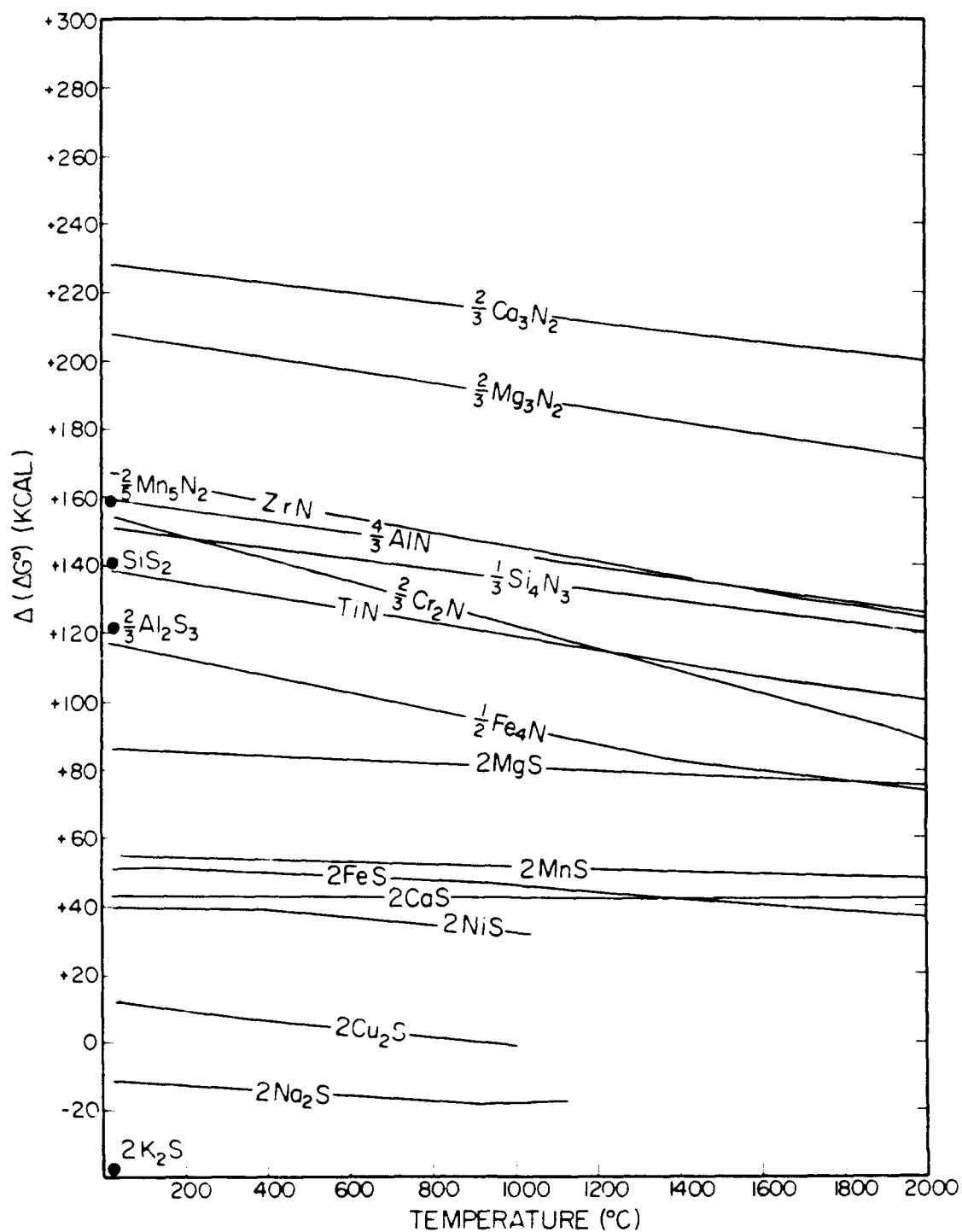
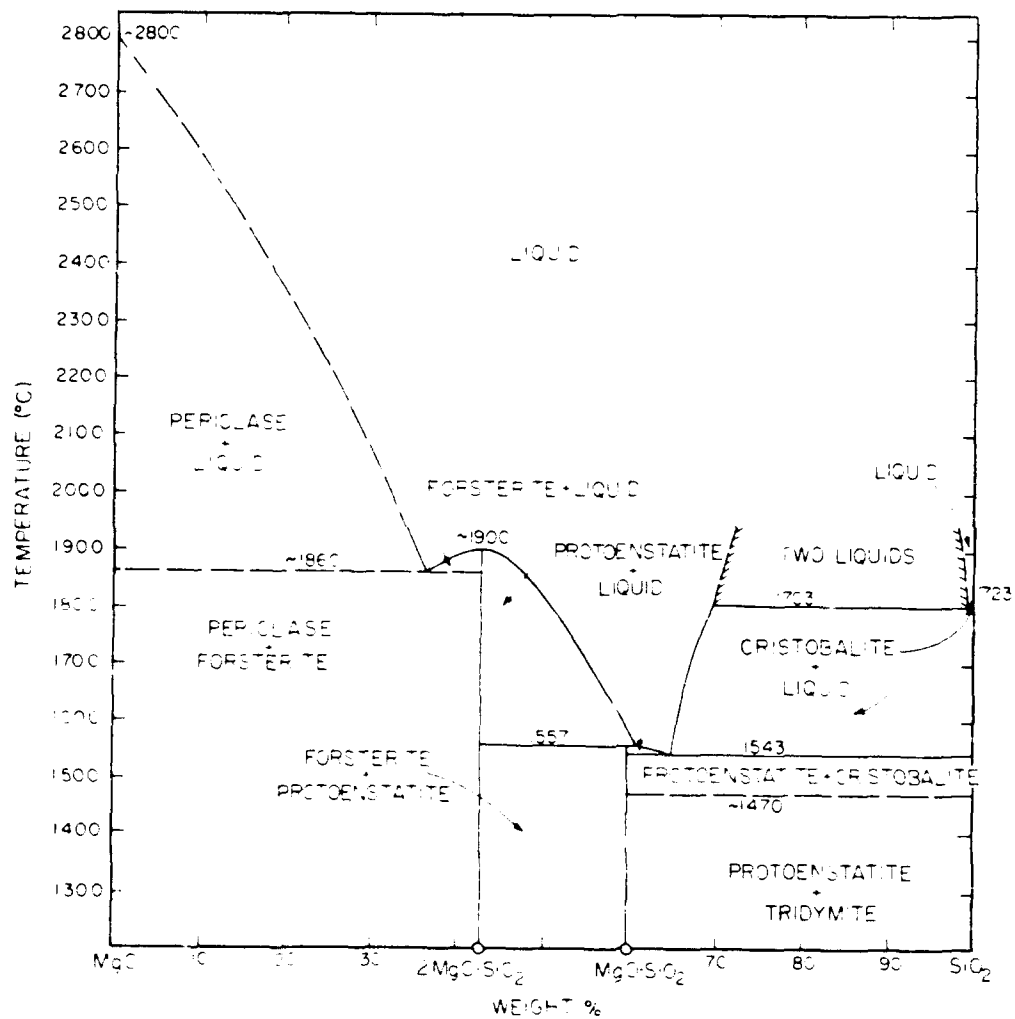


Figure A.3. Comparison of Free Energies of Formation [Ref. 39:p. 11].



**Figure A.4.** Phase diagram of MgO-SiO<sub>2</sub> System [Ref. 39:p. 39].

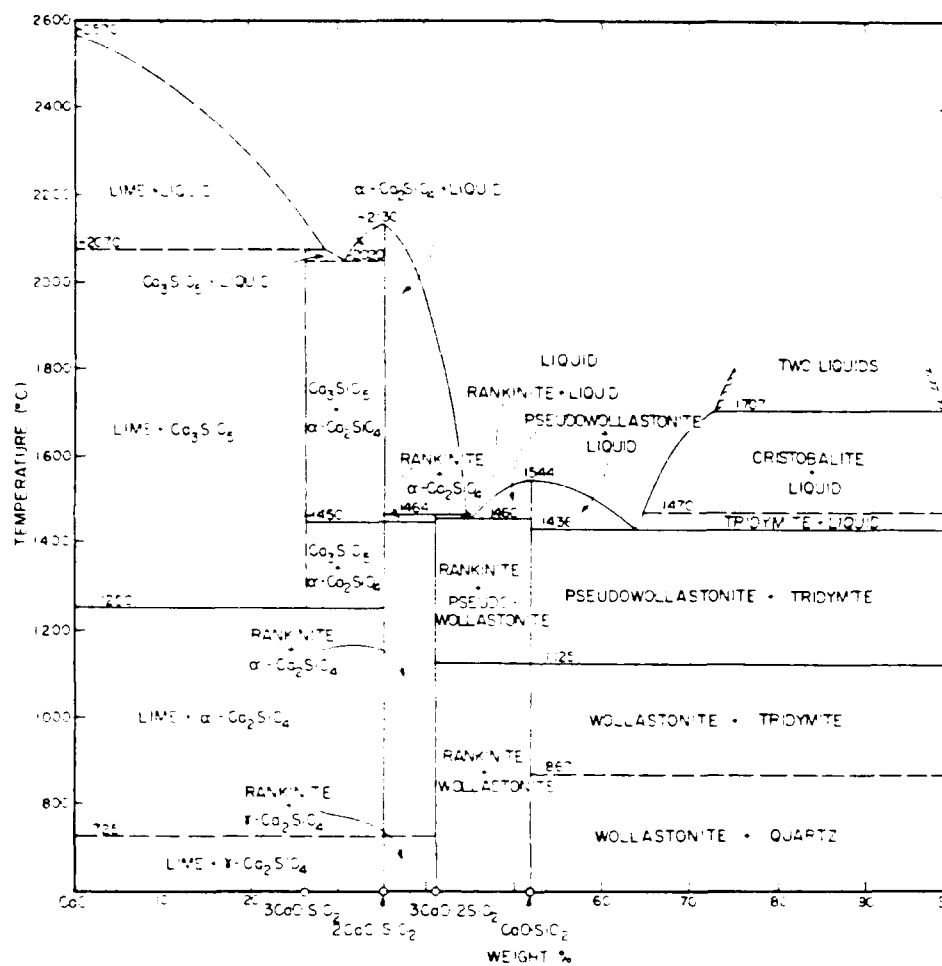


Figure A.5. Phase Diagram of CaO-SiO<sub>2</sub> System [Ref. 39:p. 35]



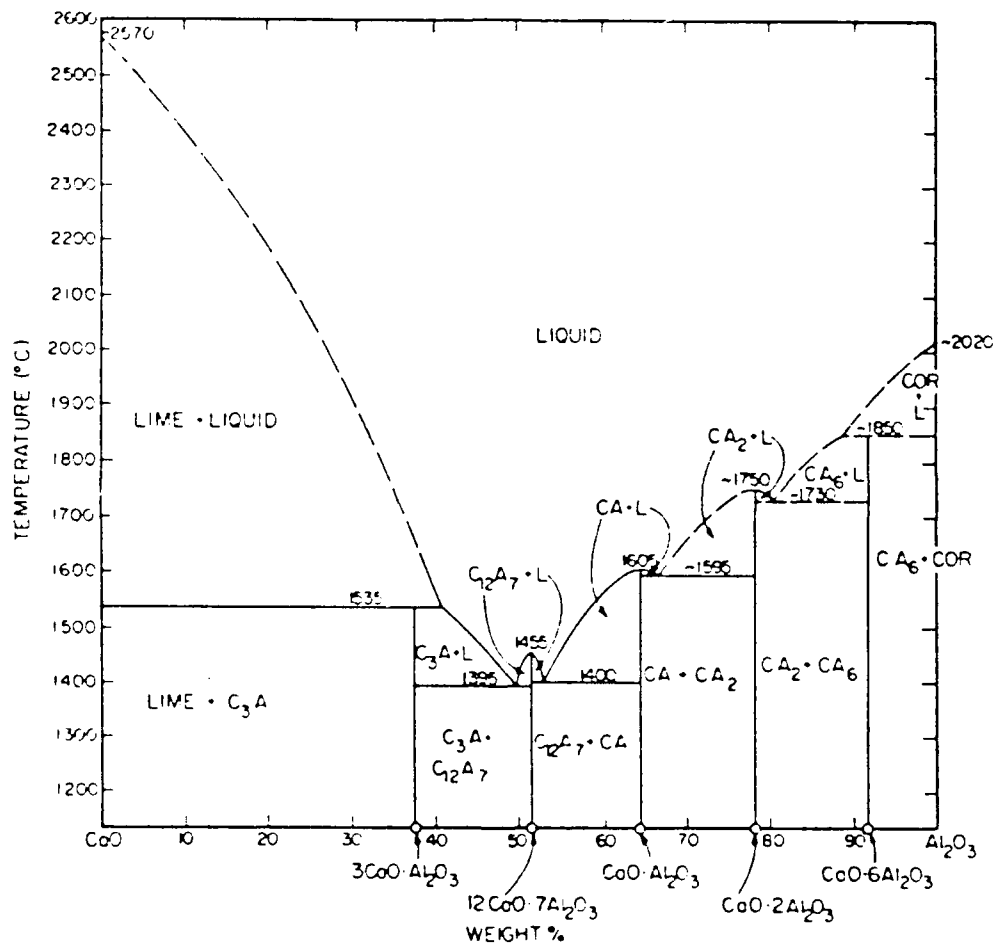
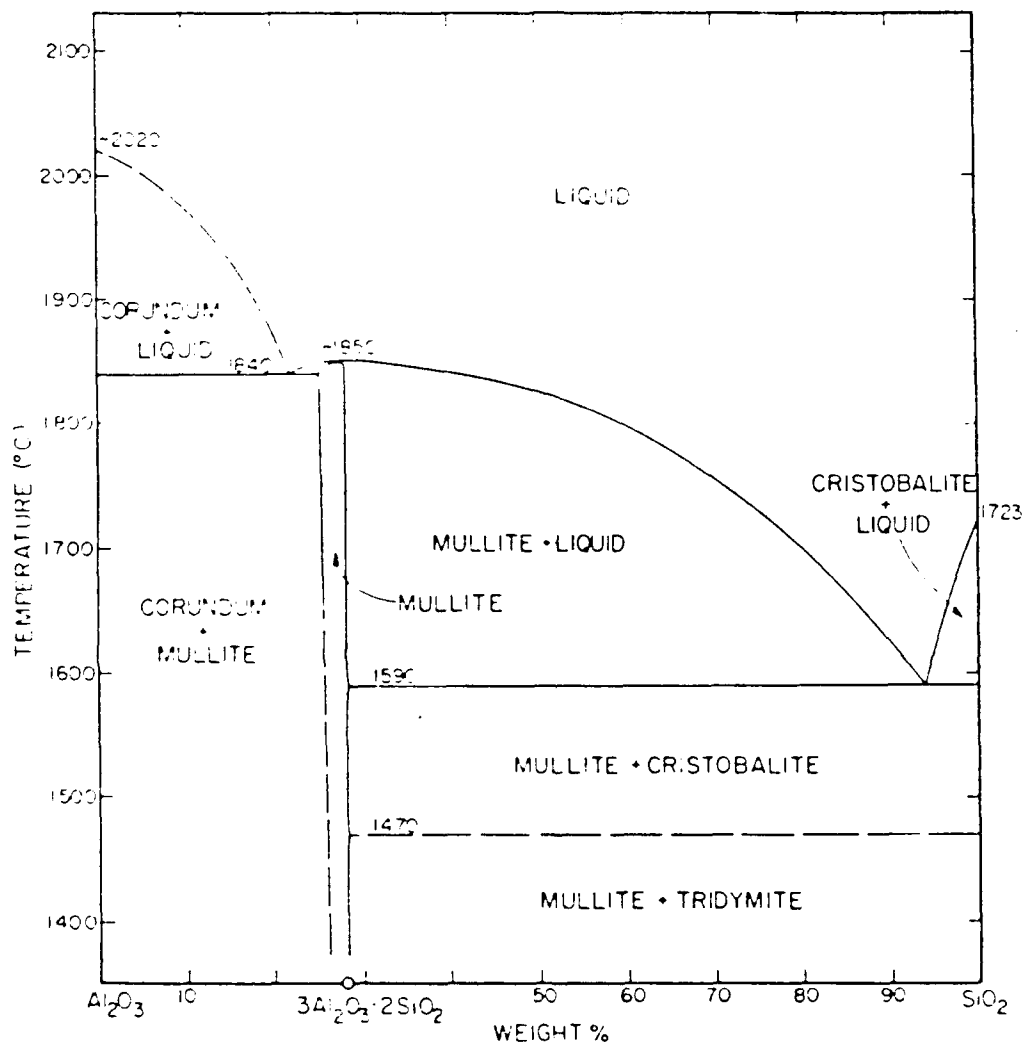


Figure A.6. Phase Diagram of CaO-Al<sub>2</sub>O<sub>3</sub> System [Ref. 39:p. 42]



**Figure A.7.** Phase diagram of  $\text{Al}_2\text{O}_3$ - $\text{SiO}_2$  System [Ref. 39:p. 37].

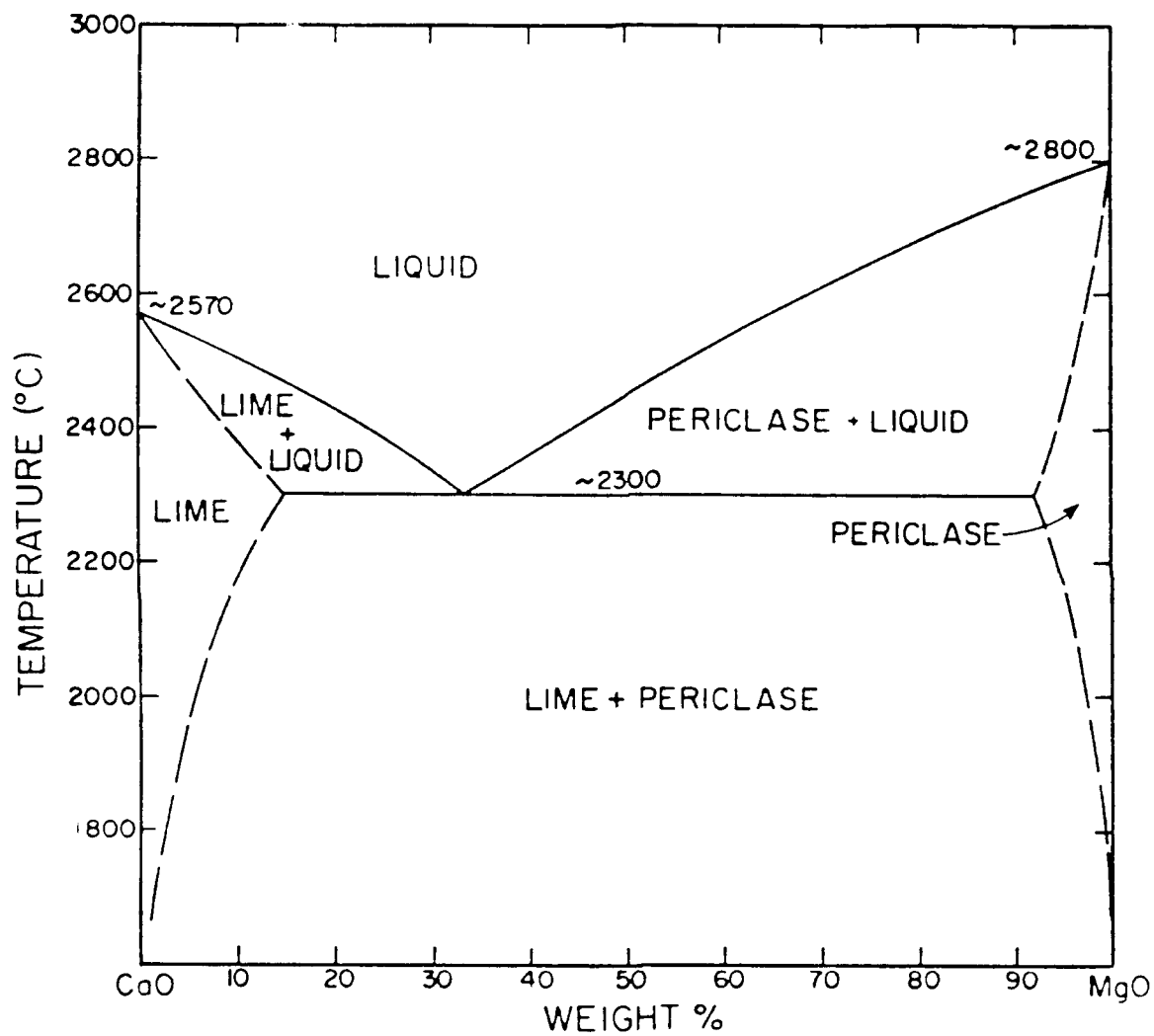


Figure A.8. Phase Diagram of CaO-MgO System [Ref. 39:p. 42].

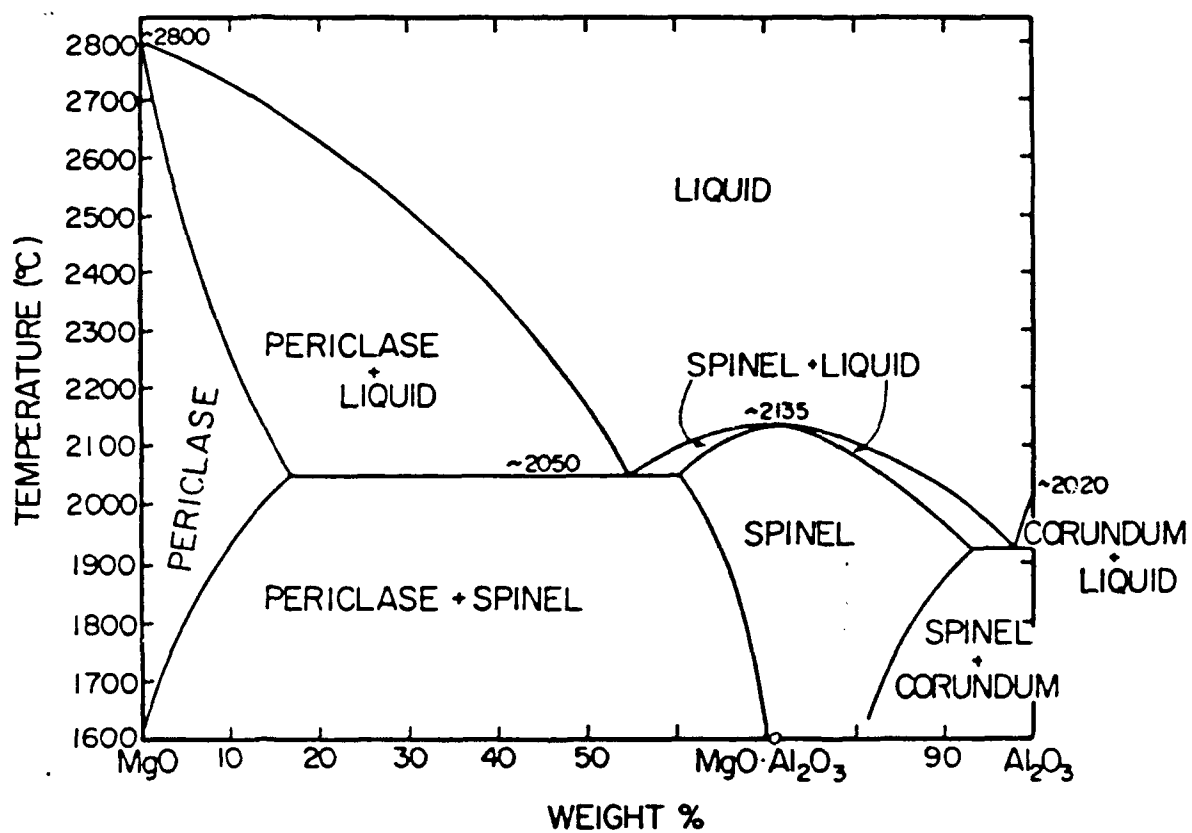
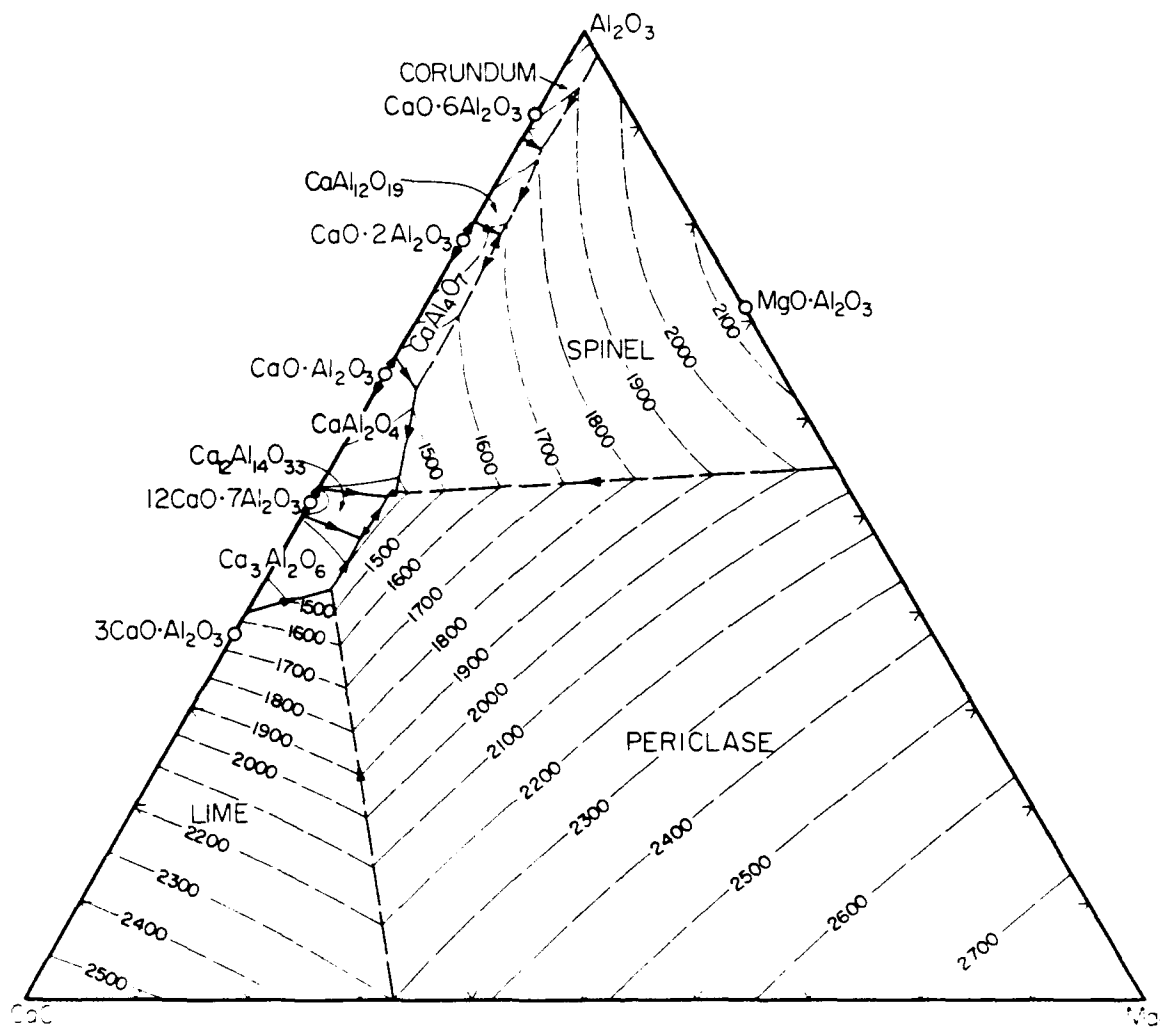
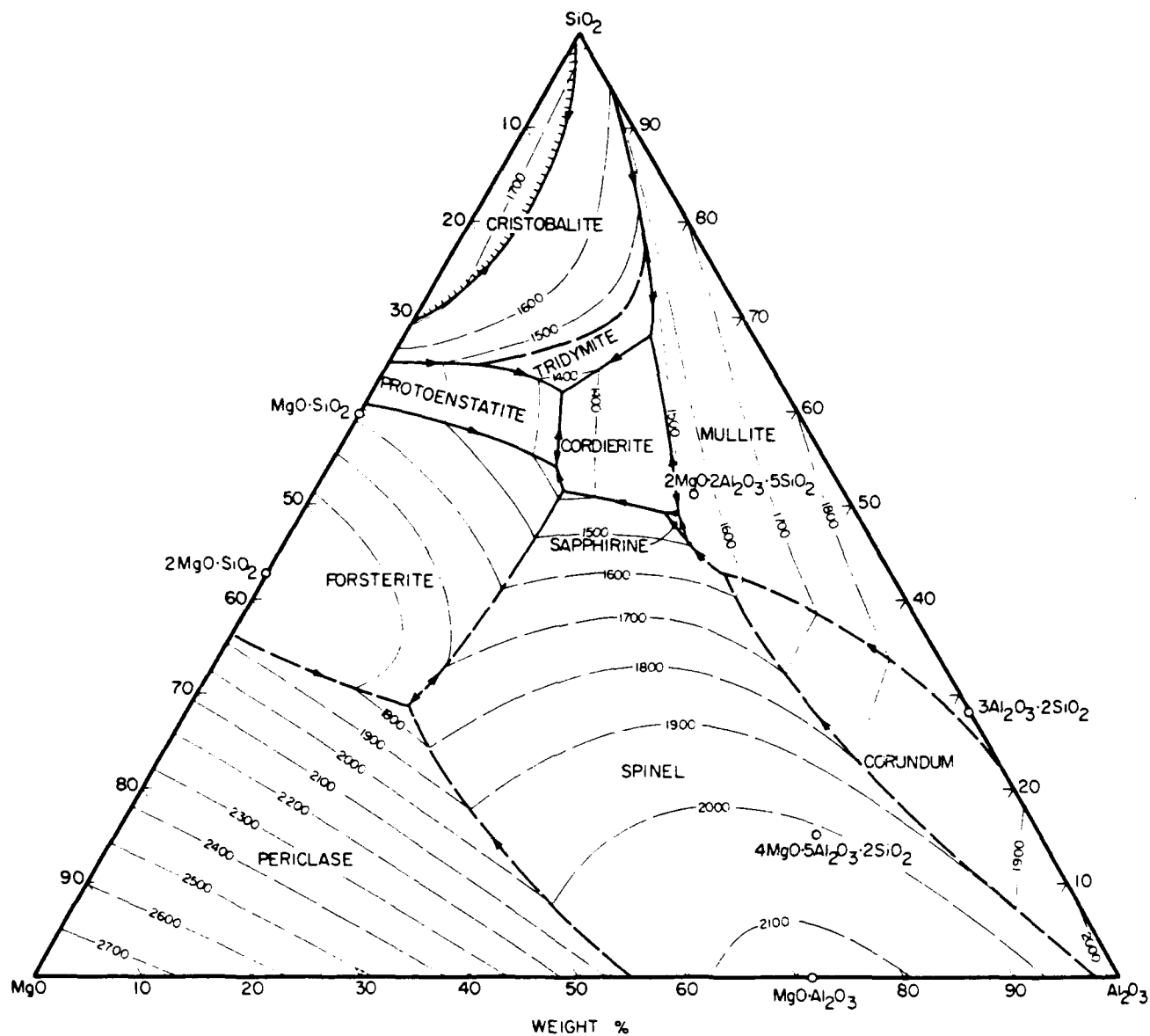


Figure A.9. Phase Diagram of MgO-Al<sub>2</sub>O<sub>3</sub> System [Ref. 39:p. 46].



**Figure A.10. Ternary Phase Diagram of CaO-MgO-Al<sub>2</sub>O<sub>3</sub> System [Ref. 39:p. 101]**



**Figure A.11. Ternary Phase Diagram of MgO-Al<sub>2</sub>O<sub>3</sub>-SiO<sub>2</sub> System [Ref. 39:p. 96].**

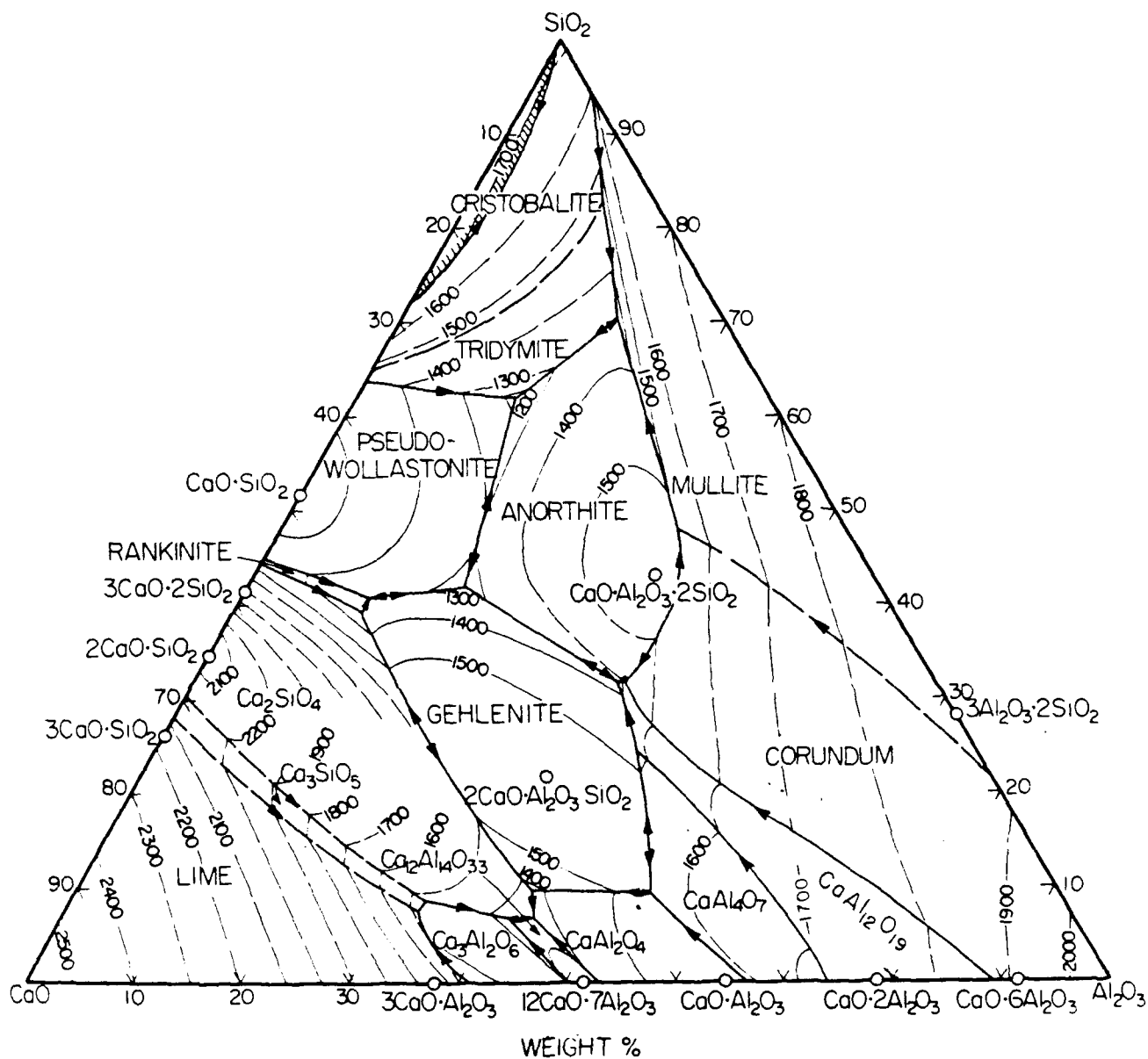


Figure A.12. Ternary Phase Diagram of CaO-Al<sub>2</sub>O<sub>3</sub>-SiO<sub>2</sub> System [Ref. 39:p. 93].

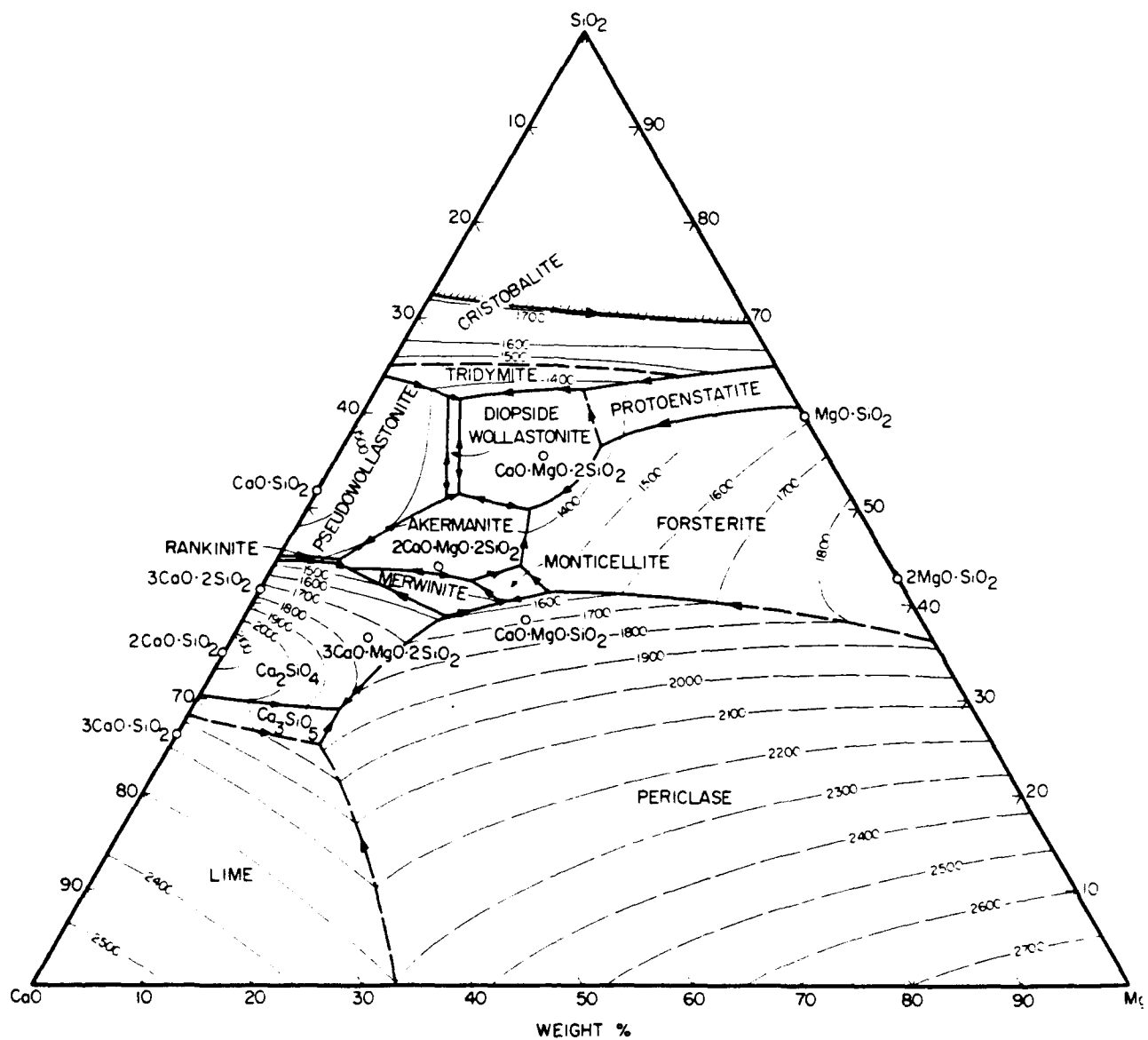


Figure A.13. Ternary Phase Diagram of CaO-MgO-SiO<sub>2</sub> System [Ref. 39:p. 92].



**APPENDIX B**  
**DTRC TENSILE TEST DATA**

<b>SPECIMEN ID</b>	<b>TEMPER (C)</b>	<b>ELONG (%)</b>	<b>AREA REDUCTION (%)</b>	<b>0.2% YS (MPa)</b>	<b>TENSILE STRENGTH (MPa)</b>
GQH 11	AQ	20.6	69.0	754	999
GQH 12	AQ	24.0	67.25	738	973
GQH 13	AQ	24.25	69.0	744	983
GQH 14	AQ	23.5	67.9	718	974
GQH 15	AQ	21.15	69.3	718	1000
GQH 16	AQ	24.5	68.6	707	1002
GQH 17	AQ	24.8	67.9	749	1003
GQH 18	AQ	24.55	66.8	780	996
GQH 21	399	31.0	68.9	917	986
GQH 23	399	24.7	63.3	945	1009
GQH 61	454	33.6	62.4	1028	1081
GQH 64	454	27.1	74.0	1047	1094
GQA 31	510	31.7	64.3	1009	1047
GQH 33	510	37.5	63.8	1005	1045
GQH 72	566	34.4	71.1	949	984
GQH 74	566	33.4	68.4	957	984
GQH 47	621	31.1	75.0	826	858
GQH 49	621	37.1	76.0	829	858
GQH 54	677	41.8	73.4	669	826

**APPENDIX C**  
**DTRC CHARPY V-NOTCH IMPACT ENERGY TEST DATA**

SPECIMEN ID	TEMPER (C)	TEST TEMP. (C)	IMPACT ENERGY (J)
GHQ 41	AQ	21.1	108.5
GQH 29	AQ	-17.8	97.6
GQH 30	AQ	-17.8	94.9
GQH 31	AQ	-17.8	94.9
GQH 32	AQ	-67.7	82.7
GQH 33	AQ	-67.7	71.9
GQH 34	AQ	-67.7	75.9
GQH 35	AQ	-73.3	85.4
GQH 38	AQ	-84.4	31.2
GQH 39	AQ	-84.4	46.1
GQH 40	AG	-84.4	63.7
GQH 26	AQ	-101.1	66.4
GQH 27	AQ	-101.1	38.0
GQH 28	AQ	-101.1	58.3
GQH 36	AQ	-117.8	28.5
GQH 37	AQ	-117.8	33.9
GQH 43	399	21.1	66.4
GQH 44	399	21.1	65.1
GQH 45	399	-17.8	46.1
GQH 46	399	-17.8	54.2
GQH 55	399	-34.4	36.6
GQH 56	399	-34.4	33.9
GQH 57	399	-45.6	40.7
GQH 58	399	-45.6	36.6
GQH 47	399	-51.1	25.8
GQH 48	399	-51.1	28.5
GQH 49	399	-67.8	31.2
GQH 50	399	-67.8	21.7
GQH 51	399	-84.4	19.0

SPECIMEN ID	TEMPER (C)	TEST TEMP. (C)	IMPACT ENERGY (J)
GQH 52	399	-84.4	19.0
GQH 53	399	-101.1	20.3
GQH 54	399	-101.1	21.7
GQH 107	454	21.1	36.6
GQH 108	454	21.1	35.2
GQH 109	454	1.67	29.8
GQH 110	454	1.67	24.4
GQH 111	454	-17.8	23.0
GQH 112	454	-17.8	23.0
GQH 113	454	-34.4	24.4
GQH 114	454	-34.4	17.6
GQH 115	454	-84.4	9.49
GQH 116	454	-84.4	6.78
GQH 59	510	21.1	92.2
GQH 60	510	21.1	116.6
GQH 65	510	21.1	88.1
GQH 72	510	4.44	67.8
GQH 73	510	4.44	74.6
GQH 74	510	4.44	75.9
GQH 69	510	-17.8	61.0
GQH 61	510	-17.8	59.7
GQH 62	510	-17.8	52.9
GQH 66	510	-51.1	36.6
GQH 67	510	-51.1	35.3
GQH 68	510	-51.1	40.7
GQH 70	510	-67.8	46.1
GQH 71	510	-67.8	25.8
GQH 63	510	-84.4	31.2
GQH 64	510	-84.4	27.1
GQH 135	566	21.1	109.8
GQH 123	566	21.1	174.9
GQH 124	566	21.1	113.9
GQH 125	566	-17.8	122.0

SPECIMEN ID	TEMPER (C)	TEST TEMP. (C)	IMPACT ENERGY (J)
GQH 126	566	-17.8	109.8
GQH 129	566	-34.4	109.8
GQH 130	566	-34.4	105.8
GQH 131	566	-62.2	78.6
GQH 132	566	-62.2	78.6
GQH 137	566	-73.3	40.7
GQH 138	566	-73.3	44.7
GQH 136	566	-84.4	59.7
GQH 127	566	-84.4	44.7
GQH 128	566	-84.4	82.7
GQH 133	566	-101.1	48.4
GQH 134	566	-101.1	24.4
GQH 75	621	21.1	149.1
GQH 76	621	21.1	164.1
GQH 77	621	21.1	135.6
GQH 78	621	-17.8	128.8
GQH 79	621	-17.8	143.7
GQH 90	621	-45.6	132.9
GQH 80	621	-84.4	116.6
GQH 81	621	-84.4	86.8
GQH 86	621	-84.4	113.9
GQH 82	621	-101.1	108.5
GQH 83	621	-101.1	122.0
GQH 87	621	-101.1	99.0
GQH 84	621	-128.9	88.1
GQH 85	621	-128.9	90.8
GQH 88	621	-156.7	24.4
GQH 89	621	-156.7	5.4
GQH 91	677	21.1	135.6
GQH 93	677	21.1	135.6
GQH 95	677	21.1	132.9
GQH 97	677	-17.8	131.5
GQH 99	677	-17.8	141.0
GQH 101	677	-84.4	124.7
GQH 103	677	-84.4	122.0

SPECIMEN ID	TEMPER (C)	TEST TEMP. (C)	IMPACT ENERGY (J)
GQH 92	677	-101.1	109.8
GQH 94	677	-101.1	86.8
GQH 96	677	-101.1	99.0
GQH 98	677	-117.8	101.7
GQH 100	677	-117.8	96.3
GQH 102	677	-128.9	74.6
GQH 105	677	-128.9	88.1
GQH 104	677	-145.6	48.8
GQH 106	677	-145.6	35.3

## LIST OF REFERENCES

1. Czyryca, Ernest J., *Development of Low-Carbon, Copper-Strengthened HSLA Steel Plate for Naval Ship Construction*, DTRC-SME-90/21, June 1990.
2. Gudas, John P., *Pre-Certification Development Plan -HSLA 130 Steel for Submarine Construction*, DTRC, March 8, 1989.
3. Czyryca, Ernest J., R.E. Link, R.J. Wong, D.A. Aylor, T.W. Montemarano and J.P. Gudas PHD, *Development and Certification of HSLA-100 Steel for Naval Ship Construction*, Naval Engineers Journal, May 1990.
4. Czyryca, E.J., and R.E. Link, *Physical Properties, Elastic Constants, and Metallurgy of HSLA-100 Steel Plate*, DTRC/SME-88/62, December 1988.
5. Coldren, A.P., and T.B. Cox, *Development of 100 KSI Yield Strength HSLA Steel*, DTNSRDC/SME-CR-07-86, July 1986.
6. Anderson, T.L., J.A. Hyatt, and J.C. West, *The Benefits of New High Strength Low-Alloy (HLSA) Steels*, Welding Journal, Vol. 66, September 1987.
7. Pickering, F.B., *Physical Metallurgy and the Design of Steels*, Applied Science Publishers LTD, London, 1978.
8. Irving, R., *Microalloying - The Route to Stronger Tougher Steels*, Iron Age, February 16, 1983.
9. Porter, L.F., and P.E. Repas, *The Evolution of HSLA Steels*, Journal of Metals, April 1982.
10. Kiessling, R.K., *Non-metallic Inclusions in Steel*, Part 5, The Institute of Metals, London, 1989.
11. Le May, I., and L. McDonald Schetky, *Copper in Iron and Steel*, John Wiley and Sons, New York.

12. Natishan, M.E., *Mechanisms of Strength and Toughness in a Microalloyed Precipitation Hardened Steel*, PH.D. Thesis, University of Virginia, 1989.
13. Mattes, V., *Microstructure and Mechanical Properties of HSLA-100 Steel*, Master's Thesis, Naval Postgraduate School, Monterey, CA, December 1990.
14. Aroztegui, J.J., J.J. Urcola, and M. Fuentes, *The Influence of Copper Precipitation and Plastic Deformation Hardening on the Impact-Transition Temperature of Rolled Structural Steels*, Metallurgical Transactions A, Vol. 20A, September 1989.
15. Miglin, M.T., J.P. Hirth and A.R. Rosenfield, *Effects of Microstructure on Fracture Toughness of a High-Strength Low-Alloy Steel*, Metallurgical Transactions A, Vol. 14A, October 1983.
16. Wilson, A.D., and others, *Properties and Microstructures of Copper Precipitation Aged Plate Steels*, Microalloyed HSLA Steels, Proceedings of Microalloying '88, ASM International.
17. Kiessling, R., and N. Lange, *Non-metallic Inclusions in Steel, Parts I-IV*, The Metal Society, London, 1978.
18. Hertzberg, R.W., *Deformation and Fracture Mechanics of Engineering Materials*, 3rd ed., John Wiley and Sons, Inc., 1989.
19. Ellis, D., *The Effects of Titanium Inclusions on HY-80 GMA Weld Deposits*, Master's Thesis, Naval Postgraduate School, Monterey, CA, December 1990.
20. Edmonds, D.V., and R.C. Cochrane, *Structure-Property Relationships in Bainitic Steels*, Metallurgical Transactions, Vol. 21A, June 1990.
21. Barrett, C.R., W.D. Nix, and A.S. Tetelman, *The Principles of Engineering Materials*, Prentice-Hall, Inc., 1973.
22. Korchynsky, M., *Microalloying and Thermo-Mechanical Treatment, Processing, Microstructure and Properties of HSLA Steels*, edited by A.J. De Ardo, The Minerals, Metals & Materials Society, 1988.
23. Cohen, M., and S.S. Hansen, *On the Fundamentals of HSLA Steels, HSLA Steels: Metallurgy and Applications*, Proceedings of an International Conference on HSLA Steels '85, ASM International.

24. Speer, J.G., and S.S. Hansen, *Austenite Recrystallization and Carbonitride Precipitation in Niobium Microalloyed Steels*, Metallurgical Transactions A, Vol. 20A, January 1989.
25. Richman, M.H., *An Introduction to the Science of Metals*, Ginn Custom Publishing, MA, 1974.
26. Miglin, M.T., and others, *Microstructure of a Quenched and Tempered Cu-Bearing High Strength Low Alloy Steel*, Metallurgical Transactions A, Vol. 17A, May 1986.
27. Hornbogen, E., *Aging and Plastic Deformation of an Fe-0.9% Cu Alloy*, Transactions of the ASM, Vol. 57, 1964.
28. Dhamen, U., P. Ferguson, and K.H. Westmacott, *Invariant Line Strain and Needle-Precipitate Growth Direction in Fe-Cu*, Acta Metallurgica, Vol. 32, No.5, 1984.
29. Speich, G.R., and R.A. Orani, *The Rate of Coarsening of Copper Precipitate in an Alpha-Iron Matrix*, Transactions of the Metallurgical Society of AIME, Vol. 233, April 1965.
30. Goodman, S.R., S.S. Brenner, and J.R. Low, *An FIM-Atom Probe Study of the Precipitation of Copper from Iron-1.4 At. Pct. Copper. Part I: Field-Ion Microscopy*, Metallurgical Transactions, Vol. 4, October 1973.
31. Goodman, S.R., S.S. Brenner, and J.R. Low, *An FIM-Atom Probe Study of the Precipitation of Copper From Iron-1.4 At. Pct. Copper. Part II: Atom Probe Analysis*, Metallurgical Transactions, Vol. 4, October 1973.
32. Russell, K.C., and L.M. Brown, *A Dispersion Strengthening Model Based on Differing Elastic Moduli, Applied to the Iron-Copper System*, ACTA Metallurgica, Vol. 20, July 1972.
33. Hamburg, E.G., and A.D. Wilson, *Production and Properties of Copper Age-Hardened Steels*, Processing, Microstructure and Properties of HSLA Steels, edited by A.J. De Ardo, The Minerals, Metals & Materials Society, 1988.
34. Turkdogan, E.T., *Metallurgical Consequences of Calcium Retention in Liquid and Solid Steel*, Proceedings of International Calcium Treatment Symposium, June 30, 1988.



35. Kitamura, M., and others, *Desulfurization Process and Shape Control of Inclusions by the Addition of Calcium or Rare Earth Metals*, Steelmaking Proceedings, Washington, D.C., AIME, 1980.
36. Faulring, G.M., J.W. Farrell, and D.C. Hilty, *Steel Flow Through Nozzles: Influences of Calcium*, Electric Furnace Conference Proceedings, 1979.
37. Wilson, A.D., *Characterizing Inclusion Shape Control in Low Sulfur C-Mn-Cb Steels*, HSLA Steels, Technology, and Applications Conference Proceedings, Philadelphia, PA, ASM, October 1983.
38. Howell, P.R., and R. Varughese, *Austenite Transformation Products in Quenched Low-Carbon HSLA Steel*, Proceedings of the XXII International Congress for Electron Microscopy, San Francisco, CA, 1990.
39. Muan, A., and E.F. Osborn, *Phase Equilibrium Among Oxides in Steelmaking*, Addison-Wesley Publishing Company, MA, 1965.

## INITIAL DISTRIBUTION LIST

	No. Copies
1. Defense Technical Information Center Cameron Station Alexandria, VA 22304-6145	2
2. Library, Code 52 Naval Postgraduate School Monterey, CA 93943-5002	2
3. Department Chairman, Code ME/Hy Department of Mechanical Engineering Naval Postgraduate School Monterey, CA 93943-5000	1
4. Naval Engineering Curricular Office, Code NE Naval Postgraduate School Monterey, CA 93943-5000	1
5. Dr. Alan G. Fox, Code ME/Fo Department of Mechanical Engineering Naval Postgraduate School Monterey, CA 93943-5000	2
6. Lt. Lawrence W. Comerford 7843 Pluto Court Pensacola, FL 32506	2
7. Dr. M.G. Vassilaros, Code 2814 David Taylor Research Center Annapolis, MD 21402	1

8. Ms. Stephanie Mickalac, Code 2814  
David Taylor Research Center  
Annapolis, MD 21402

1